



# Influence of porous material on the flow behind a backward-facing step: experimental study

L. Klotz<sup>1,†</sup>, K. Bukowski<sup>1</sup> and K. Gumowski<sup>1</sup>

<sup>1</sup>Institute of Aeronautics and Applied Mechanics, Warsaw University of Technology, Nowowiejska 24, 00-665 Warsaw, Poland

(Received 31 July 2022; revised 24 June 2024; accepted 21 July 2024)

We investigate effect of porous insert located upstream of the separation edge of a backward-facing step (BFS) in early transitional regime as a function of Reynolds number. This is an example of hydrodynamic system that is a combination of separated shear flow with large amplification potential and porous materials known for efficient flow destabilisation. Spectral analysis reveals that dynamics of BFS is dominated by spectral modes that remain globally coherent along the streamwise direction. We detect two branches of characteristic frequencies in the flow and with Hilbert transform we characterise their spatial support. For low Reynolds numbers, the dynamics of the flow is dominated by lower frequency, whereas for sufficiently large Reynolds numbers cross-over to higher frequencies is observed. Increasing permeability of the porous insert results in decrease in Reynolds number value, at which frequency cross-over occurs. By comparing normalised frequencies on each branch with local stability analysis, we attribute Kelvin–Helmholtz and Tollmien–Schlichting instabilities to upper and lower frequency branches, respectively. Finally, our results show that porous inserts enhance Kelvin–Helmholtz instability and promote transition to oscillator-type dynamics. Specifically, the amplitude of vortical (BFS) structures associated with higher-frequency branch follows Landau model prediction for all investigated porous inserts.

**Key words:** absolute/convective instability, separated flows, porous media

## 1. Introduction

Backward-facing-step (BFS) flow is a classical case to study separation and has remained an open problem for more than half of the century. This canonical configuration includes a localised geometry discontinuity, at which the level of the lower bounding wall suddenly

† Email address for correspondence: [lukasz.klotz@pw.edu.pl](mailto:lukasz.klotz@pw.edu.pl)

drops from the inlet to the outlet by step height  $h$  triggering the separation of the incoming upstream boundary layer. Separated flows are frequently encountered both in nature (river flow behind the dune bedforms or atmospheric flow over the hills) and in engineering applications (flow over airfoils, buildings or vehicles; flows in diffusers, turbines, compressors, inlets and junctions). As an example, the separation of the incoming boundary layer due to geometric discontinuity in combustion chambers promotes effective mixing. Understanding the mechanisms behind separated shear flow is crucial for the optimal design and control of flow devices to assure their high performance. Despite its simple geometry, the complex dynamics of BFS flow include separation of the incoming inflow, downstream evolution of separated shear layer, formation of the recirculation zone behind the step, eventual reattachment of the separated shear layer and subsequent downstream relaxation of the reattached flow to equilibrium boundary layer (e.g. Bradshaw & Wong 1972; Chen *et al.* 2018). In addition, BFS dynamics depend on many parameters, including Reynolds number, aspect ratio  $AR$  (spanwise extent of the model to the height of the step), expansion ratio  $ER$  (aspect between the outlet and inlet height) and inlet velocity profile at the separation edge.

Turbulent flow behind BFS at high Reynolds number is dominated by robust roll-up of separated shear layer due Kelvin–Helmholtz instability (e.g. Eaton & Johnston 1981; Driver, Seegmiller & Marvin 1987; Hudy, Naguib & Humphreys 2007; D’Adamo, Sosa & Artana 2014) that generates spanwise vortical coherent structures. Troutt, Scheelke & Norman (1984) and Jovic (1996) showed that their initial downstream evolution shares similarity with a free-mixing shear layer. However, this analogy fails further downstream due to the influence of a bottom bounding wall, adverse pressure gradient and reverse back-flow in the recirculation zone (Roos & Kegelman 1986).

The length of the recirculation zone is a well-studied property of BFS: in laminar flow, it increases monotonically with Reynolds number, then starts to decrease reaching the global minimum and, finally, slightly increases to reach an asymptotic value in the turbulent regime (e.g. Armaly *et al.* 1983; Durst & Tropea 1983). Downstream the reattachment of the shear layer, the flow remains far from the equilibrium and significant deviation from the conventional boundary layer was reported up to  $100h$  (Jovic & Driver 1994). This illustrates that the large-scale coherent vortices generated behind the step persist much further downstream than the reattachment.

In early transitional regime, the dynamics of spatially developing flows can be divided into oscillator and amplifier types (Monkewitz *et al.* 1990; Huerre 2000; Chomaz 2005): the former is characterised by well-defined intrinsic oscillations, whereas the later amplifies extrinsic environmental perturbations. This distinction was initially based on whether the upstream front of the linearised perturbation wave moves upstream: if yes, then perturbation grows in time from an initial infinitesimal perturbation; otherwise, the initial infinitesimal perturbation is flushed away from a specific point in space, as in boundary- or co-flowing mixing-layer flows. In this situation continuous infinitesimal forcing is required and downstream growth of the perturbation can be attributed to local convective instability (e.g. Kaiktsis, Karniadakis & Orszag 1996; Blackburn, Barkley & Sherwin 2008). A local description of convective instability has been proposed by Dovgal, Kozlov & Michalke (1994) for streamwise extended recirculation bubbles with length of the order of  $50h$ . Within this framework, local spatial amplification of a convective instability at any specific streamwise location can be predicted by linear stability analysis of the time-averaged streamwise velocity profile at that location, under the additional assumption of parallel base flow (i.e. homogeneous streamwise direction). This originates from boundary layer theory, according to which the ratio between wall-normal and

streamwise velocity components scales with one over the squared root of the Reynolds number, and for sufficiently high-Reynolds-number wall-normal velocity component can be neglected. Furthermore, this simplification is valid when the streamwise wavelength of the disturbance is small compared with the characteristic length scale of the variation of the base flow along the streamwise direction (Dovgal *et al.* 1994). According to the local theory, sufficiently weak streamwise initial perturbation grows exponentially along the streamwise direction until its amplitude is large enough and nonlinear saturation decreases effective growth rate (Dovgal *et al.* 1994).

In the global eigenmode framework (Chomaz 2005; Theofilis 2011), each characteristic frequency of oscillator corresponds to a single unstable global eigenmode. In contrast, amplifier dynamics needs to be described by superposition of several non-orthogonal eigenvectors (Cossu & Chomaz 1997; Sipp *et al.* 2010); potential for perturbation amplification depends on the degree of non-normality of the linearised Navier–Stokes operator that governs the dynamics of infinitesimal perturbation (Schmid & Henningson 2001; Chomaz 2005; Schmid 2007). However, amplifier-type dynamics is best characterised by the optimal response determined by resolvent analysis, rather than in basis composed of global eigenmodes (e.g. Marquet *et al.* 2008; Sipp *et al.* 2010; Symon *et al.* 2018). Empirical orthogonal functions (EOFs) is another basis to optimally represent spatial variance of vortical structures triggered by stochastic forcing (Dergham, Sipp & Robinet 2013).

Barkley, Gomes & Henderson (2002) evaluated the linear stability of BFS flow with  $ER = 2$  and with fully developed Poiseuille flow at the inlet upstream of the separation edge. They found that the first instability of spanwise uniform base flow occurs at  $Re_m = U_{max}h/\nu = 748$ , with  $Re_m$  defined based on the step height and centreline velocity. This bifurcation leads to stationary streamwise vortices concentrated in the recirculation zone with spanwise wavelength of  $\lambda_z = 6.9h$ . Lanzerstorfer & Kuhlmann (2012) extended this analysis for  $ER \in (1.3, 40.0)$ .

Marquet *et al.* (2009) modified the BFS geometry of Barkley *et al.* (2002) to prevent the emergence of a secondary recirculation zone at the top wall. They found similar bifurcation leading to steady streamwise vortices with rotation axes at approximately half of the step height  $h$ . They also showed that spatial support of direct and adjoint modes is spatially separated along the streamwise direction due to convective-type non-normality (see also Chomaz 2005). As a result, the maximal amplitude of global mode (describing flow response) is located downstream, whereas the maximum of adjoint modes (related to sensitivity of the flow to perturbation) is located upstream. Finally, they identified the recirculation zone as an optimal location for both volumetric body force and localised passive control devices.

Using the same geometry as in Barkley *et al.* (2002), Blackburn *et al.* (2008) characterised optimal initial perturbation and resulting optimal flow response. They reported that both two-dimensional and quasi-two-dimensional perturbations result in comparable energy gain that is attained at very similar time horizons and at the same downstream location. The spatial structure of both resulting waves consists of spanwise rollers with large coherence along the wall-normal direction and with major axes aligned in the streamwise and wall-normal directions. For linear perturbations with larger modulation along the spanwise direction, Marquet *et al.* (2008) observed an abrupt decrease of energy gain. This has been partially attributed to the loss of coherence along the spanwise direction and enhanced energy dissipation.

Dergham *et al.* (2013) studied the linear response to harmonic forcing in a BFS geometry with rounded corner using singular value decomposition (SVD) of the resolvent operator in

frequency domain. They identified the leading branch of shear layer dynamics associated with the amplification of the perturbation along the recirculation zone. They also evaluated the linear response of the system subjected to permanent stochastic forcing using EOF decomposition. The first pair of their EOF modes capture well the spatial structure derived from optimal harmonic response. Leading values of subsequent EOF modes decay rapidly indicating that this decomposition provides a robust basis to describe BFS dynamics. They also showed that spatial support of optimal stochastic forcing is located near the separation edge and that its energy convergence rate is even faster than for optimal EOFs.

Boujo & Gallaire (2015) observed that maximal energy amplification obtained with optimal frequency forcing is reached at most downstream locations: forcing with any other frequency will result in lower energy gain reached further upstream. They compared local and global stability analyses showing that both methods provide similar values of the most amplified forcing frequency. Corresponding integrated optimal amplification rates were comparable for both methods, with local amplification being approximately four times smaller when compared with the global method. Significant difference has been observed at higher forcing frequencies: velocity profiles are locally stable for high-frequency perturbation, whereas in global analysis high frequencies can be amplified through an Orr mechanism. Finally, they presented linearised sensitivity maps of energy gain for different flow modifications, including steady base flow modification, volume forcing and wall suction/blowing. The largest sensitivity of the flow to volume force is observed in the primary recirculation zone.

BFS flow is typically considered as a selective amplifier with relatively narrow frequency band for amplification. Within a linearised global framework, optimal initial perturbations, optimal harmonic forcing and stochastic forcing resulted in similar flow response (Blackburn *et al.* 2008; Dergham *et al.* 2013; Boujo & Gallaire 2015). However, in contrast to other canonical examples of amplifiers (e.g. mixing layer, boundary layer or free jet), BFS flow contains a recirculation zone. Dovgal *et al.* (1994) investigated separation of the boundary layer in different geometries (backward- and forward-facing steps, humps with upstream and/or downstream wedges), and for all considered configurations they demonstrated that the dynamics of the separated shear flow is mostly dominated by the primary recirculation zone formed immediately downstream of the separation edge. Moreover, for sufficiently high Reynolds numbers close to a fully turbulent regime, the recirculation zone seems to support oscillator-type behaviour (Wee *et al.* 2004; D'Adamo *et al.* 2014; Ma, Tang & Jiang 2020). Similar self-sustained global dynamics in the recirculation zone formed behind a smooth bump were reported by Marquillie & Ehrenstein (2003) and Passaglia, Leweke & Ehrenstein (2012).

Separation bubbles are another class of separated shear flows that can support self-sustained oscillations. However, in this case there is no geometrical discontinuity that could trigger separation. Hammond & Redekopp (1998) analysed expanded Falkner–Skan velocity profiles with two additional parameters to vary the intensity of the reverse flow and height of the recirculation region. They proposed that the separation bubble becomes absolutely unstable when the reverse flow exceeds 30% of the free-stream velocity. Recently, Avanci, Rodríguez & Alves (2019) considered the combined effect of the intensity of the back-flow and height of the recirculation zone. Specifically, they analysed the family of velocity profiles initially proposed by Dovgal *et al.* (1994) and reported that the local velocity profile can become absolutely unstable even for the intensity of the reversed flow as low as 2.5% of  $U_0$ . In addition, Rodríguez, Gennaro & Souza (2021) showed that weak spanwise modulation of the flow destabilises otherwise stable two-dimensional eigenmode.

In the context of early transitional regime, Marquet *et al.* (2008) suggested that very large transient amplification of spanwise rollers on the time scale imposed by the length of the recirculation zone leads to nonlinear modification of the flow, which, in turn, might allow spanwise-coherent structures to entirely dominate BFS dynamics. Nonlinear effects were studied by Blackburn *et al.* (2008) for BFS flow subjected to weak stochastic perturbation. They showed that linear and nonlinear responses have similar spatial structure and characteristic frequency. In addition, nonlinear response is characterised by narrow frequency band with no higher harmonics. A similar narrow frequency band with distinct central peak was observed in full direct numerical simulation (DNS) by Marquet & Sipp (2012).

Mantič-Lugo, Arratia & Gallaire (2014) evaluated nonlinearity with an iterative procedure that transforms the most-unstable mode into the marginal mode with zero growth rate (see Barkley 2006) through Reynolds stresses. The same Reynolds stresses modify the base flow into mean flow. This concept relies on the idea that nonlinear saturation of supercritical instability originating from Hopf bifurcation is a result of the interaction between base flow and Reynolds stresses induced by the most unstable mode (Stuart 1958; Zielinska *et al.* 1997). The same procedure has been also applied to BFS subjected to harmonic (Mantič-Lugo & Gallaire 2016*b*) and stochastic (Mantič-Lugo & Gallaire 2016*a*) forcing. For harmonic excitation they observed that nonlinearities suppress linear amplification of the dominant mode, resulting in nonlinear saturation similar to the supercritical limit cycle for a cylinder wake. However, there is no significant nonlinear influence on the selection of the most amplified frequency. Once the forcing amplitude is increased, maximal energy gain of the flow response is reached further upstream. This results in a reduction of recirculation length, similar to the effect of Reynolds stresses described by Zielinska *et al.* (1997) and Barkley (2006) for a cylinder wake. Regarding BFS response to stochastic forcing, the contribution to Reynolds stresses from a single optimal frequency was sufficient to obtain good qualitative prediction for nonlinear saturation.

For round jet flows characterised by convective instability, local stability analysis around the time-averaged mean flow predicts the perturbation field well (Gudmundsson & Colonius 2011; Garnaud *et al.* 2013; Oberleithner, Rukes & Soria 2014). For a cylinder wake (classical oscillator with one unstable eigenmode), linearisation around the mean flow provides good prediction for the oscillation frequency, even far from the oscillation threshold (Pier 2002; Barkley 2006). Mean flow stability analysis can provide a marginal mode with zero growth rate when higher harmonics of fundamental oscillation are sufficiently weak (Sipp & Lebedev 2007) or when oscillations are monochromatic (Turton, Tuckerman & Barkley 2015). In the context of BFS, Mantič-Lugo & Gallaire (2016*b*) demonstrated that higher harmonics can indeed be neglected in nonlinear saturation of growth perturbation even for finite-size amplitude forcing.

Harmonic resolvent analysis with linearisation around the mean flow combined with Reynolds decomposition is yet another method used to characterise energetically dominant vortical structures and their characteristic frequencies. In this case, the forcing term contains not only external environmental noise but also all nonlinear interactions of velocity fluctuations. Using this method Beneddine *et al.* (2016) analysed BFS dynamics at high Reynolds number and without distinguishing between oscillator and amplifier behaviour. Through a comparison of both resolvent analysis and linearisation around the mean flow, they concluded that mean flow stability analysis is valid when the dominant singular value of the resolvent operator at a given forcing frequency is significantly greater

than the others, provided that turbulent forcing does not display any preferential direction along any suboptimal resolvent vectors. If this condition is satisfied, then a marginally stable spectral mode and dominant response of resolvent SVD vector are proportional. They also showed that this condition holds for flows dominated by convective instability (e.g. resulting from Kelvin–Helmholtz instability) and for flows with marginally stable eigenmode. However, as demonstrated by Symon *et al.* (2018), a mode with growth rate closest to zero does not have to be strictly marginal, and it is sufficient that it dominates in the dyadic representation of the resolvent operator. If there is more than one eigenmode in the vicinity of the least-stable marginal mode, then the assumption of dominant value does not hold and the resolvent operator has to be described by more than one dominant response mode.

BFS has been also used to evaluate optimal control strategies of the separated shear layer to reduce the separation length or to maximise mixing efficiency. Passive flow control can be achieved by various devices, e.g. surface modifications with roughness, longitudinal groove, splitter plate or small secondary control cylinder (e.g. Choi, Jeon & Kim 2008). Another possibility is to use a porous material at the fluid–solid interface. As specified by Rosti, Cortelezzi & Quadrio (2015), porous materials have a wide range of applications, including filtration processes, extraction of oil or transpiration cooling to enhance heat exchange. Flows through sedimentary rocks, seabeds or riverbeds are examples encountered in nature. Porous material are also abundant in biological fluid, e.g. at the walls of blood vessels, lungs and kidneys.

Permeability at the fluid–porous interface can have a strong destabilising effect on both laminar and turbulent flows (e.g. Jiménez *et al.* 2001; Suga *et al.* 2010; Rosti *et al.* 2015; Wedin, Cherubini & Bottaro 2015; Ghosh *et al.* 2019). For laminar channel flow Tilton & Cortelezzi (2008) showed that wall permeability can dramatically decrease linear stability with respect to the solid impermeable case and that the most pronounced destabilisation is observed at low values of permeability. Similarly, Tilton & Cortelezzi (2015) reported that a small amount of wall permeability can destabilise asymptotic suction boundary layer flow and cause a substantial broadening of the region of unstable frequencies. For the same shear flow, Wedin *et al.* (2015) demonstrated that both the linear instability threshold and threshold for nonlinear travelling waves drop by more than 90 % when a porous substrate is included at the bottom bounding wall.

For turbulent flows, Jiménez *et al.* (2001) observed a significant increase of skin friction for flow over a permeable wall and attributed this increase to vortical spanwise rolls originating from Kelvin–Helmholtz-type instability. Similar organisation of spanwise structures induced by a porous medium at the bounding walls was also detected both experimentally (Suga *et al.* 2018) and in numerical simulations (Breugem, Boersma & Uittenbogaard 2006; Nishiyama, Kuwata & Suga 2020). Using internally heated turbulent shear flow configuration with porous bounding walls, Motoki *et al.* (2022) recently reported about the ultimate state, in which heat and momentum transfer are significantly enhanced due to the Kelvin–Helmholtz wave that is roughly uniform along the spanwise direction.

However, boundary conditions at the fluid–porous interface are important. Hahn, Je & Choi (2002) observed significant skin-friction reduction for turbulent flow when a streamwise slip condition without wall-normal component on the fluid–porous interface was assumed. When wall suction at the bounding wall is imposed without wall-normal velocity fluctuations at the interface, any non-trivial non-laminar dynamics is delayed and observed at larger values of Reynolds numbers (Wedin *et al.* 2015). Linear stability of the flow is also over-predicted in such a case when compared with experimental results

(Fransson & Alfredsson 2003). This indicates that the wall-normal velocity component and its temporal fluctuations at the fluid–porous interface have an important effect on the dynamics of the shear flow subjected to porous materials.

BFS at low Reynolds numbers is typically considered as an amplifier without intrinsic dynamics. Despite the absence of an unstable oscillating eigenmode in the linearised Navier–Stokes operator, BFS flow possesses an intrinsic response frequency captured by linear resolvent analysis that persists when nonlinear effects are included. Dominance of the intrinsic frequency and consistent spatial structure of the flow response indicates a possibility for global behaviour in BFS. BFS flow also satisfies known conditions for the marginal mode to exist, i.e. low level of higher harmonics and monochromatic frequency evolution. In addition, porous materials are known to destabilise the flow, i.e. increasing skin friction in fully turbulent flows and decreasing critical Reynolds number for linear instability. The porous insert can induce spanwise-coherent vortical structures (rollers), which makes it a good candidate for passive destabiliser of the BFS flow. We study BFS with an expansion ratio close to unity at low Reynolds numbers to carefully characterise dynamics of the BFS flow in the early transitional regime. Our aim is to characterise the combination of strong destabilisation of the least-stable mode by a porous insert with large potential for amplification observed in BFS flow. The paper is divided as follows: the experimental set-up and results are presented in § 2 and § 3, respectively. Spectral analysis of measured velocity fields is described in § 4, including the determination of characteristic Strouhal numbers, bifurcation diagrams, spatial support of envelopes for each frequency range and description of the dominating characteristic frequencies in terms of canonical instabilities. In § 5 we present measurements of cross-stream velocity components. Measurements in other auxiliary planes are presented in § 6. In § 7 and § 8 we characterise the incoming boundary layer upstream of the separation edge and time-averaged fields in the primary recirculation zone. Finally, in § 9 and § 10 we discuss and conclude our results.

## 2. Experimental set-up

The experimental configuration is presented in figure 1. The incoming boundary layer at the separation edge (blue profile) is characterised by the free-stream velocity ( $U_0$ ), displacement ( $\delta_0$ ) and momentum ( $\theta_0$ ) thickness. We denote the streamwise (direction of the free-stream), wall-normal (vertical) and spanwise (transverse) directions as  $x$ ,  $y$ ,  $z$ , respectively. The origin of the coordinate system is placed in the  $x$ – $y$  symmetry plane at the lower corner between the BFS and the floor–wall. An interchangeable insert with streamwise extent of  $L_p \simeq 5$  cm marked as a red cuboid is located directly upstream of the separation edge ( $-L_p \leq x \leq 0$ ) and extends below the level of the inlet floor channel ( $0 \leq y \leq h$ ). To evaluate the effect of a porous material upstream of the separation edge, we consider four different insert configurations: solid impermeable insert as the reference case and three inserts made of rectified foams with 10, 20 and 45 PPI (pores per inches) corresponding to 2.54, 1.27 and 0.56 mm of average linear pore size, respectively.

Step height for each insert configuration was determined using a laser sheet and camera with a spatial resolution of 0.14 mm per pixel. The laser sheet illuminated the level of the lower bounding wall upstream and downstream of the separation edge ( $y = h$  at the inlet and  $y = 0$  at the outlet, respectively). The resulting value of  $h = 5.77 \pm 0.14$  mm is a compromise between ensuring the largest possible spanwise aspect ratio ( $AR \approx 26$ ) and having a sufficient spatial resolution for the particle image velocimetry (PIV) method.

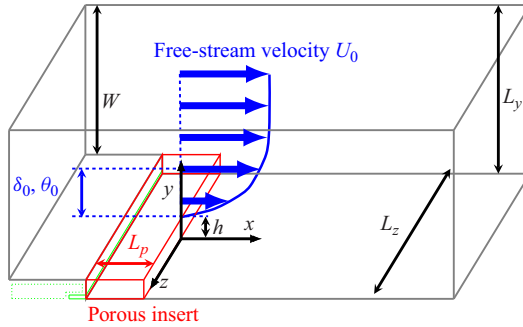


Figure 1. Schematic representation of an experimental set-up of BFS with  $h$  as the step height. Blue profile indicates boundary layer at the separation edge characterised by the free-stream velocity  $U_0$ , as well as displacement ( $\delta_0$ ) and momentum ( $\theta_0$ ) thickness. The red volume indicates the location of the replaceable insert with length  $L_p$ . The black coordinate system defines the streamwise ( $x$ ), wall-normal ( $y$ ) and spanwise ( $z$ ) directions, respectively. Thin green lines mark the system that delivers dye into the recirculation zone for flow visualisations: solid and dashed lines correspond to the narrow slit and inner chamber inside the inlet floor for flow visualisations, respectively. Channel height above the porous insert upstream of the separation edge is marked as  $W$ .

The cross-section of the outlet test section downstream of the separation edge is equal to  $L_y \times L_z = 10 \text{ cm} \times 15 \text{ cm}$ . This results in an expansion ratio of  $ER = L_y/W = 1.06$  (equivalent to a step-to-outlet ratio  $\Gamma = h/L_y = 0.058$ ). The small height of the step allows us to measure a large area up to  $x \leq 50h$  downstream of the separation edge. Here  $W$  denotes the height of the inlet channel above the porous substrate upstream of the separation edge ( $x < 0$ ).

Permeability is the primary parameter associated with the hydrodynamics within a porous medium and describes a relationship between pressure drop across the medium and Darcy's drift velocity in the bulk of the porous medium. Typically, its value depends on the details of the geometry, such as porosity and pore diameter (Edouard *et al.* 2008). It also characterises the influence of the porous material on the shear flow above the porous substrate in the fluid–porous interface (Breugem *et al.* 2006; Suga *et al.* 2010), even at the limit of low permeability (Rosti *et al.* 2015). Specifically, among permeability, porosity and thickness of the porous material, the permeability was shown to be the main parameter describing the response of the shear flow to the permeable wall (Rosti *et al.* 2015). Finally, permeability also quantifies the effect of the porous substrate on the linear stability of the shear flow above at a given value of Reynolds number (Tilton & Cortelezzi 2015; Wedin *et al.* 2015). The measured permeabilities of porous inserts are  $k_1 = 11.0 \times 10^{-8} \text{ (m}^2\text{)}$  for 10 PPI,  $k_1 = 8.9 \times 10^{-8} \text{ (m}^2\text{)}$  for 20 PPI and  $k_1 = 4.6 \times 10^{-8} \text{ (m}^2\text{)}$  for 45 PPI, respectively (see Appendix A). The effective permeability pore diameter ( $\sqrt{k_1}$ ) varies from 0.21 mm (45 PPI) to 0.33 mm (10 PPI) and defines the most relevant characteristic microscale within the bulk of the porous medium (Beavers & Joseph 1967; James & Davis 2001; Breugem, Boersma & Uittenbogaard 2005; Breugem *et al.* 2006), as well as in the fluid–porous interface (Ochoa-Tapia & Whitaker 1995; James & Davis 2001).

Relative permeability normalised with channel height above the porous insert ( $k_1/W^2$ ) is the most suitable macroscale hydrodynamical parameter of the porous medium in our geometrical configuration with low expansion ratio. Low relative permeability is equivalent to a large ratio between the hydraulic resistance of the porous insert and the hydraulic resistance of the shear flow above the porous substrate. Increasing channel height  $W$  decreases relative permeability and results in a relative increase of the shear flow

volume flux when compared with flux through the porous insert, in analogy to a parallel network of electrical resistors. In addition, when the effective permeability pore size ( $\sqrt{k_1}$ ) is much lower than the height of the channel above the porous substrate ( $W$ ), then the bulk of the porous insert becomes effectively impermeable and leads to a significant reduction of the slip velocity at the fluid–porous interface (Breugem *et al.* 2005).

An expansion ratio close to unity ( $ER \simeq 1$ ) results in the low relative permeability of our inserts:  $k_1/W^2 = 12.4 \times 10^{-6}$  for 10 PPI,  $k_1/W^2 = 10.0 \times 10^{-6}$  for 20 PPI and  $k_1/W^2 = 5.2 \times 10^{-6}$  for 45 PPI, respectively. The largest value for 10 PPI is approximately one order of magnitude lower than the maximal relative permeability considered by Gupte & Advani (1997,  $k_{max}/W^2 = 5.2 \times 10^{-4}$ ), Breugem *et al.* (2006,  $k_{max}/W^2 = 1.9 \times 10^{-4}$ ), Suga & Nishio (2009,  $k_{max}/W^2 = 8.9 \times 10^{-4}$ ), Suga *et al.* (2010,  $k_{max}/W^2 = 9.7 \times 10^{-5}$ ) and Kuwata & Suga (2016,  $k_{max}/W^2 = 1.7 \times 10^{-4}$ ) to list a few. Therefore, we expect that the influence of the porous substrate will be manifested at the fluid–porous interface, rather than in the bulk of the porous inserts.

The flow visualisation system used to deliver fluorescein dye into the recirculation zone consists of an inner chamber (green dashed lines in figure 1) and narrow slit (green solid lines in figure 1) extending upstream of the replaceable insert ( $x \leq -L_p$ ). The slit forms a narrow gap ( $0 \leq y < 0.5$  mm) above the level of the outlet floor that is connected with the inner chamber by spanwise-aligned row of small vertical holes ( $\phi_{hole} < 0.4$  mm) shifted by 2.5 mm along the  $z$  direction. As a result, dye is gently injected from the inner chamber perpendicularly downwards towards the floor, and then distributed to the recirculation zone through the narrow slit.

The main campaign of measurements consists of two realisations for each of the four different insert configurations under consideration. These two different realisations will be distinguished by grey and black marker edges on the plots presented in the following. Each realisation consists of series of measurements, during which the free-stream velocity  $U_0$  (and, thus, Reynolds number) is changed. Velocity fields were measured with a two-dimensional PIV system that consists of a Litron Nano L200-15 laser (double-headed, 532 nm light, 1200 mJ energy per pulse), Imager sCMOS camera (16-bit,  $2560 \times 2160$  pix) and Davis 8.1 Lavisision software. We acquire single-frame image sequences and cross-correlate five consecutive images with temporal Gaussian weighting using  $48 \times 16$  pixel interrogation windows with 4 : 1 elliptical Gaussian weighting along the streamwise direction and with 50% overlap. A rectangular interrogation window was achieved by stretching acquired images three times in the wall-normal direction using cubic interpolation. This provides us with spatial resolution of  $0.59h$  and  $0.19h$  along the streamwise and wall-normal direction, respectively. For each measurement we adjust acquisition frequency from 10 to 30 Hz (depending on  $U_0$ ) to retain the time correlation between two consecutive snapshots. Resulting time shift between two snapshots equals approximately 0.7 advective time units ( $t_{adv} = h/U_0$ ). For comparison, a typical time scale of Kelvin–Helmholtz instability in our experiment was measured as  $\approx 16$  advective time units. Unless otherwise stated, for all PIV measurements presented in this paper, the 1.5-mm-thick laser sheet is aligned with the  $z = 0$  plane.

Unless otherwise stated, all quantities are normalised using the step height ( $h$ ) and free-stream velocity of the incoming boundary layer at the separation edge ( $U_0$ ). We investigate the dynamics of BFS varying the Reynolds number, which is the main control parameter in our study defined as  $Re_H = U_0 h/\nu$ , with  $\nu$  as the kinematic viscosity of water at room temperature.

Experiments were performed in a closed-loop water channel at Warsaw University of Technology, with the working fluid at room temperature. The experimental set-up has been already described elsewhere (Klotz, Gumowski & Wesfreid 2019). The experiment described therein has been slightly modified by inserting a 5-cm-thick block of rectified foam (10 PPI) upstream of the honeycombs screens. This allows us to keep background velocity fluctuations measured in the central part of free-stream below 1.7% up to  $U_0 \approx 15 \text{ cm s}^{-1}$ . The bulk free-stream velocity is evaluated with calibrated PIV measurements and controlled by a large needle valve with an absolute setting precision of approximately  $\Delta Re_H = \pm 5$ .

The principal source of Reynolds number errors originates from the uncertainty of the determination of the free-stream velocity (<1.7%), which adds stochastic variation on the control parameter within each series of measurements. The second error source is related to the inaccuracy of the step height determination (<2.5%), which is independent of the Reynolds number and remains fixed for a given insert configuration. Therefore, it does not affect trend lines observed when the control parameter is changed other than the rescaling of abscissas of all data points in a series of measurements by a fixed constant. The third source of error originates from the limited control precision of the valve, which is less than the actual accuracy for the determination of the control parameter value. It reflects that it is substantially easier to measure the current Reynolds number than to set one specific value during the experiment. For this reason, for each series of experiments we systematically varied the Reynolds number to cover the full range of interest in our study (see e.g. Klotz *et al.* 2014, 2019). In addition, we performed two independent series of measurements for each insert configuration. Finally, we verified that for a given flow regime, the BFS flow does not change substantially with a small variation of the control parameter.

### 3. Experimental results

We first present flow visualisations (streaklines) to illustrate qualitatively flow dynamics behind BFS in the early transitional regime. Fluorescein dye was excited by a point source of visible white light and released into the recirculation zone through a narrow slit at the bottom corner edge of the step geometry (see the green thin solid line for  $x < -L_p$  and  $y > 0$  in figure 1). Instantaneous qualitative pictures of structures formed downstream of the separation edge are shown in figure 2 (top view) and figure 3 (side view). Flow visualisations are presented for a solid insert with impermeable walls (reference case, panels *a,b*) along with 10 PPI porous insert configuration (panels *c,d*). To enhance the contrast, for each presented picture we subtract the light intensity of the background acquired for the BFS flow with no injection of the dye. The images are captured with a single Nikon D610 camera ( $6016 \times 4016$  pix matrix) and a mirror inclined at  $45^\circ$  to the horizontal plane. At low Reynolds number ( $Re_H = 290$ ) both porous and solid configurations exhibit streamwise-elongated filaments of dye. This will be discussed further in § 5. Once Reynolds number is further increased to  $Re_H = 510$ , spanwise-coherent roller-like structures can be observed that dominate the temporal dynamics of the BFS flow. In the presence of a porous insert, these structures are shed more regularly and more frequently when compared with the reference case with solid impermeable walls. In the following part of § 3 and § 4, we characterise the unsteady dynamics of these spanwise-coherent structures formed downstream of the separation edge of BFS flow.

Dovgal *et al.* (1994) analysed the local linear stability of the local streamwise velocity profiles in streamwise-inhomogeneous BFS flow and referred to the observed structures

*Influence of porous material on the flow behind a BFS*

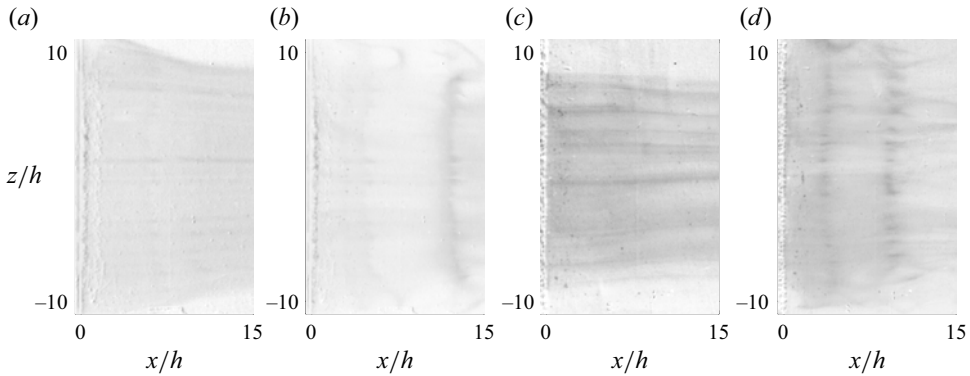


Figure 2. Top view of flow visualisations for solid impermeable insert (a,b) and permeable 10PPI porous insert (c,d). Two Reynolds numbers are shown:  $Re_H = 290$  (a,c) and  $Re_H = 510$  (b,d).

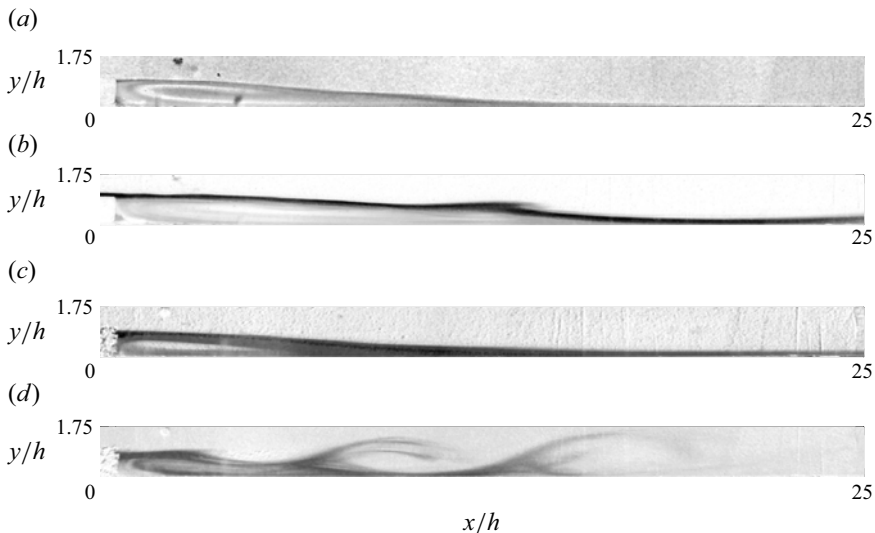


Figure 3. Same as figure 3 but for a side view: (a) solid,  $Re_H = 290$ ; (b) solid,  $Re_H = 510$ ; (c) 10 PPI,  $Re_H = 290$ ; (d) 10 PPI,  $Re_H = 510$ . The recirculation bubble downstream of the separation line can be observed qualitatively on each panel.

as (local) instability waves. In the global mode framework, Marquet *et al.* (2008) characterised wave packet in the form of vortical structures with an alternating sign of spanwise vorticity in the vicinity of the locus of inflectional points, which are amplified and grow in space while travelling along the recirculation zone. Cantwell & Barkley (2010) and Marais *et al.* (2011) investigated the wake behind a cylinder, which is another example of streamwise-inhomogeneous flow configuration. They observed that the wave packet amplified within the recirculation zone in the subcritical regime consists of the street of vortices with a similar spatial structure to Bénard–von Kármán street in the supercritical regime, i.e. above the critical threshold of sustained oscillations. Finally, we also note that any measurable finite-amplitude instability wave with non-zero oscillation frequency must alter the underlying base flow inducing some surplus vorticity fluctuations  $\omega'_z$ , which, in

turn, manifest as vortical structures. For this reason, we refer to finite-amplitude instability waves and vortical structures interchangeably as BFS structures in the following.

Next, we evaluate quantitatively BFS flow dynamics for  $Re_H \in (230, 850)$  using a PIV method with measurement region covering  $x/h \in (0, 50h)$  and  $y/h \in (0, 3.0h)$ . Each measurement series consists of a sequence of 2500 snapshots covering approximately 1750 advective time units. We investigate three porous inserts made of 10 PPI, 20 PPI and 45 PPI rectified foams, along with a solid Plexiglas insert as the reference case. For each configuration, two independent realisations are taken to assess the robustness of the analysis and to evaluate possible sensitivity to external noise in the installation. Flow visualisations in figures 2 and 3 and PIV measurements presented in the following were acquired in different runs.

The instantaneous spatial distribution of streamwise ( $u/U_0$ ) and wall-normal ( $v/U_0$ ) velocity components measured with the PIV technique are presented in figures 4 and 5, respectively. The spatial distribution of instantaneous vorticity fluctuations (the difference between instantaneous and time-averaged vorticity fields denoted as  $\omega'_z$ ) is illustrated in figure 6. Each column corresponds to a single Reynolds number,  $Re_H \in (290, 410, 510)$  from left to right. Each of the presented fields is extracted from a different series of measurements and variations between the actual Reynolds numbers resulting from an absolute setting precision of the controlling valve is approximately  $\Delta Re_H = \pm 5$ . Rows represent solid Plexiglas, 45 PPI and 10 PPI porous insert configurations, from top to bottom. In addition, on each panel we superpose time-averaged recirculation zones (dashed magenta curve) and the locus of inflectional points of time-averaged streamwise velocity profiles (dashed magenta curve). Specifically, the regions of reversed flow downstream and below the separation edge are observed for all insert configurations.

Laminar featureless flow at low Reynolds number is presented in the left columns of figures 4–6. The central columns illustrate the flow at sufficiently high  $Re_H$ , above which a spatially periodic pattern of BFS structures can be observed. The right columns represent the flow at a further increased Reynolds number, at which distinct spatially periodic patterns are preserved. These BFS structures manifest by waviness of the streamwise velocity component (figure 4), street of coherent regions of vertical velocity with alternating signs (figure 5) and street of alternating vorticity fluctuations along the streamwise direction (figure 6). A comparison between left and central columns indicates a bifurcation leading to the formation of the finite-amplitude structures downstream of the separation edge for sufficiently large Reynolds numbers. The quantitative analysis of this bifurcation, which includes the determination of the thresholds using the Landau model, are presented in § 4.

Our observation that spatial periodic structure is most pronounced on the vertical component  $v/U_0$  agrees with former numerical results (see e.g. Blackburn *et al.* 2008; Marquet & Sipp 2012; Boujo & Gallaire 2015). In addition, the structure of the perturbation consists of elliptical shapes with major axes aligned with the vertical and horizontal directions, in agreement with Blackburn *et al.* (2008). Moreover, Cantwell & Barkley (2010) and Marais *et al.* (2011) demonstrated that cross-flow (wall-normal) velocity component is a good representation of vortical structures observed both below and above the critical threshold of the Bénard–von Kármán street in the wake behind a cylinder. For these reasons in the rest of the paper we concentrate our analysis on  $v/U_0$ , in analogy with the analysis of a cylinder wake (Marais *et al.* 2011) or jet in a cross-flow (Megerian *et al.* 2007; Klotz *et al.* 2019).

### Influence of porous material on the flow behind a BFS

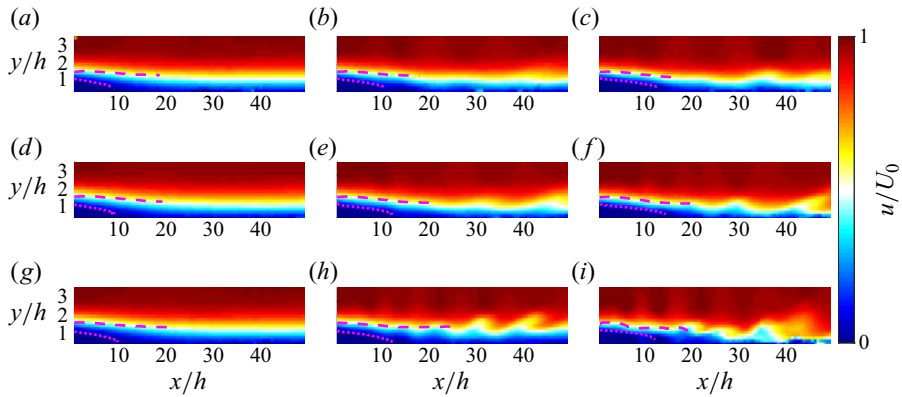


Figure 4. Instantaneous streamwise velocity component ( $u/U_0$ ) measured with a two-dimensional PIV technique for solid (a–c), 45 PPI (d–f) and 10 PPI (g–i) insert configurations, from top to bottom. The first (a,d,g), second (b,e,h) and third (c,f,i) columns correspond to  $Re_H = 290$ ,  $Re_H = 410$  and  $Re_H = 510$ , from left to right. In each panel, the locus of the inflectional point in the shear-layer profiles (magenta dashed line) and recirculation zone (magenta dotted line) are superposed.

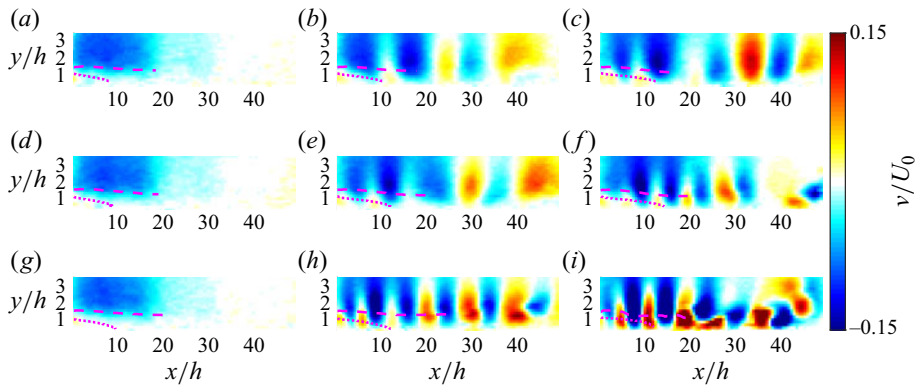


Figure 5. Same as in figure 4 but for instantaneous wall-normal velocity component ( $v/U_0$ ): for solid (a–c), 45 PPI (d–f) and 10 PPI (g–i) insert configurations, from top to bottom. The first (a,d,g), second (b,e,h) and third (c,f,i) columns correspond to  $Re_H = 290$ ,  $Re_H = 410$  and  $Re_H = 510$ , from left to right.

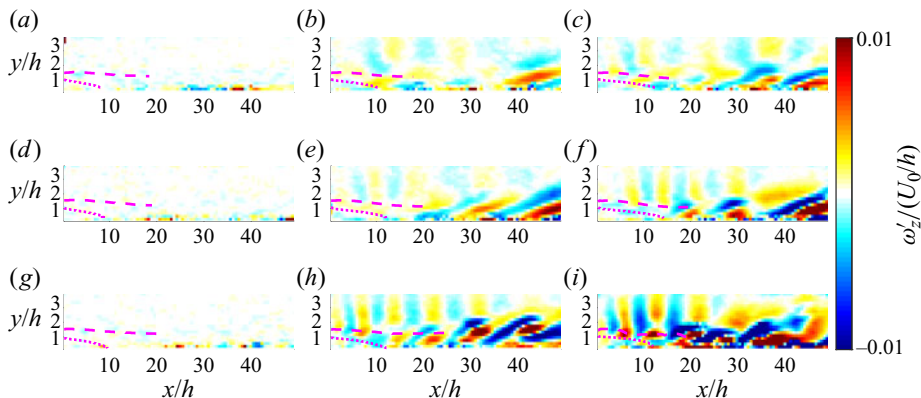


Figure 6. Same as in figure 4 but for instantaneous spanwise vorticity fluctuations ( $\omega'_z/(U_0/h)$ ) defined as the difference between instantaneous and time-averaged spanwise vorticity fields: for solid (a–c), 45 PPI (d–f) and 10 PPI (g–i) insert configurations, from top to bottom. The first (a,d,g), second (b,e,h) and third (c,f,i) columns correspond to  $Re_H = 290$ ,  $Re_H = 410$  and  $Re_H = 510$ , from left to right.

#### 4. Spectral analysis

For each spatial location  $(x, y)$  we perform temporal fast Fourier transform (FFT) analysis of the  $v(t)/U_0$  signal. The long sequence of measurements is divided into nine subsequences without overlap and with duration of  $\approx 200$  advective time units each. This covers more than 12 full periods of Kelvin–Helmholtz instability. All subsequences are ensemble-averaged to obtain the final spatial distribution of amplitude  $A_{FFT}/U_0$  for each frequency in the spectrum. First, we extract spatio-spectral diagrams at wall-normal locations, at which standard deviation in time of  $v/U_0$  reaches the maximum. Dependence of the Strouhal number ( $St_H = (fh)/(U_0)$ ) on streamwise location is shown in [figure 7](#). Vertical lines can be distinguished on these diagrams, which demonstrates the existence of global coherent spectral modes with well-defined characteristic Strouhal number that prevails along the streamwise direction in the separated shear layer formed behind the BFS. Their spectral amplitudes reach the maximal value at some finite distance from the separation edge ( $15h - 25h$ , depending on  $Re_H$  and porous insert configuration) and subsequently decay. This is in analogy with the global mode evolution observed in the wake of a cylinder (Goujon-Durand, Jenffer & Wesfreid 1994; Wesfreid, Goujon-Durand & Zielinska 1996), three-dimensional bluff bodies (Ormières & Provansal 1999; Klotz *et al.* 2014), jet in a cross-flow (Klotz *et al.* 2019; Chauvat *et al.* 2020) or hot free jet (Coenen *et al.* 2017). Our observations are also in agreement with Blackburn *et al.* (2008) who reported that non-trivial dynamics of the separated shear flow extends further downstream of the step, and is not solely determined by the initial roll-up of the shear layer at the separation edge.

Next, we average spatio-spectral diagrams over the streamwise direction  $x$ . Selected results for solid, 45 PPI, 20 PPI and 10 PPI insert configurations are shown in [figure 8\(a–d\)](#), from left to right. For the solid configuration, two characteristic Strouhal numbers can be distinguished: at low Reynolds numbers ( $Re_H = 325$  and  $Re_H = 365$ ), no peak at  $\approx 0.055$  can be distinguished and only a peak at  $St_H \approx 0.035$  is present. For  $Re_H = 460$ , a new weak peak emerges at  $St_H \approx 0.055$  and eventually it becomes the main peak in the spectrum for sufficiently large Reynolds number ( $Re_H = 675$ ). For the 45 PPI insert configuration, we observe analogical spectral shift but at lower Reynolds number when compared with solid insert configuration. For 20 PPI, a weak signature of lower characteristic Strouhal number can be distinguished only at the lowest  $Re_H$ , and for the 10 PPI configuration, a dominant peak occurs at  $\approx 0.055$  for the entire range of Reynolds numbers under consideration.

##### 4.1. Characteristic Strouhal numbers and frequency cross-over

For each insert configuration, Reynolds number and realisation, we determine a global dominant spectral peak (with positive frequency) and associated global peak of FFT amplitude ( $A_{FFT}$ ) within the entire area of measurements. In contrast to results shown in [figure 8](#), the data in [figure 9](#) do not include averaging along the streamwise direction. In [figure 9](#) we present the dependence of dominant  $St_H$  on  $Re_H$  for four insert configurations: solid insert (orange triangles), 45 PPI insert (violet squares), 20 PPI insert (green reversed triangles) and 10 PPI insert (blue circles). For each insert configuration different edge colours of the markers are used to distinguish between two independent series of measurements.

All measurement points can be grouped into two distinct spectral regions marked by dark-red ( $0.048 < St_{H2} < 0.070$ ) and light-blue ( $0.020 < St_{H1} < 0.042$ ) shaded areas.

## Influence of porous material on the flow behind a BFS

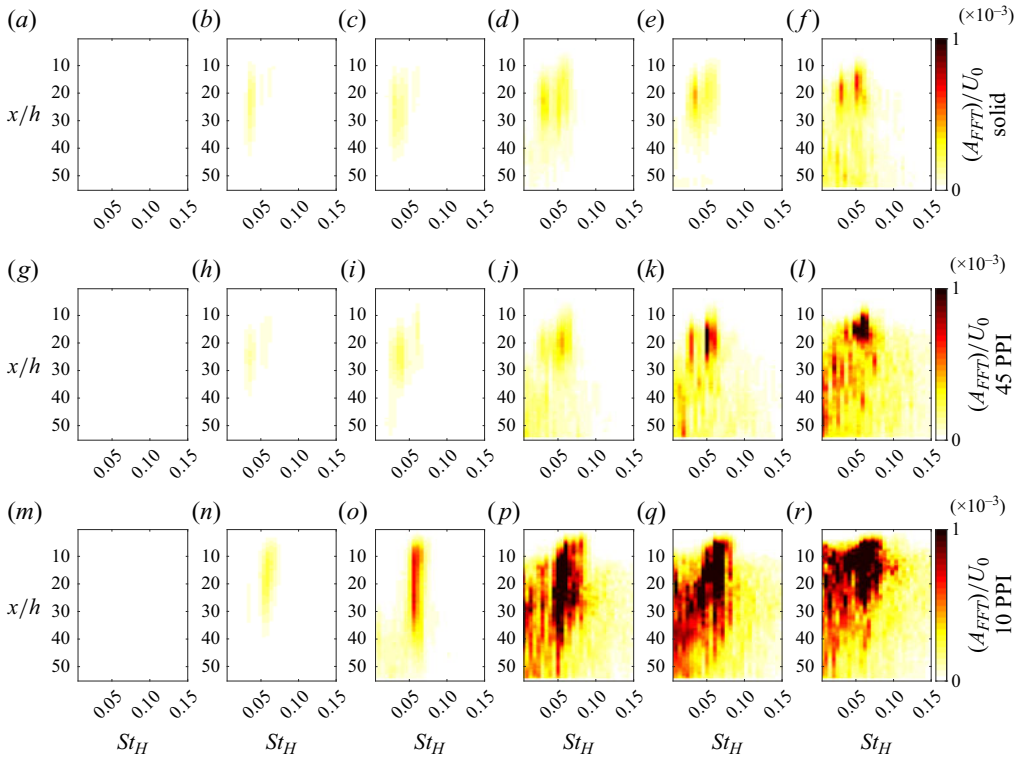


Figure 7. Spatio-spectral diagrams with normalised frequency ( $St_H$ ) on the horizontal and streamwise coordinate ( $x/h$ ) on the vertical axis for different  $Re_H$ : (a–f) solid, (g–l) 45 PPI and (m–r) 10 PPI porous configurations, from top to bottom; (a)  $Re_H = 295$ ; (b)  $Re_H = 365$ ; (c)  $Re_H = 405$ ; (d)  $Re_H = 515$ ; (e)  $Re_H = 575$ ; (f)  $Re_H = 675$ ; (g)  $Re_H = 285$ ; (h)  $Re_H = 365$ ; (i)  $Re_H = 410$ ; (j)  $Re_H = 505$ ; (k)  $Re_H = 580$ ; (l)  $Re_H = 685$ ; (m)  $Re_H = 290$ ; (n)  $Re_H = 365$ ; (o)  $Re_H = 405$ ; (p)  $Re_H = 510$ ; (q)  $Re_H = 570$ ; (r)  $Re_H = 700$ .

We ensemble-averaged all data points within each of these two spectral regions to obtain two characteristic central frequencies, which results in  $St_{H1} = 0.033$  and  $St_{H2} = 0.058$ . In the following, we refer to these characteristic frequencies and corresponding spectral amplitudes as spectral mode 1 and 2, respectively. Once the Reynolds number is increased, a cross-over between dominant Strouhal numbers and corresponding spectral modes can be observed. Estimated Reynolds numbers, at which this cross-over occurs, are marked by thick solid vertical lines in the same colours as the corresponding markers. Increasing permeability of the insert promotes frequency cross-over to occur at lower values of  $Re_H$ . Apart from the switch of dominating frequency, the characteristic Strouhal numbers do not depend on Reynolds number: despite some intrinsic scatter of the measured frequencies, the results fall on one of two horizontal trend lines for each realisation. In fact, some scatter is expected due to large potential for perturbation amplification in BFS (e.g. Blackburn *et al.* 2008; Marquet *et al.* 2008; Sipp *et al.* 2010; Dergham *et al.* 2013; Boujo & Gallaire 2015).

### 4.2. Bifurcation diagram of spectral amplitudes

In figure 10 we show a bifurcation diagram illustrating a dependence of squared amplitude of dominant FFT mode ( $E = A_{FFT}^2/U_0^2$  for the mode with positive frequency) on Reynolds

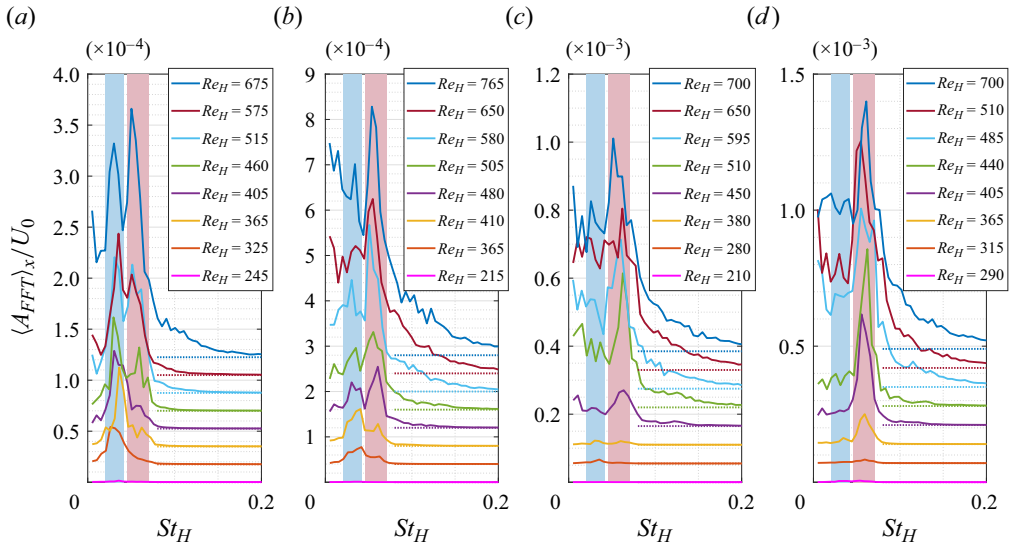


Figure 8. Selected spectra resulting from averaging spatio-spectral diagrams along the streamwise direction: (a) solid boundary configuration; (b) 45 PPI rectified foam configuration; (c) 20 PPI rectified foam configuration; (d) 10 PPI rectified foam configuration. The  $Re_H$  values are shown in corresponding legends on each panel.

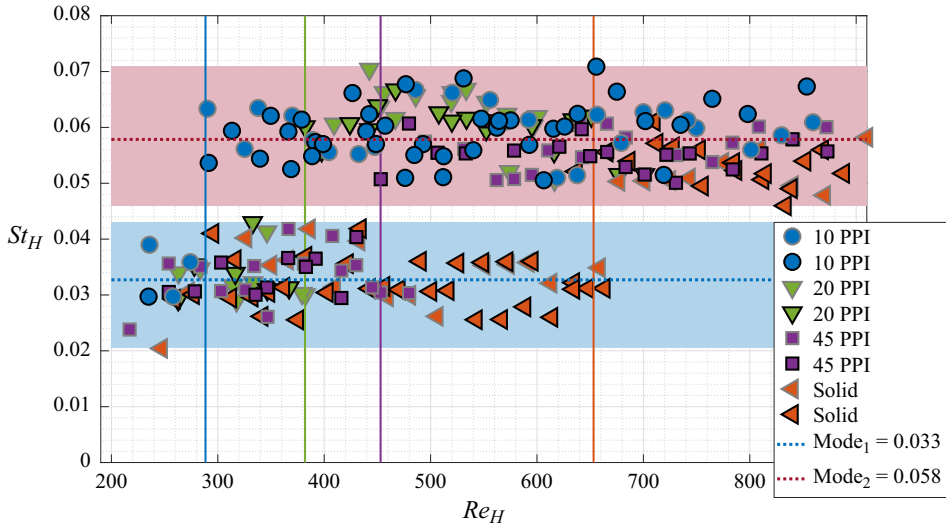


Figure 9. Dominant normalised frequencies  $St_H = fh/U_0$  for each realisation and each configuration as a function of the control parameter  $Re_H$ . Light blue and dark red semi-transparent areas indicate two main spectral regions, in which data points are grouped. Orange triangles, violet squares, reversed green triangles and blue circles correspond to solid, 45 PPI, 20 PPI and 10 PPI insert configurations, respectively. Black and grey edges of the markers indicate two different series of measurements for each porous insert configuration. Solid vertical lines in corresponding colours mark the frequency cross-over from lower to higher frequencies.

number  $Re_H$ . All markers, colours and solid vertical lines are the same as in figure 9. Each subsequent configuration is shifted upwards by 0.0012 to increase readability of the plot and zero reference levels are marked by horizontal dotted lines in corresponding colours.

### Influence of porous material on the flow behind a BFS

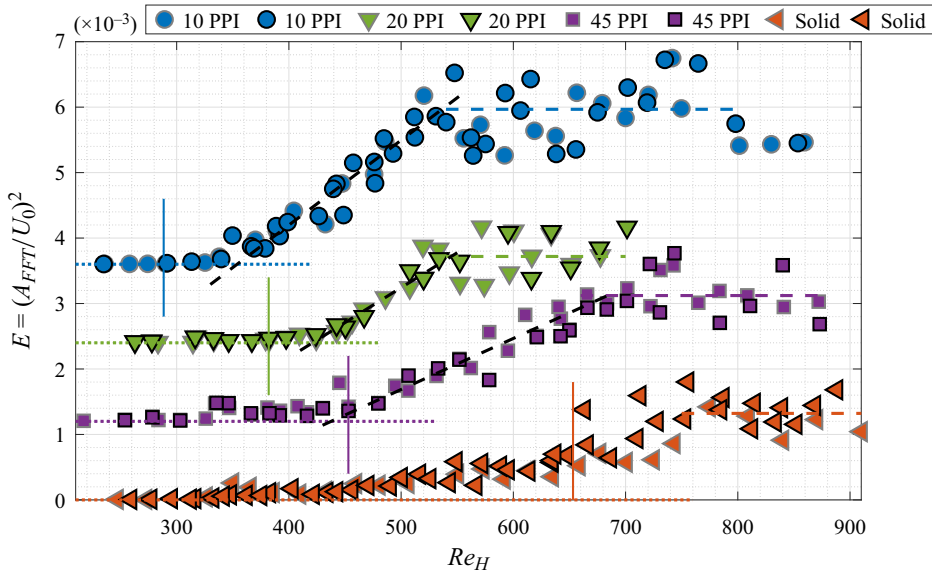


Figure 10. Dependence of the dominant spectral mode amplitude on control parameter  $Re_H$  for a solid insert (orange triangles), 45 PPI (violet squares), 20 PPI (reversed green triangles) and 10 PPI (blue circles) porous inserts. Solid vertical lines indicate the frequency cross-over from spectral mode 1 to spectral mode 2. Linear increase of the squared amplitude of the dominant spectral mode is marked by a black dashed line for all three porous inserts. Horizontal dashed lines in corresponding colours indicate energy saturation of the dominant mode for higher Reynolds numbers. Series of measurements for each subsequent configuration is shifted upwards by 0.0012 to increase readability of the plot and zero reference levels are marked by horizontal dotted lines in corresponding colours.

For all four insert configurations, the squared amplitude of the dominant mode reaches fully saturated value at sufficiently large Reynolds number. This is marked by horizontal dashed lines in corresponding colours. Similar saturation of the dominant frequency has been observed for wake behind a cylinder (Zielinska *et al.* 1997; Mantič-Lugo *et al.* 2014).

However, the dependence of  $E(Re_H)$  prior to the fully saturated regime is different for a solid insert when compared with the three porous configurations. Specifically, for 10 PPI, 20 PPI and 45 PPI inserts,  $E$  is close to zero at low enough Reynolds numbers (blue circles, green triangles and violet squares in figure 10). Once the Reynolds number exceeds some critical value  $Re_c$ , the squared amplitude of dominant mode ( $E$ ) starts to grow proportionally to the distance from the threshold, as indicated by black dashed lines. This behaviour of the order parameter agrees with the Landau model and indicates the occurrence of Hopf bifurcation at  $Re_c$ . We determined threshold values for each porous insert by interpolating linear growth of  $E(Re_H)$  to zero. This results in  $Re_c \approx 350$  for 10 PPI,  $Re_c \approx 420$  for 20 PPI and  $Re_c \approx 450$  for 45 PPI. In contrast, for the solid insert (orange triangles in figure 10), the squared amplitude of the dominant mode grows gradually with no visible change of growth trend once the Reynolds number is increased.

Furthermore, for all porous insert configurations the frequency cross-over (blue, green and violet solid vertical lines in figure 10) occurs prior to the threshold  $Re_c$  associated with Hopf bifurcation. This demonstrates that entire growth of  $E$  presented on this bifurcation diagram can be attributed to the dominating spectral mode 2. In contrast, for a solid insert the frequency cross-over is observed only when  $E$  reaches approximately half of its final

saturated value showing that both spectral modes 1 and 2 contribute to the growth of  $E$  presented in [figure 10](#).

According to the Landau model, the amplitude of the oscillations is zero below the critical threshold and starts to grow when the control parameter exceeds the critical Reynolds number, with its squared value proportional to the distance from the critical threshold (i.e.  $(A_{FFT})^2 \sim (Re - Re_C)$ ). This transition is due to Hopf bifurcation associated with a linear instability of the base flow with non-zero frequency at the critical threshold. The exponential growth of instability for finite values of  $Re - Re_C$  is reduced to zero through a nonlinear cubic term in the Landau equation, which results in finite-amplitude oscillations (i.e. limit cycle). In our experiment, the amplitude  $A_{FFT}$  of dominating spectral mode 2 follows the prediction of the Landau model for all porous inserts. In contrast, our experimental data do not clearly support the existence of a supercritical limit cycle for the solid insert configuration. Our observations thus support the suggestion of Marquet *et al.* (2009) who postulated that the recirculation zone behind the step can be an optimal location for a passive control device.

#### 4.3. Spatial support for spectral modes: Hilbert transform

In [figures 11](#) and [12](#), we illustrate the spatial distribution of envelope amplitudes associated with spectral modes 1 and 2, respectively. The envelopes are calculated using Hilbert transform for spectral ranges marked by light-blue and dark-red semi-transparent areas in [figure 9](#). Difference between the spatial distribution of envelopes 2 and 1 is illustrated in [figure 13](#): blue and red colours represent the regions dominated by spectral modes 1 and mode 2, respectively. Columns in [figures 11–13](#) correspond to  $Re_H \in (290, 410, 510)$  with  $\Delta Re_H = \pm 5$ , from left to right. Rows are associated with solid, 45 PPI and 10 PPI porous insert configurations, from top to bottom.

For the solid insert configuration, the average spatial intensity of envelope 1 is larger than envelope 2, in agreement with [figures 9](#) and [10](#). The first row in [figures 11](#) and [13](#) indicate that this dominance is mostly pronounced downstream the reattachment of the separated shear layer, with maximal value located slightly above the separation edge ( $y > h$ ). However, envelope 2 can locally dominate in the vicinity of the recirculation zone marked as dotted magenta curves.

Spatial envelopes for 45 PPI are shown in the second row of [figures 11–13](#). Below the threshold of limit cycle oscillations ( $Re_H < Re_c \approx 450$  for 45 PPI), spatial distribution of the envelope difference is similar to the solid insert configuration with the dominance of envelope 1 downstream of the reattachment line, as illustrated in [figure 13\(d,e\)](#) (compare with [figure 13\(a–c\)](#) for the solid insert configuration). However, for  $Re_H = 510$ , envelope 2 starts dominating downstream of the reattachment ([figure 13f](#)). Similar transition of the spatial envelope structure with increasing  $Re_H$  is also observed for 10 PPI in the third row of [figure 13](#). Below the critical threshold ( $Re_H < Re_c \approx 350$  for 10 PPI), envelope 1 is dominating downstream ([figure 13g](#)), whereas above this threshold the intensity of envelope 2 overtakes in the entire region of measurements with a maximal value slightly above the locus of inflectional points marked by a dashed magenta curve ([figure 13h,i](#)).

To further characterise the streamwise dependence of both envelopes, we calculate their mean value along the wall-normal direction for each streamwise location  $x/h$ . The results are presented in [figure 14](#): solid, 45 PPI, 20 PPI and 10 PPI porous insert configurations are shown in the rows from top to bottom; left and right columns represent envelopes

*Influence of porous material on the flow behind a BFS*

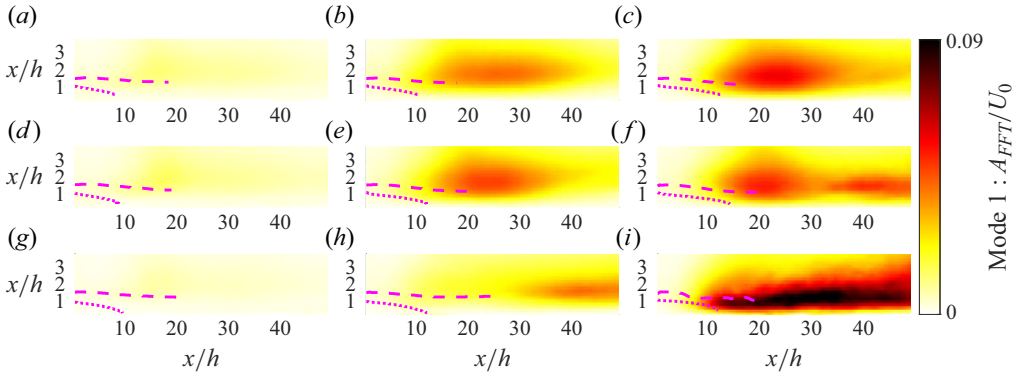


Figure 11. Time-averaged spatial envelope reconstructed using Hilbert transform on the spectral range corresponding to mode 1. Solid insert, 45 PPI and 10 PPI porous insert configurations are presented in (a–c), (d–f) and (g–i), from top to bottom. Panels (a,d,g), (b,e,h) and (c,f,i) correspond to  $Re_H \in (290, 410, 510)$ , from left to right. On each field, magenta dotted and dashed curves are superposed to mark the time-averaged recirculation zone and locus of inflection points of time-averaged streamwise velocity profiles. Compare with figures 4–6.

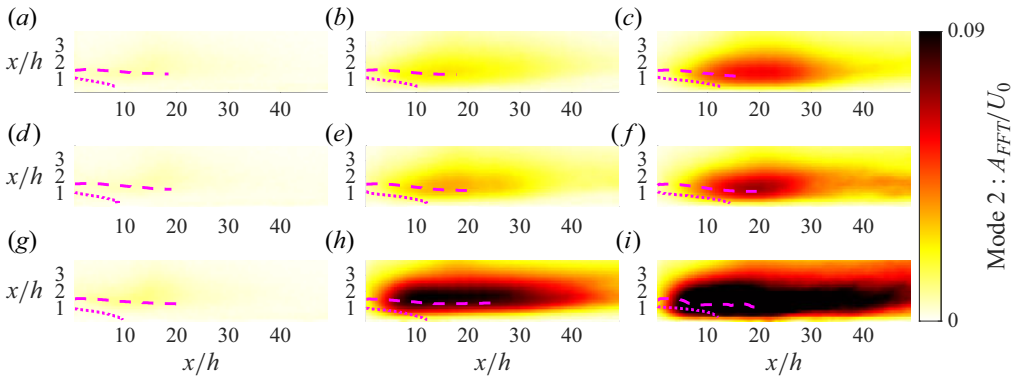


Figure 12. Same as figure 11 but for spectral range corresponding to mode 2: solid insert, 45 PPI and 10 PPI porous insert configurations are presented in rows (a–c), (d–f) and (g–i), from top to bottom. Columns (a,d,g), (b,e,h) and (c,f,i) correspond to  $Re_H \in (290, 410, 510)$ , from left to right.

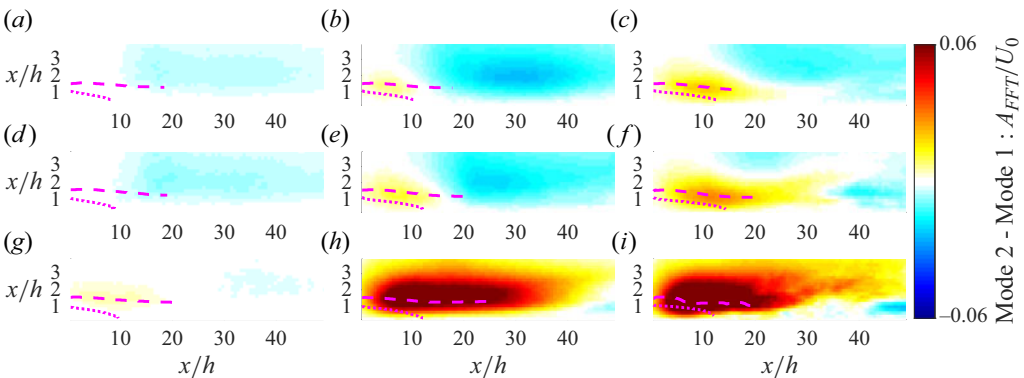


Figure 13. Difference between spatial support of spectral mode 2 and spectral mode 1 envelopes: solid insert, 45 PPI and 10 PPI porous insert configurations are presented in rows (a–c), (d–f) and (g–i), from top to bottom. Columns (a,d,g), (b,e,h) and (c,f,i) correspond to  $Re_H \in (290, 410, 510)$ , from left to right.

1 and 2, respectively. On each panel, we present the streamwise envelope intensity for several selected values of  $Re_H$ , the values of which are listed in legends on the right.

For solid insert configuration, both envelopes reach a global maximum at  $x/h \approx 20$  and their dependence along the streamwise direction is similar (figure 14a,b). In addition, the spatial peak of envelope 1 is larger than that of envelope 2 up to  $Re_H = 675$  (blue circles in figure 14a,b), in agreement with the frequency cross-over shown in figure 9. After initial streamwise growth, the amplitude of envelope 1 tends to reach a constant equilibrium value further downstream. In addition, the global peak of envelope 1 for porous inserts (figure 14c,e,g) does not change significantly when compared with the solid insert configuration (figure 14a).

In contrast, porous inserts heavily influence BFS structures characterised by the spectral range of mode 2. Envelope 2 for all porous inserts is characterised by non-monotonic streamwise evolution, reaching their maximal value at some finite distance from the step and subsequently decaying further downstream. In addition, the streamwise location of the global peak shifts upstream with increasing  $Re_H$ , in analogy with Mantič-Lugo & Gallaire (2016a). This streamwise evolution of envelope 2 for porous inserts is similar to the spectral mode evolution shown in figure 7.

The different streamwise evolutions of envelopes 1 and 2, combined with their different spatial support observed for porous inserts, indicate that the dynamics characterised by spectral range 2 is associated with the mixing-layer region in the vicinity of the recirculation zone. In contrast, envelope 1 corresponds to the dynamics of the boundary-layer region downstream of the reattachment of the separated shear layer.

#### 4.4. Origin of dominant spectral modes

Characteristic frequencies of mode 1 and mode 2 are nearly commensurate. We note that for solid insert configuration at low  $Re_H$  only mode 1 can be observed (see red curve for  $Re_H = 325$  in figure 8a). Significant peak corresponding to mode 2 can be detected in the spectrum only at larger values of  $Re_H$  (e.g. green curve for  $Re_H = 460$  in figure 8a). This shows that mode 1 is not a subharmonic of mode 2. Therefore, BFS dynamics is different from subharmonic resonance in free mixing layers, for which first subharmonic was least-stable secondary instability to the equilibrated train of primary vortices related to fundamental frequency.

Similarly, for 10 PPI insert configuration, mode 2 fully dominates the spectrum and very weak/no spectral signature of mode 1 can be distinguished (figure 8d). Moreover, mode 2 grows faster along the streamwise direction and reaches maximum closer to the separation edge when compared to mode 1 (figures 13 and 14), which indicates that mode 2 is not a higher harmonic of mode 1. This demonstrates that modes 1 and mode 2 are two separate spectral modes with two different characteristic frequencies. In this context, Boujo & Gallaire (2015) observed a transition of linear harmonic BFS response from one to two dominant frequencies once the expansion ratio is decreased from  $ER = 2$  to  $ER = 1.4$ . Our value of  $ER = 1.06$  is below the estimated transition range reported by Boujo & Gallaire (2015) and thus a two-peak response can be expected.

To better assess characteristic frequencies for each mode, we acquired few additional series of measurements for solid and 10 PPI porous inserts. We compute the spectra using a similar method as described in the first paragraph of § 4 but with 50 % longer time series for each sub-sequence. Then, we ensemble-averaged the results for all three long series of measurements. This allowed us to increase spectral resolution by 50 % when

*Influence of porous material on the flow behind a BFS*

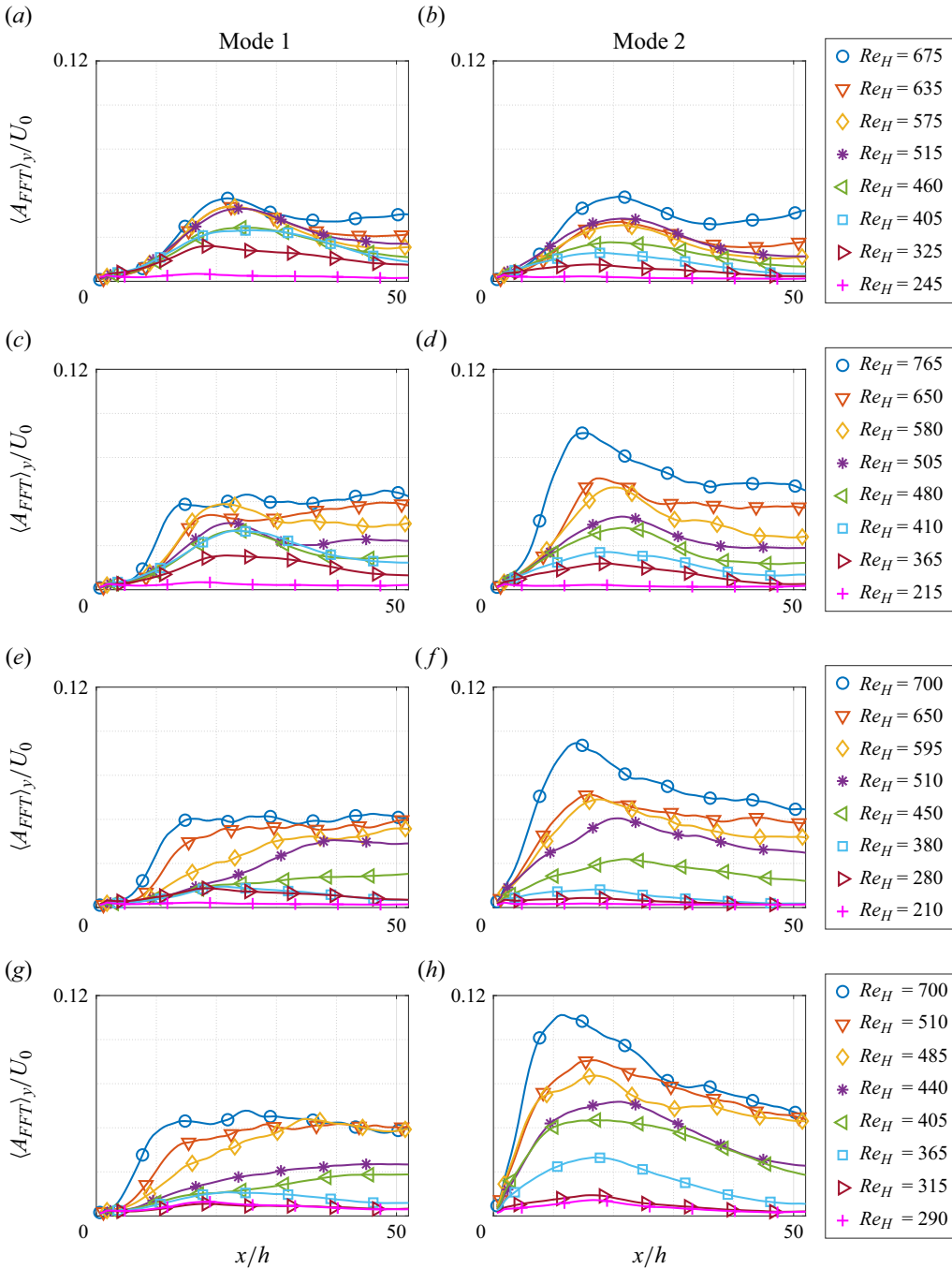


Figure 14. Streamwise dependence of amplitudes of envelope 1 (*a,c,e,g*) and envelope 2 (*b,d,f,h*). Panels (*a,b*), (*c,d*), (*e,f*) and (*g,h*) correspond to solid, 45 PPI, 20 PPI and 10 PPI porous inserts, from top to bottom. The  $Re_H$  values for each insert configuration are indicated in legends. Each point at a given  $x/h$  results from averaging envelopes shown in figures 11 and 12 in time and along wall-normal direction. All presented curves are smoothed along the  $x$  direction between three neighbouring points.

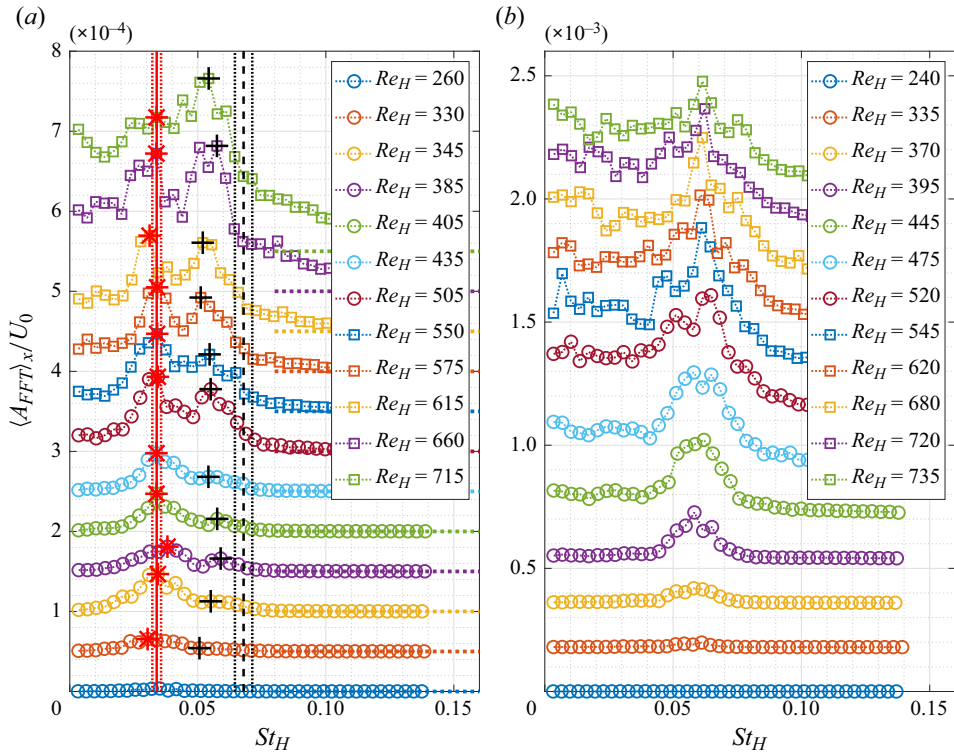


Figure 15. Spectra averaged along the streamwise direction for solid (a) and 10 PPI porous inserts (b). Each spectrum is ensemble-averaged over three different long series of measurements. This results in 50 % better resolution in frequency when compared with figure 8 and with higher signal-to-noise ratio at lower frequencies. Red solid and black dashed vertical lines illustrate the characteristic frequency of spectral mode 1 and its higher harmonic, respectively.

compared to the data presented in figure 8. Resulting spectra are presented in figure 15 with Reynolds numbers listed in the legends. This extended analysis confirms that at low  $Re_H$  BFS dynamics with solid insert is dominated by low-frequency mode 1 (red stars in figure 15a). As  $Re_H$  is increased the amplitude of mode 2 increases and eventually becomes dominant. Characteristic frequency of mode 1 remains constant as illustrated by red vertical solid line, with additional red dashed lines indicating the spectral resolution of FFT transform. Spectral range allowed for the first higher harmonic of mode 1 is marked in figure 15(a) as black vertical dashed line with black dotted vertical lines indicating the spectral accuracy for higher harmonic (twice the spectral resolution). Peaks of mode 2 (black crosses in figure 15a) lie outside the spectral range of the higher harmonic of mode 1 for all measured spectra, which confirms that mode 2 is not a higher harmonic of mode 1. Furthermore, on both panels in figure 15, the spectral range associated with near-zero frequency modes is relatively flat with no significant and robust peaks in the vicinity of zero frequency for investigated  $Re_H$  range and for our spectral resolution.

One can distinguish at least two more characteristic length scales in BFS flow different from step height  $h$ , such as momentum thickness ( $\theta_0$ ) of incoming boundary layer at the separation edge or displacement thickness ( $\delta_r$ ) close to the streamwise location where separated shear layer re-attaches. Momentum thickness is conventionally used in the context of free mixing shear layers (e.g. Ho & Huerre 1984), whereas displacement

## Influence of porous material on the flow behind a BFS

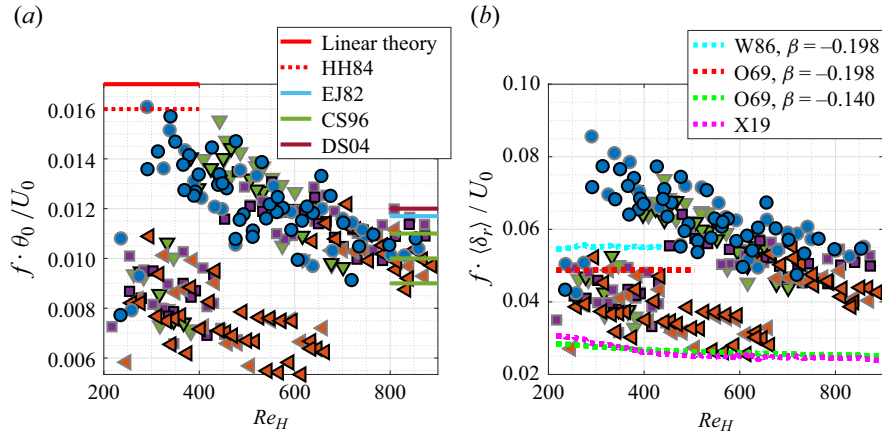


Figure 16. Strouhal numbers computed using different characteristic length scales: (a) momentum thickness at the separation edge,  $\theta_0$ ; (b) displacement thickness downstream of the reattachment,  $\langle \delta_r \rangle$ . Compared with figure 9 where step height  $h$  is used as the length scale. Horizontal red lines in (a) correspond to the most amplified frequency calculated using spatial local linear theory for the mixing layer (solid, Michalke 1965; Freymuth 1966; dashed, Ho & Huerre 1984). Horizontal non-red solid lines in (a) represent reported values for roll-up of the shear layer for BFS (Eaton & Johnston 1982; Chun & Sung 1996; Dovgal & Sorokin 2004). Dashed curves in (b) correspond to the most amplified frequency of the Falkner–Skan family of boundary layers with Hartree parameter  $\beta = -0.198$  (Obremski *et al.* 1969 in red; Wazzan, Taghavi & Pafford 1986 in cyan) and  $\beta = -0.140$  (Obremski *et al.* 1969 in green). Correlation proposed by Xu *et al.* (2019) is also superposed as magenta curve.

thickness is more frequently applied in boundary layer flow (e.g. Obremski *et al.* 1969; Ehrenstein & Gallaire 2005; Alizard, Cherubini & Robinet 2009; Monokrousos *et al.* 2010; Wedin *et al.* 2015). In figure 16(a,b) we present characteristic frequencies of both spectral modes normalised with  $\theta_0$  and  $\langle \delta_r \rangle$ , respectively.  $\langle \delta_r \rangle$  is calculated from streamwise velocity profile averaged along the streamwise direction starting from re-attachment ( $x_r$ ) and spanning  $2h$  downstream ( $x'_r = x_r + 2h$ ). Variation of both  $St_\theta(Re_H)$  and  $St_\delta(Re_H)$  illustrated in figure 16(a,b) is more pronounced than the variation of  $St_h(Re_H)$  presented in figure 9. This shows that for a given value of  $ER$ , step height  $h$  is the most appropriate length scale for BFS flow. However, independently of the selected characteristic length scale, all measured points group onto two distinct branches associated either with mode 1 (lower branch at the bottom of figures 9 and 16) or mode 2 (upper branch at the top of figures 9 and 16).

Local spatial stability analysis (Michalke 1965) along with experimental measurements in free mixing layer (Freymuth 1966) indicated that  $St_\theta = 0.017$  is the most unstable frequency amplified through inviscid Kelvin–Helmholtz instability due to inflectional point in the time-averaged streamwise velocity profile. Ho & Huerre (1984) reported about similar value of  $St_\theta = 0.016$  (note that here we transform their results using free-stream velocity  $U_0$  as the velocity scale). Both values are marked as red horizontal lines in figure 16(a). The largest  $St_\theta$  were measured at the frequency cross-over from mode 1 to mode 2, with maximal values of approximately 0.016, 0.015, and 0.014 for 10 PPI, 20 PPI, and 45 PPI, respectively. These values are in good agreement with linear stability prediction for free mixing shear layer, demonstrating that the maximal allowed value of  $St_\theta$  on the upper branch is bounded from above by the most unstable frequency of the shear layer at the separation edge. In addition,  $St_\theta$  on the upper branch decreases once the Reynolds number  $Re_H$  is increased, in analogy to the trend reported by Michalke

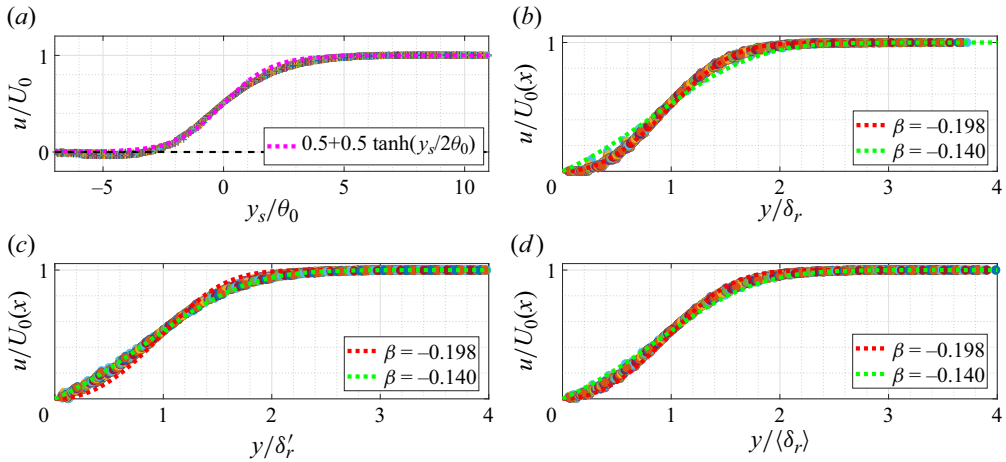


Figure 17. Time-averaged streamwise velocity profiles measured: (a) immediately downstream of the separation edge; (b) at re-attachment of separated boundary layer,  $x = x_r$ ; (c)  $2h$  downstream of the re-attachment, at  $x = x'_r = x_r + 2h$ ; (d) streamwise-averaged for  $x \in (x_r, x'_r)$ . Wall-normal coordinate  $y$  is normalised with momentum (a) and displacement (b–d) thickness computed separately for each presented location. Magenta curve in (a) represents free mixing shear layer solution ( $u(y) = 0.5 + 0.5 \tanh(y_s/2\theta_0)$ ). Dashed curves in (b–d) represent velocity profiles of Falkner–Skan boundary layer flow with Hartree parameter:  $\beta = -0.198$  (at the re-attachment of boundary layer; in red),  $\beta = -0.140$  ( $2h$  downstream the re-attachment; in green). In (b–d) velocity profiles with  $Re_H$  below the threshold of frequency cross-over are shown.

& Hermann (1982) for free jet. Our results on  $St_\theta$  for the largest Reynolds number under investigation ( $Re_H \approx 900$ ) compare well with the values reported by Eaton & Johnston (1982), Chun & Sung (1996) and Dovgal & Sorokin (2004) marked as horizontal non-red solid lines on the right of figure 16(a). Overall agreement between measured frequencies on upper branch frequencies and results reported for free mixing shear layer and BFS demonstrates that the upper branch associated with mode 2 corresponds to Kelvin–Helmholtz instability.

This is further demonstrated in figure 17(a), on which we plot time-averaged velocity profiles measured for all Reynolds numbers and all considered inserts (approximately 300 independent series of measurements). As already mentioned in the introduction, the dynamics of the perturbation at the separation edge in BFS shares similarity with the free-mixing shear layer. Therefore, the wall-normal coordinate is normalised with the momentum thickness of the boundary layer at the separation edge  $\theta_0$ . In addition, for each measured velocity profile the wall-normal locations were shifted by  $\Delta y$ , such that  $u(y_s) = 0.5U_0$  for  $y_s = y - \Delta y = 0$ . We also superpose classical hyperbolic-tangent mixing layer velocity profile ( $0.5(1 + \tanh(y_s/2\theta_0))$ ) illustrated by a thick dashed magenta curve. All the measured streamwise velocity profiles collapse to a single curve that compares well with a hyperbolic tangent. This demonstrates that immediately downstream of the separation edge, BFS dynamics can be considered as analogical to the free-mixing shear layer and dominated by Kelvin–Helmholtz instability, as already mentioned in the introduction.

In figure 16(b) we present characteristic frequency normalised with displacement thickness in the vicinity of the re-attachment of separated shear layer as a function of  $Re_H$ . The lower branch associated with mode 1 covers the spectral range of  $St_\delta \in (0.02 - 0.06)$ . We compare lower branch frequencies to the results derived from local linear stability analysis of Falkner–Skan family of boundary layer profiles, with Hartree parameter  $\beta$

that quantifies the intensity of the adverse pressure gradient. Specifically, we consider  $\beta = -0.198$  and  $\beta = -0.140$ .

First, we demonstrate the universal character of the streamwise velocity profiles in the vicinity of the reattachment of the separated shear layer. In [figure 17\(b–d\)](#) we select velocity profiles with  $Re_H$  below the threshold of frequency cross-over for which mode 1 is dominating. On each panel, we overlap all selected velocity profiles without distinguishing insert configuration, Reynolds number or realisation. Specifically, we consider streamwise location, at which separated shear layer reattaches ( $x_r$  in [figure 17b](#)), streamwise location located two steps heights downstream of the reattachment ( $x'_r = x_r + 2h$  in [figure 17c](#)) and velocity profile averaged along the streamwise direction for  $x \in (x_r, x'_r)$  ([figure 17d](#)). For reference, we also superpose Falkner–Skan velocity profiles for  $\beta = -0.198$  and  $\beta = -0.140$  that represent local velocity profile at the reattachment (red dashed curve) and  $2h$  downstream of the separation line (green dashed curve), respectively. The wall-normal coordinate  $y$  is normalised by displacement thickness at the reattachment ( $\delta_r$  in [figure 17b](#)), displacement thickness  $2h$  downstream of the reattachment ( $\delta_{r'}$  in [figure 17c](#)), and displacement thickness of the velocity profile averaged along the streamwise direction  $x \in (x_r, x'_r)$  ( $\langle \delta_r \rangle$  in [figure 17d](#)). One can observe that the measured velocity profiles at  $x_r$  and  $x'_r$  compare well with Falkner–Skan velocity profiles with  $\beta = -0.198$  and  $\beta = -0.140$ , respectively.

The local intensity of the adverse streamwise pressure gradient associated with specific Hartree parameter  $\beta$  is a value that is required at a given streamwise location to preserve self-similarity of the Falkner–Skan solution along the streamwise direction. If, at any location, this value is lower than required, then the local velocity profile will relax further downstream towards a solution that is closer to the zero-pressure equilibrated boundary layer (i.e. towards a solution with  $\beta$  closer to zero). As already mentioned in the introduction, BFS flow is not self-similar along the streamwise direction and it represents spatial relaxation of free-mixing layer flow into an equilibrated boundary layer profile further downstream. This implies that the local intensity of the adverse pressure gradient is lower than required by the Falkner–Skan solution to preserve streamwise self-similarity. Furthermore, the agreement between one specific self-similar Falkner–Skan solution and measured velocity profiles occurs only locally at one specific streamwise location.

In [figure 17\(b–d\)](#) we established that velocity profiles in the vicinity of re-attachment can be locally spanned between Falkner–Skan solutions for  $\beta = -0.198$  and  $\beta = -0.140$ . Now we compare the measured spectral range of the lower branch with the most amplified frequencies of these two Falkner–Skan boundary layers. Obremski *et al.* (1969) studied local linear stability of the Falkner–Skan solution and presented in their [figure 10\(m,n\)](#) the dependency of the most amplified frequency of the Tollmien–Schlichting wave on the Reynolds number based on displacement thickness. However, they did not state  $f_{TS}(Re_\delta)$  dependency explicitly. The cusps of iso-contours shown in [figure 10\(m,n\)](#) from Obremski *et al.* (1969) fall on the straight line on a log–log scale. Therefore, we infer the coordinates of these cusps and fit a power-law dependence to estimate the missing  $f_{TS}(Re_\delta)$  dependency. Finally, we substitute the dependence of local values of  $Re_\delta(Re_H)$  measured in our experiments and compare with our spectral results.

The resulting spectral range for the most amplified frequencies of Tollmien–Schlichting waves is marked in [figure 16\(b\)](#) and spans from  $\beta = -0.198$  (red dotted curve) to  $\beta = -0.140$  (green dotted curve). We also superposed results reported by Wazzan *et al.* (1986, cyan curve) and Xu *et al.* (2019, magenta curve). Measured Strouhal numbers of the lower branch (mode 1) are contained within the spectral range bounded above by

the curves associated with  $\beta = -0.198$  (Obremski *et al.* 1969; Wazzan *et al.* 1986), and bounded below by the curve related to  $\beta = -0.140$  (Obremski *et al.* 1969) and correlation reported by Xu *et al.* (2019). Moreover, the largest measured values of  $St_\delta$  on a lower branch are in relatively good agreement with the most amplified frequency for  $\beta = -0.198$ . The streamwise velocity profile at this location is expected to be the least stable among all velocity profiles within the Falkner–Skan family of boundary layers (Obremski *et al.* 1969). This indicates that the mode 1 lower branch is related to the Tollmien–Schlichting instability.

We note that in contrast to the well-defined reattachment location  $x_r$ , the downstream limit  $x'_r$  for streamwise averaging has been selected arbitrarily. For any location selected further downstream than  $x'_r$ , the intensity of adverse pressure gradient would decrease (i.e.  $\beta$  closer to zero) and lower bound limit for  $St_\delta$  (green dotted curve in figure 16*b*) would shift closer to abscissa.

Regarding the relation between local and global stability analysis, Boujo & Gallaire (2015) investigated BFS flow with solid impermeable walls and  $ER = 2.0$ . They reported that the most amplified frequency response of BFS structures calculated using global stability analysis (i.e. incorporate streamwise eigendirection directly into eigenfunctions) agrees well with the most amplified frequency derived by integration along the streamwise direction of local amplification rates calculated independently for each streamwise location using local stability analysis (i.e. under the additional assumption of streamwise homogeneity at each streamwise location). This indicates that local stability analysis can provide meaningful criteria for the prediction of the most amplified perturbation frequency.

## 5. Measurements in cross-stream planes

Flow visualisations presented in figure 2(*a,c*) reveal weak streamwise-elongated structures, with spanwise wavelength that differs from the value reported by Barkley *et al.* (2002) and Lanzerstorfer & Kuhlmann (2012). To quantify their intensity, we performed additional PIV measurements with a laser sheet parallel to the  $y$ – $z$  plane at three different streamwise locations downstream of the separation edge. We used a 5-mm-thick laser sheet and 50 % larger ratio between acquisition frequency and free-stream velocity when compared with the measurements described in §2–§4. Each series of measurements consists of 1000 images captured using a low-height and wide mirror inclined at  $45^\circ$  to the lower bounding wall and located  $55h$  downstream from the separation edge. Acquired images are cross-correlated using  $64 \times 64$  pix with 75 % overlap integration window, and with Gaussian time-averaging of  $\pm 8$  images. Area of measurement covers  $y/h \in (0.0, 2.0)$  and  $z/h \in (-11.1, 11.1)$  with spatial resolution of  $0.22h$  in both wall-normal and spanwise directions.

In figures 18 and 19 we present time-averaged fields for  $Re_H = 280$  and  $Re_H = 380$ . Each panel consists of two images showing the streamwise vorticity ( $\omega_x h/U_0$ , top) and wall-normal velocity fields ( $v/U_0$ , bottom). Solid and 10 PPI configurations are presented in the left and right columns, respectively. Each row corresponds to one specific downstream location of the laser sheet:  $x/h = 10$ ,  $x/h = 20$  and  $x/h = 30$  downstream of the separation edge, from top to bottom. For our aspect ratio of  $AR \approx 26$  approximately one-third of the total spanwise extent of the test section in the centre remains free of the side-wall effects, which is marked by magenta dashed vertical lines. Time-averaged fields do not reveal any significant intensity of stationary streamwise vortices other than structures induced close to the side walls.

Influence of porous material on the flow behind a BFS

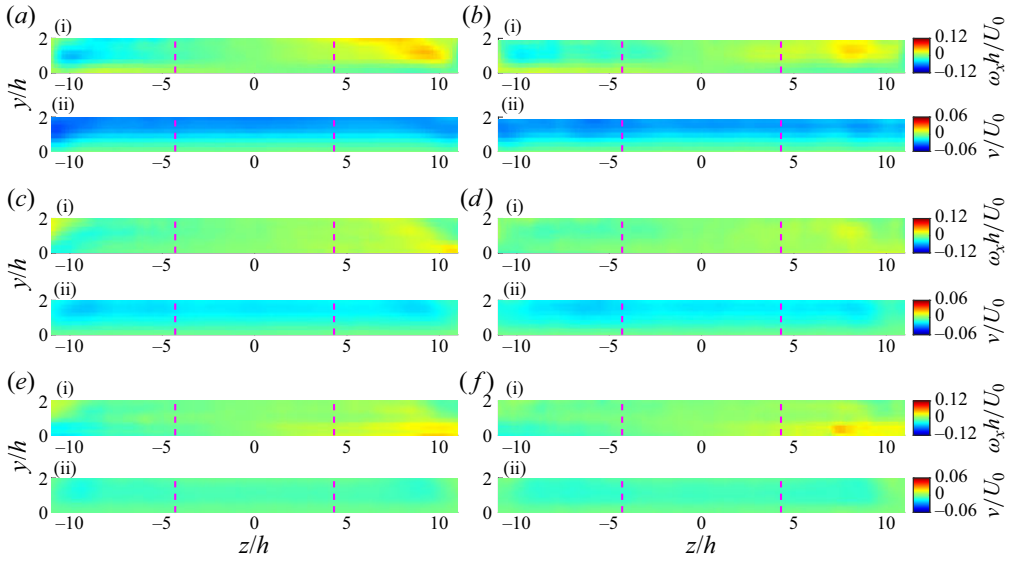


Figure 18. Streamwise vorticity ( $\omega_x h/U_0$ , part (i) in panels *a-f*) and time-averaged wall-normal velocity ( $v/U_0$ , part (ii) in panels *a-f*) fields measured for  $Re_H = 280$  with laser plane perpendicular to the streamwise direction: (*a,c,e*) and (*b,d,f*) solid and 10 PPI porous inserts, from left to right; (*a,b*), (*c,d*) and (*e,f*) different streamwise locations at which the laser plane is located,  $x/h = 10, 20, 30$  from top to bottom.

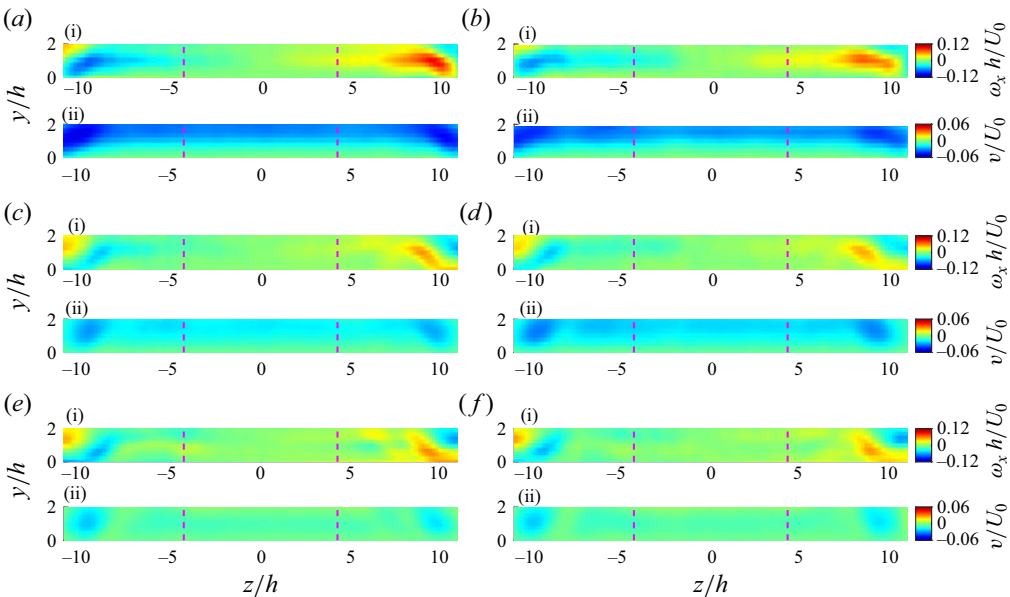


Figure 19. Same as in figure 18 but for  $Re_H = 380$ : (*a,c,e*) and (*b,d,f*) solid and 10 PPI porous inserts, from left to right; (*a,b*), (*c,d*) and (*e,f*) different streamwise locations at which the laser plane is located,  $x/h = 10, 20, 30$  from top to bottom.

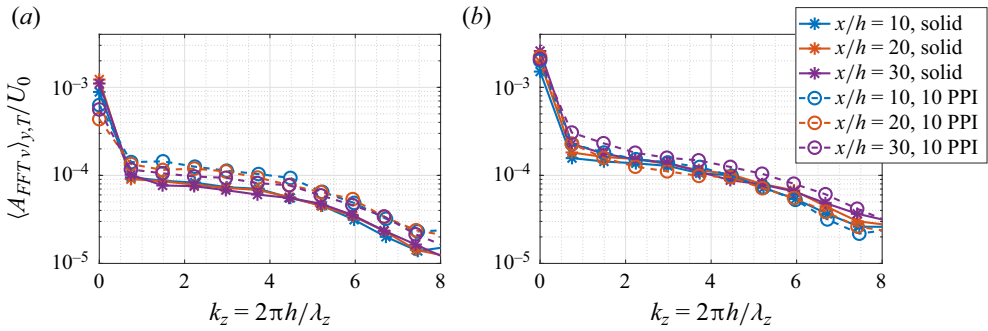


Figure 20. Spatial FFT spectra along the spanwise direction averaged in time and along the wall-normal direction. Results for  $Re_H = 280$  (a) and  $Re_H = 380$  (b) are shown. Stars and circles represent solid and 10 PPI porous inserts on both panels. Dark blue, red and violet colours indicate three different streamwise locations of cross-stream measurements:  $x/h = 10$ ,  $x/h = 20$  and  $x/h = 30$ , respectively.

In the next step, we analyse instantaneous vortical structures in the centre of the test section,  $z/h \in (-4.5, 4.5)$ . From series of instantaneous wall-normal velocity snapshots we subtract time-averaged fields,  $(v(t, y, z) - \langle v(y, z) \rangle_T) / U_0$ . Then, for each  $t$  and  $y$  we calculate instantaneous spatial FFT transform along the spanwise direction  $z$ , and we average the results in time and along the wall-normal direction. In figure 20 we present the resulting spatial spectra for spanwise wavenumber  $k_z$ . Left and right columns correspond to  $Re_H = 280$  and  $Re_H = 380$ , respectively. Stars and circles represent solid and 10 PPI porous insert configurations. Colour of the markers indicates three different streamwise locations of the laser plane:  $x/h = 10$  (blue),  $x/h = 20$  (red) and  $x/h = 30$  (violet). Spanwise organisation of the BFS structure in the central part of the test section is dominated by zero mode with uniform distribution along the  $z$  direction ( $k_z = 0$ ). In addition, some weak modes with non-zero spanwise wavelength ( $k_z \neq 0$ ) are present in the spectrum, with slightly more enhanced amplitude for 10 PPI porous insert configuration. This indicates that instantaneous vortical structures with spatial modulation along the spanwise ( $z$ ) direction are present in the BFS flow. However, their amplitude is typically one order of magnitude lower than the zero mode ( $k_z = 0$ ), which illustrates that dynamics of the BFS flow is dominated by quasi-two-dimensional roller structures.

## 6. Offset-side-plane and top-plane measurements

To further characterise the BFS flow, we performed two auxiliary campaigns of PIV measurements. The first campaign consists of side-view measurements in  $x$ - $y$  plane at four different  $z$  locations. The acquisition details of this auxiliary campaign are the same as that already described in § 2. We present the velocity fields measured for  $Re_H = 400$  in solid (figure 21) and 10 PPI porous (figure 22) configurations. The first two rows illustrate streamwise and wall-normal velocity components, with each panel composed of two subpanels representing time-averaged and instantaneous velocity fields. The third row demonstrates the spatial envelope of mode 1 (subpanels on the left) and mode 2 (subpanels on the right), in analogy with already-presented results in figures 11–13. Each column corresponds to one  $z$  location, with  $z/h \in (-3.8, -1.2, 1.4, 4.0)$  from left to right. Similarly to figures 4–6, we also superposed time-averaged recirculation zones and locus of inflectional points by magenta dotted and magenta dashed curves, respectively. We can

## Influence of porous material on the flow behind a BFS

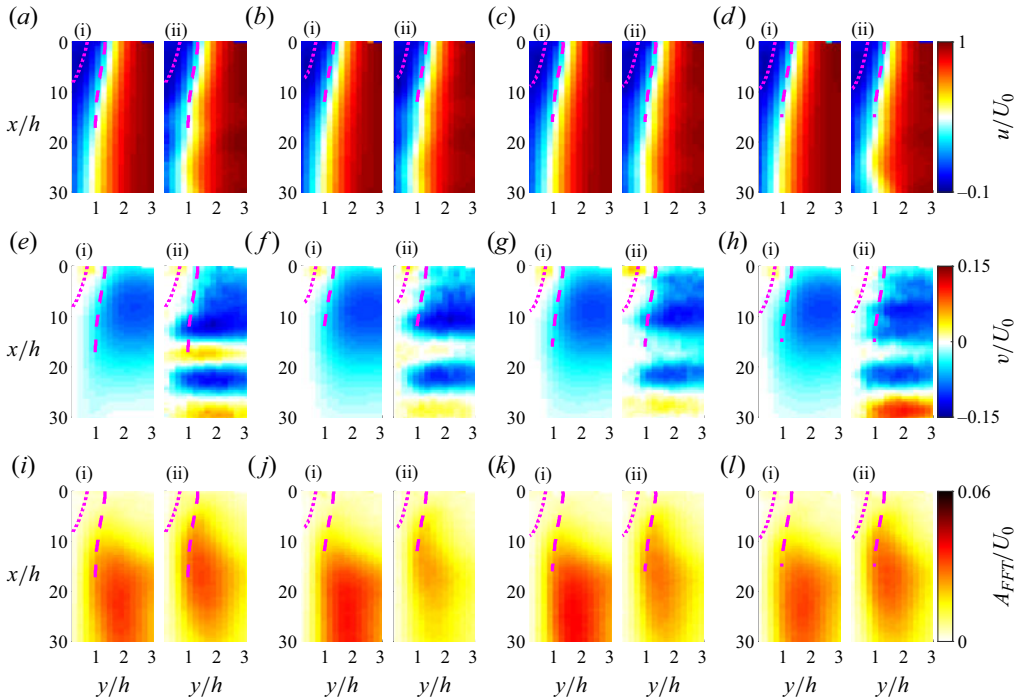


Figure 21. PIV measurements in  $x$ - $y$  planes at different  $z$  locations with solid impermeable configuration for  $Re_H = 400$ ; at four different spanwise locations:  $z = -3.8 h$  (panels *a,e,i*);  $z = -1.2 h$  (panels *b,f,j*);  $z = 1.4 h$  (panels *c,g,k*);  $z = 4.0 h$  (panels *d,h,l*). Panels (*a-d*) and (*e-h*) illustrate streamwise and wall-normal velocity components, respectively. Each panel in (*a-d*) and (*e-h*) consists of parts (i) and (ii) showing time-averaged and instantaneous velocity fields. Panels (*i-l*) correspond to spatial distribution of modes 1 and 2 presented in part (i) and (ii), respectively (compare also with figures 11–13). Time-averaged recirculation zones and locus of inflectional points are marked by magenta dotted and magenta dashed curves, respectively.

see that the structure of BFS flow does not change significantly with  $z$ , in agreement with the cross-stream measurements already discussed in § 5.

The second auxiliary campaign includes top view measurements in the  $x$ - $z$  plane at  $y/h = 0.7$ . This wall-normal location is close to the centre of the streamwise vortices reported by Barkley *et al.* (2002) for BFS with  $ER = 2$  and near the location discussed in detail by Giannopoulos (2021). A total 2500 images were acquired and cross-correlated using  $64 \times 64$  pix with 50% overlap integration window, and with Gaussian time-averaging of  $\pm 1$  images. Measuring area spans over  $x/h \in (0.0, 30.0)$  and  $z/h \in (-11.1, 11.1)$  with spatial resolution of  $0.29h$  in both streamwise and spanwise directions. In figure 23 we illustrate the spatial distribution of spanwise and streamwise velocity components measured for  $Re_H = 400$ . The first and third columns correspond to instantaneous velocity fields, whereas the second and fourth columns show time-averaged data. The top and bottom rows represent solid and 10 PPI porous insert configurations, respectively. In addition, dashed vertical lines indicate four spanwise locations corresponding to  $x$ - $y$  side planes presented in figures 21 and 22.

The central part of the test section near the symmetry plane  $z = 0$  is free of side-wall effects for solid impermeable configuration (figure 23*a,c*). This agrees with cross-stream measurements already presented in § 5. Specifically, in the central region no spanwise modulation of streamwise velocity components has been detected, in agreement with

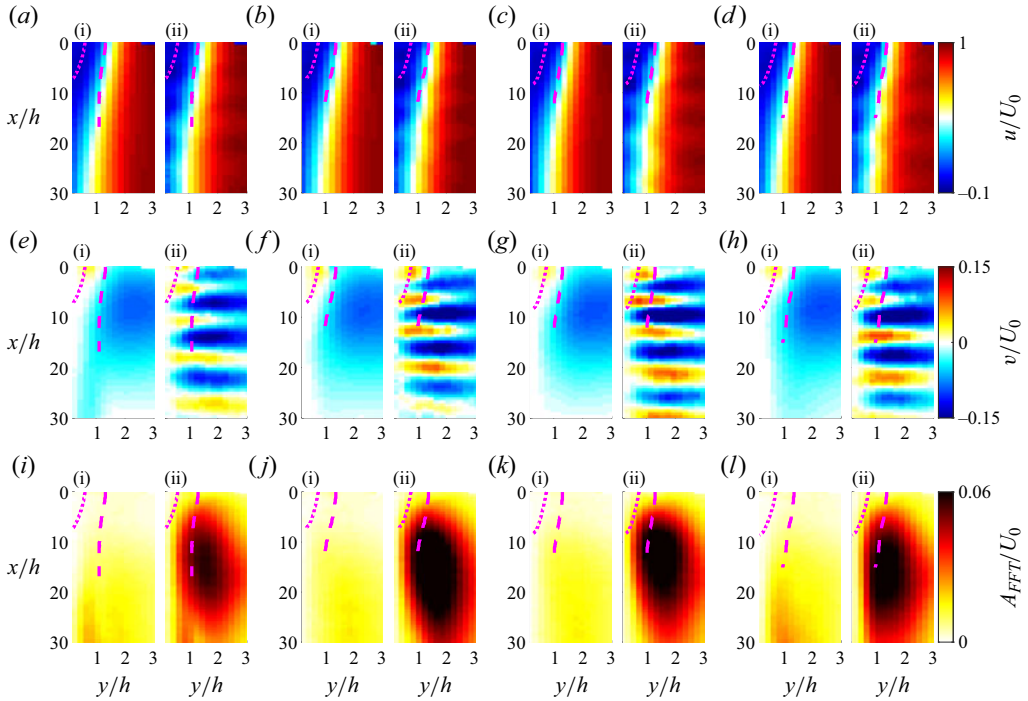


Figure 22. Same as in figure 21 but for 10PPI porous insert configuration: at four different spanwise locations:  $z = -3.8$  h (panels *a,e,i*);  $z = -1.2$  h (panels *b,f,j*);  $z = 1.4$  h (panels *c,g,k*);  $z = 4.0$  h (panels *d,h,l*).

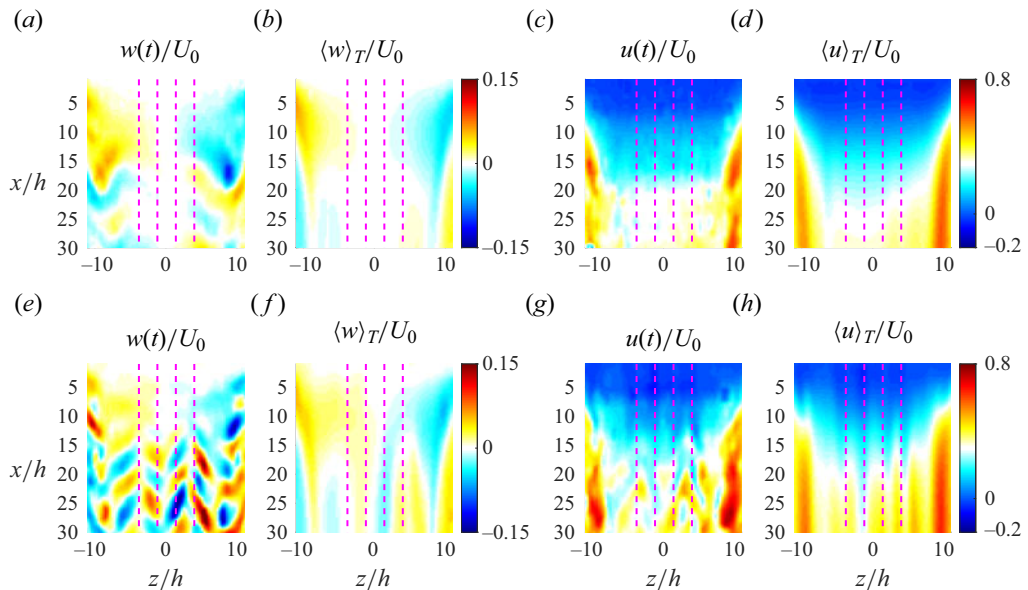


Figure 23. Spanwise and streamwise velocity components measured on the  $x$ - $z$  plane at  $y = 0.7h$  for  $Re_H = 400$ . Top and bottom rows represent solid and 10PPI configurations, respectively. Instantaneous and time-averaged velocity fields are presented in panels (*a,c,e,g*) and (*b,d,f,h*), respectively. Vertical magenta lines mark  $z/h \in \{-3.8, -1.2, 1.4, 4.0\}$  locations.

*Influence of porous material on the flow behind a BFS*

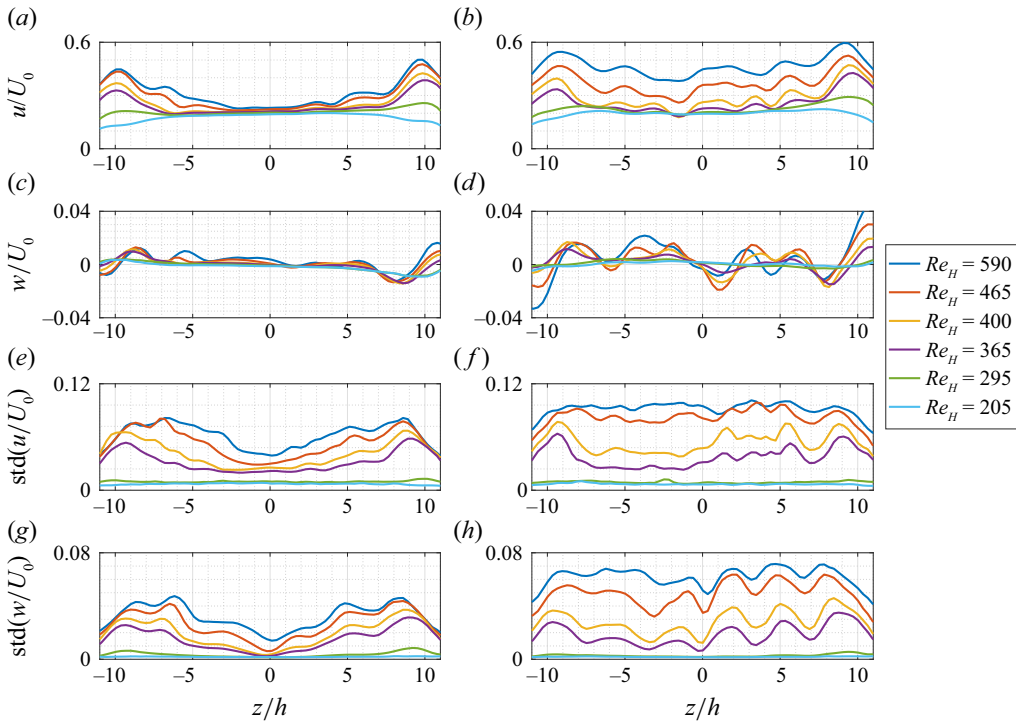


Figure 24. Time-averaged velocity components and velocity fluctuations as a function of spanwise location  $z$ . Presented profiles result from averaging the PIV measurements on the  $x$ - $z$  plane at  $y/h = 0.7$  over  $x/h \in (0, 30)$ . Right and left columns correspond to solid and 10 PPI porous inserts, respectively. Streamwise and spanwise velocity components, as well as streamwise and spanwise velocity fluctuations, are presented from top to bottom.

Giannopoulos (2021) who proposed  $Re_H = 670$  as the lower bound of the threshold for streak instability.

For 10 PPI configuration we observe a clear spanwise-periodic structuring of spanwise velocity component with  $\lambda_z \approx 4h$  (central region of figure 23e). The spanwise modulation is absent in the vicinity of the separation edge and its amplitude starts growing from  $x/h \gtrsim 15$ . However, in figure 22(e–h) we distinguish the signature of a two-dimensional roller structure forming directly downstream of the separation edge. This picture of three-dimensionality that develops further downstream is similar to mode A instability developing on top of the Bénard–von Kármán street behind the cylinder wake (Henderson & Barkley 1996; Williamson 1996) or to three-dimensional von Kármán instability observed in low-Reynolds-number flow around an airfoil (Nastro *et al.* 2023). We note that we did not observe such a spanwise modulation in the central region of the test section for solid impermeable configuration.

Next, we averaged over the streamwise direction the time-averaged and fluctuating part of streamwise and spanwise velocity components measured in the top view. The resulting profiles and their dependence on  $z$  are presented in figure 24, with  $Re_H$  values specified in the legend. Solid and 10 PPI porous configurations are presented in left and right columns, respectively. Time-averaged profiles of streamwise and spanwise velocity components are presented in figure 24(a–d). Corresponding profiles of temporal fluctuations are shown in figure 24(e–h).

For the lowest Reynolds numbers ( $Re_H = 205$  and  $Re_H = 295$ ) spanwise profiles for all four considered quantities reach comparable intensity levels for both solid and 10 PPI porous configurations. Starting from  $Re_H = 365$  the intensity of velocity fluctuations is typically higher for 10 PPI when compared with solid reference case. Furthermore, the periodic variability along the spanwise direction is more pronounced for 10 PPI. Moreover, for solid configuration, the intensity levels of these quantities typically peak in the vicinity of the side walls and then gradually decrease in damped-oscillation fashion toward the minimum at the centre of the test section. In contrast, for a 10 PPI insert, spanwise oscillation occurs around a constant value that does not change significantly along the central part of the test section ( $-5 < z/h < 5$ ).

We note that no spanwise modulation of time-averaged streamwise velocity component has been measured for the solid reference case at  $Re_H = 295$ . In contrast, for 10 PPI porous insert at the same Reynolds number we did observe very weak spanwise modulation of time-averaged streamwise velocity component with the amplitude of oscillations below 0.7 % of  $U_0$ . This amplitude increases up to approximately 2.3 % of  $U_0$  for  $Re_H = 400$  and 10 PPI, as can be seen in [figure 24\(b\)](#).

## 7. Characterisation of the boundary layer upstream of the separation edge

In this section, we characterise the incoming boundary layer upstream of the separation edge. All PIV parameters are the same as in the main measuring campaign described in § 2–§ 4, with the only exception of using a smaller interrogation window ( $32 \times 11$  pix with 75 % overlap) to enhance the spatial resolution into  $x/h = 0.20$  and  $y/h = 0.06$ .

In [figure 25](#) we show velocity fluctuations of both measured velocity components at the separation edge ( $x = 0$ ) averaged along the wall-normal direction to estimate environmental noise in the experimental facility. Velocity fluctuations are computed using standard deviation and resulting values are lower than 2 % for all realisations and for all insert configurations. Fluctuations remain approximately constant for the entire range of Reynolds numbers under consideration, with a single exception for the wall-normal velocity component for 10 PPI configuration (blue circles in [figure 25a](#)). For this specific case, the intensity of the fluctuations is constant up to  $Re_H \leq 400$  and starts to grow gradually with the Reynolds number for  $Re_H > 400$ . The noise level of the wall-normal velocity component, as well as its dependence on the Reynolds number, are the same for both solid and 45 PPI inserts.

Next, displacement ( $\delta_0$ ) and momentum ( $\theta_0$ ) thickness at the separation edge ( $x = 0$ ) are calculated using trapezoidal integration of streamwise velocity profile  $u(y)$ , with their dependence on Reynolds number presented in [figure 26](#). The green error bar is a sum of errors associated with the determination of the free-stream velocity, detection of the position of the lower bounding wall and half of the value of trapezoidal integration between the first valid measurement point closest to the wall and linearly interpolated location, at which streamwise velocity reaches zero. The difference between solid and 45 PPI configurations in [figure 26](#) is barely perceptible. For 10 and 20 PPI, both  $\delta_0$  and  $\theta_0$  are slightly smaller when compared with the solid reference case.

Time-averaged streamwise velocity profiles in the lower boundary layer upstream of the separation edge are characterised in [figure 27](#) for  $x/h = 0.0, -2.5, -5.0$ , from left to right. Plotted velocity profiles are selected such that  $Re_H < 600$  for 10 PPI,  $Re_H < 700$  for 20 PPI,  $Re_H < 790$  for 45 PPI and  $Re_H < 900$  for a solid insert. They mutually overlap and compare well with zero-streamwise-pressure-gradient equilibrated Blasius boundary

Influence of porous material on the flow behind a BFS

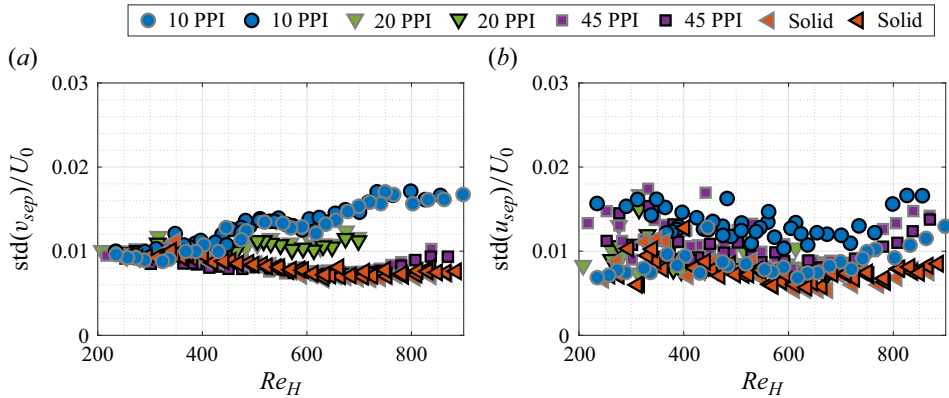


Figure 25. Velocity fluctuations of wall-normal (a) and streamwise (b) velocity component at the separation edge ( $x = 0$ ) as a function of  $Re_H$ .

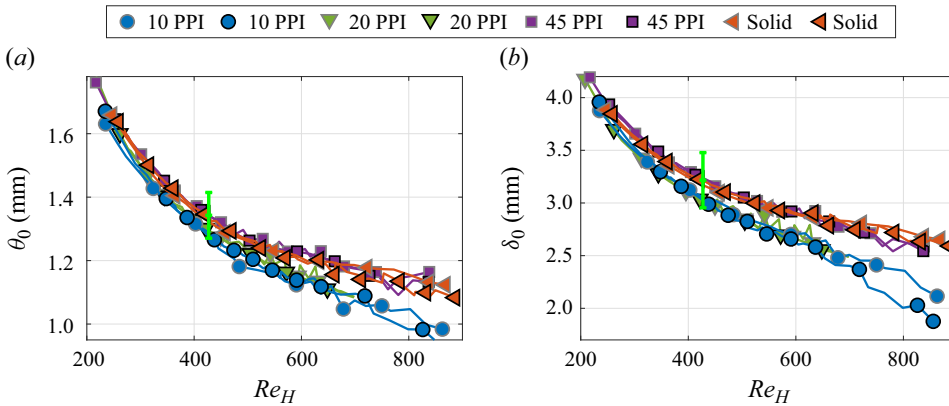


Figure 26. Momentum (a) and displacement (b) thickness of inlet lower boundary layer profiles at the separation edge ( $x = 0$ ).

layer (cyan dashed curve) for all insert configurations. The shape factor of the presented velocity profiles equals  $H = \delta(x)/\theta(x) = 2.5 \pm 0.2$ .

Finally, in [figure 28](#) we present the downstream dependence of the velocity fluctuations within the incoming lower boundary layer for  $Re_H \in (290, 410, 510)$  and for all insert configurations. Specifically, we show streamwise (top row) and wall-normal (bottom row) velocity fluctuations that are averaged along the wall-normal direction within the range  $y_u \in (0.3 - 2.0)$ , where  $y_u = 0$  corresponds to the level of the inlet floor upstream of the separation edge. The intensity of streamwise velocity fluctuations remains constant up to the separation edge at  $x/h = 0$ . Higher intensity of wall-normal velocity fluctuations remains confined near the separation edge for  $x/h \gtrsim -2.5$ .

As already specified in § 2, the maximal relative permeability  $k_1/W^2 \leq 12.4 \times 10^{-6}$  in our experiments is an order of magnitude lower than the typically considered values (Gupte & Advani 1997; Breugem *et al.* 2006; Suga & Nishio 2009; Suga *et al.* 2010; Kuwata & Suga 2016) due to expansion ratio close to unity. As reported by Breugem *et al.* (2005), low relative permeability reduces slip velocity at the fluid–porous interface. In our case, the slip velocity can be estimated as  $U_s \approx 1.2\%U_0$ , with a value of the order of  $10^{-3}$  ( $\text{m s}^{-1}$ )

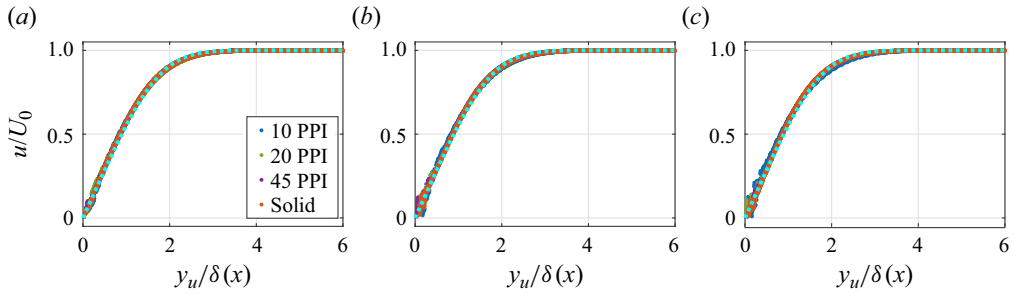


Figure 27. Time-averaged streamwise velocity profiles  $u(y_u)$  of the lower boundary layer formed above the inserts measured upstream of the separation at  $x/h = 0.0$ ,  $x/h = -2.5$  and  $x/h = -5.0$ , from left to right. The wall-normal coordinate  $y_u = y - h$  is normalised by local displacement thickness  $\delta(x)$ . Velocity profiles for all insert configurations and all Reynolds numbers are presented in each panel. Independently of the insert configuration, all measured profiles compare well with laminar equilibrated Blasius boundary layer with zero pressure gradient (marked as a cyan dashed curve).

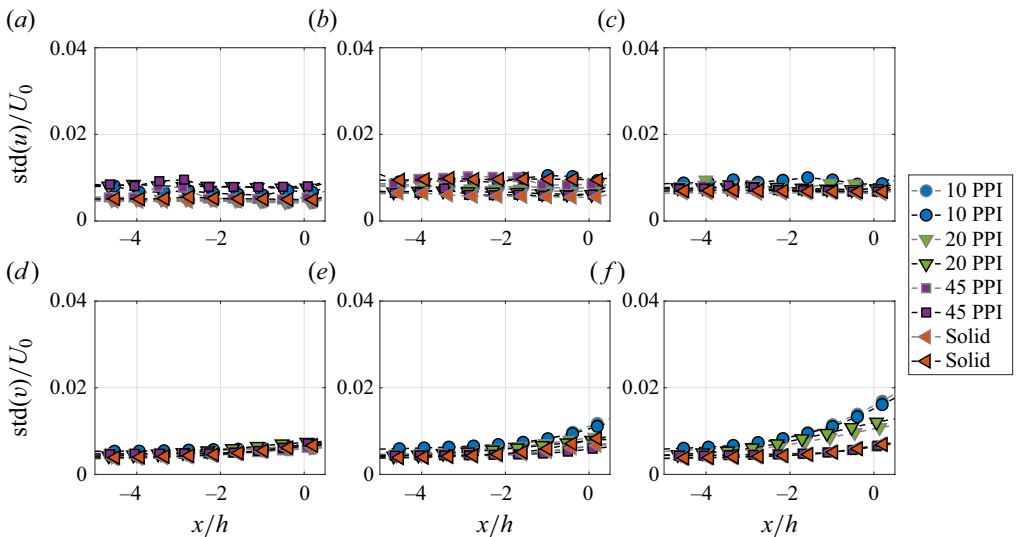


Figure 28. Streamwise ( $\text{std}(u)/U_0$ ) and wall-normal ( $\text{std}(v)/U_0$ ) velocity fluctuations in the incoming boundary layer upstream of the separation ( $x/h < 0$ ): (a,d)  $Re_H = 290$ , (b,e)  $Re_H = 410$  and (c,f)  $Re_H = 510$ . Velocity fluctuations are spatially averaged along the wall-normal direction for  $y_u/h \in (0.3 - 2.0)$ , where  $y_u/h = 0$  is the level of the inlet floor upstream of the separation edge ( $x < 0$ ).

(figure 27). The pore Reynolds number based on the slip velocity  $U_s$  and permeability microscale  $\sqrt{k_1}$  is an order of magnitude lower than unity ( $Re_{pore} = U_s \sqrt{k_1} / \nu = 0.2$  for 45 PPI and  $Re_{pore} = 0.3$  for 10 PPI). Furthermore, the permeability  $k_1$  is more than two orders of magnitude lower than the squared step height  $h^2$ , which is a macroscale in our geometrical configuration. Low pore Reynolds number and scale separation between permeability and squared macroscale allows us to use the Brinkman model to approximate the flow within the fluid–porous interface upstream of the separation edge, in agreement with the analysis of Breugem *et al.* (2005) for spatially evolving laminar boundary layer over a porous substrate.

This interface is defined as the region at the fluid–porous boundary, in which the time-averaged streamwise velocity profile relaxes from the slip velocity at the

top of the interface to Darcy's drift velocity at the bottom. Using volume-averaged Navier–Stokes equations Breugem *et al.* (2006) demonstrated that the time-averaged streamwise velocity penetrates within the fluid–porous interface and decays exponentially to zero with increasing penetration depth, in agreement with analytical predictions for the Brinkman boundary layer within a porous substrate (Breugem *et al.* 2005). This spatial exponential decay in a porous medium has a positive second derivative of the streamwise velocity profile ( $d^2u/dy^2 > 0$ ), whereas Blasius boundary layer shear flow above a porous insert is characterised by  $d^2u/dy^2 < 0$ . The continuity of the second derivative implies an inflectional point in a fluid–porous interface, the presence of which has been further verified using microscale-resolved direct simulations of the Navier–Stokes equation using the Lattice–Boltzmann method by Suga & Nishio (2009) and Kuwata & Suga (2016). Jiménez *et al.* (2001) observed that a porous wall induces large-scale spanwise rolls originating from Kelvin–Helmholtz-type instability. Breugem *et al.* (2006) observed similar spanwise-coherent vortical structures that were manifested by enhanced amplitude of cross-stream velocity fluctuations. Suga *et al.* (2010) experimentally confirmed a significant increase in wall-normal velocity fluctuations due to porous substrate permeability.

To summarise, figure 27 demonstrates that the incoming lower boundary layer is well approximated by an equilibrated Blasius boundary layer with no streamwise pressure gradient, independently of porous insert configurations. In addition, the low relative permeability of the porous inserts reduces the slip velocity at the fluid–porous interface. This allows us to approximate the flow within the interface by the Brinkman boundary layer (Breugem *et al.* 2005), which, in turn, justifies the presence of an inflectional point in time-averaged streamwise velocity profile within the fluid–porous interface (compare with, e.g. Breugem *et al.* 2006). In figure 28 we can observe that 10 PPI and 20 PPI porous inserts locally induce weak wall-normal velocity fluctuations in the vicinity of the separation edge ( $x/h \gtrsim -2.5$ ) that does not exceed 2% of  $U_0$ . This is in full agreement with numerical (Breugem *et al.* 2006) and experimental (Suga *et al.* 2010) results, according to which permeability of the porous substrate results in the enhancement of the wall-normal velocity fluctuations.

## 8. Influence of porous inserts on time-averaged velocity and pressure fields

As mentioned in the introduction, BFS dynamics can be estimated based on the linearisation around the time-averaged fields. In this section, we evaluate whether the porous inserts modify the time-averaged velocity and pressure gradient fields. We present the spatial distribution of time-averaged velocity fields in figure 29. Columns correspond to  $Re_H = 290$ ,  $Re_H = 410$  and  $Re_H = 510$ , from left to right. Each column is composed of two groups of panels illustrating the streamwise and wall-normal velocity components (figures 29a–i and 29j–r, respectively). Each panel group is composed of three rows representing solid, 45 PPI and 10 PPI porous inserts, from top to bottom. For all insert configurations, the incoming boundary layer separates from the top corner edge of the BFS inlet inducing a recirculation zone at the outlet, as marked by magenta dotted curves. In addition, dashed magenta curves mark the locus of inflectional points of time-averaged streamwise velocity profiles downstream of the separation edge. In figure 30 we present time-averaged streamwise velocity profiles  $u(y)$  measured downstream of the separation edge and within the recirculation zone. Three different streamwise locations are grouped in columns,  $x/h \in (1.7, 6.4, 11.1)$ , from left to right. Rows from top to bottom correspond to  $Re_H \in (290, 410, 510)$ . On each panel, we superpose the measured velocity profiles for

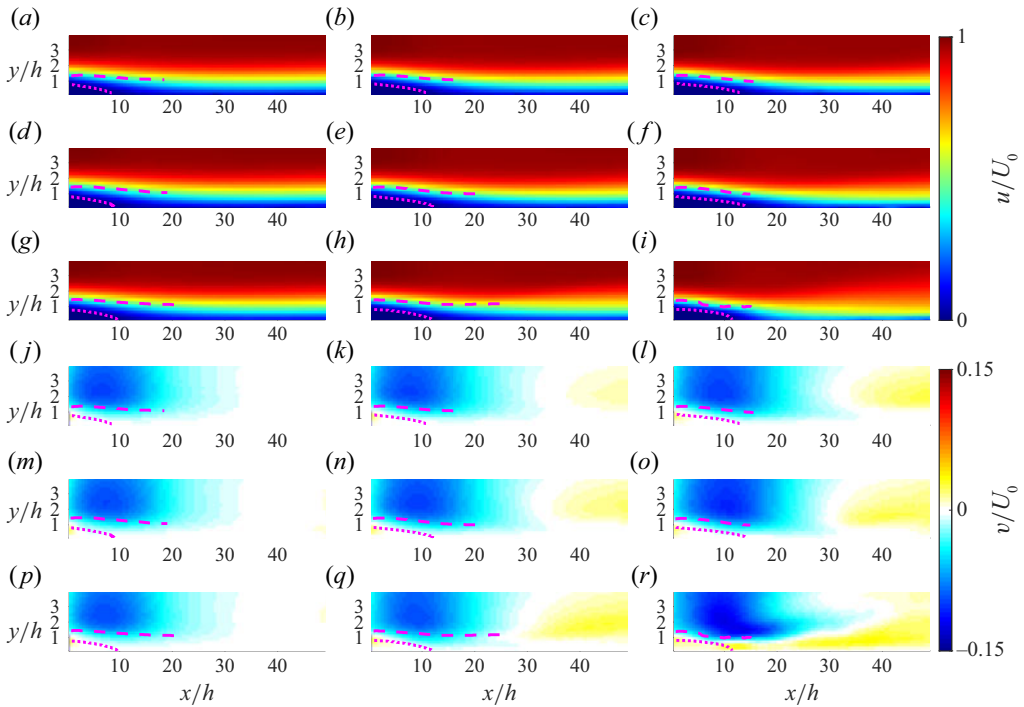


Figure 29. Spatial distribution of time-averaged streamwise (*a–i*) and wall-normal (*j–r*) velocity components for  $Re_H \in (290, 410, 510)$ , in columns from left to right. Velocity fields for three different configurations are presented: solid (*a,b,c,j,k,l*), 45 PPI (*d,e,f,m,n,o*) and 10 PPI (*g,h,i,p,q,r*). Compare with figures 4 and 5.

all realisations and all insert configurations. The time-averaged velocity profiles within the recirculation zone are not altered in any significant way by porous inserts. The lack of influence of porous inserts on time-averaged velocity fields is a result of an expansion ratio close to unity and low relative permeability.

In addition, Zielinska *et al.* (1997) and Mantić-Lugo *et al.* (2014) reported that the time-averaged flow can be considered as the base flow modified through nonlinear Reynolds stresses induced by the finite-size amplitude of the velocity fluctuations. The same spatial distribution of time-averaged velocity fields in the recirculation zone for all insert configurations demonstrates that the influence of the permeability is sufficiently weak to not alter the mean-flow modification of the solid insert reference case.

As shown in figures 16 and 17 the dominant frequency of mode 1 can be approximated by the most amplified frequencies of the Falkner–Skan family of boundary layer flows. These velocity profiles are parametrised using the Hartree parameter  $\beta$  associated with the time-averaged streamwise pressure gradient. To compare these theoretical values with our experimental results shown in figure 29, we calculate the streamwise and wall-normal pressure gradients from PIV measurements assuming that BFS flow is two-dimensional. For this, we transform Navier–Stokes equation into

$$\langle \partial p / \partial x \rangle_T = -\rho \langle \partial u / \partial t + u \partial u / \partial x + v \partial u / \partial y \rangle_T - \langle \mu \Delta(u) \rangle_T, \quad (8.1)$$

$$\langle \partial p / \partial y \rangle_T = -\rho \langle \partial v / \partial t + u \partial v / \partial x + v \partial v / \partial y \rangle_T - \langle \mu \Delta(v) \rangle_T, \quad (8.2)$$

where  $\rho$  and  $\mu$  refer to the density and dynamic viscosity of water.

## Influence of porous material on the flow behind a BFS

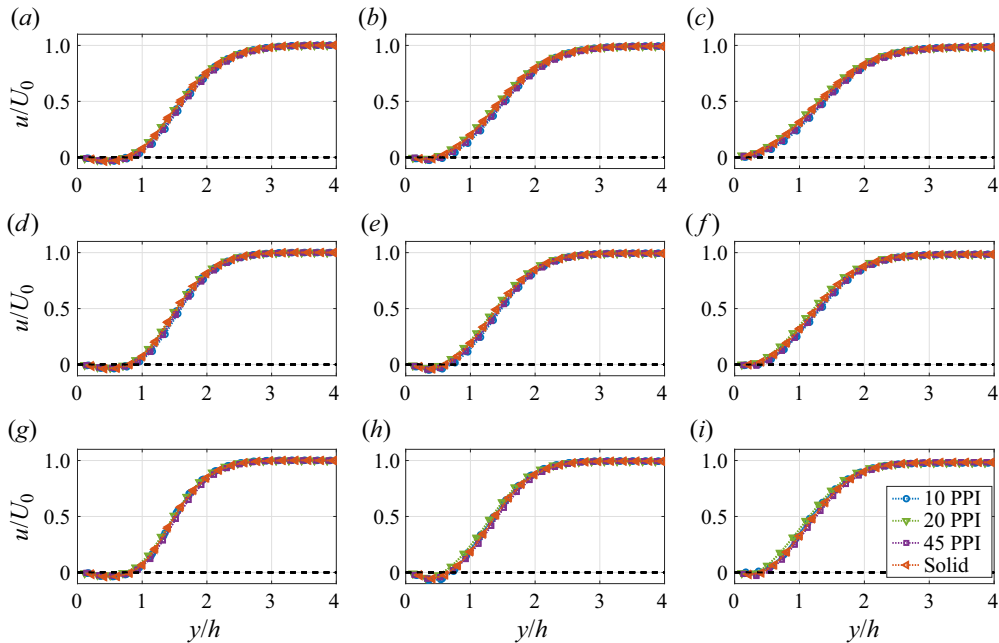


Figure 30. Time-averaged streamwise velocity profiles measured at different streamwise locations downstream of the separation edge ( $x/h > 0$ ). Wall-normal location is normalised with step height  $h$ . Eight different series (two series for each of four insert configurations) are shown on each panel: columns correspond to  $x/h = 1.7, 6.4, 11.1$ , from left to right; rows represent  $Re_H = 290, 410, 510$ , from top to bottom.

In figure 31 we present the spatial distribution of time-averaged pressure gradients along the streamwise ( $\langle \partial p / \partial x \rangle_T$ ) and wall-normal ( $\langle \partial p / \partial y \rangle_T$ ) directions. The global maximum intensity of the streamwise pressure gradient is more than twice as large when compared with the pressure gradient along the wall-normal direction. Local influence of the porous insert on the pressure gradients can be observed only downstream of the recirculation zone and only for the largest values of permeability (10 PPI) and Reynolds number ( $Re_H = 510$ ).

In figure 32 we present a dependence of global spatial maximum of  $\langle \partial p / \partial x \rangle_T$  on Reynolds number. For sufficiently low  $Re_H$  the global spatial maximum of  $\langle \partial p / \partial x \rangle_T$  remains constant and does not depend either on  $Re_H$  or the insert configuration. In addition, all critical thresholds of Hopf bifurcation marked in figure 10 fall within the Reynolds number range, for which streamwise pressure gradient is constant ( $\langle \partial p / \partial x \rangle_T = 0.04 \pm 0.01$ ). This indicates that Hopf bifurcation induced by porous inserts is not influenced by the streamwise pressure gradient. We also observe that  $\langle \partial p / \partial x \rangle_T$  starts to increase at Reynolds number close to the value, at which nonlinear saturation of dominant mode 2 occurs.

Constant value of  $\langle \partial p / \partial x \rangle_T = 0.04(\pm 0.01)$  is marked by a red dashed horizontal line and corresponds to Falkner–Skan solution for  $\beta = -0.045(\pm 0.007)$ . This implies that the intensity of adverse pressure gradient in BFS geometry at the reattachment is lower than the prediction of the Falkner–Skan solution for  $\beta = -0.198$ . However, Tollmien–Schlichting instability is shear-driven with characteristics that depend on the shape of the velocity profile. Moreover, the Falkner–Skan flow family represents self-similar velocity profiles and  $\beta$  defines the required intensity of local streamwise pressure gradient to maintain self-similarity along the downstream direction. If the local adverse streamwise pressure gradient is lower than the required value, then the streamwise

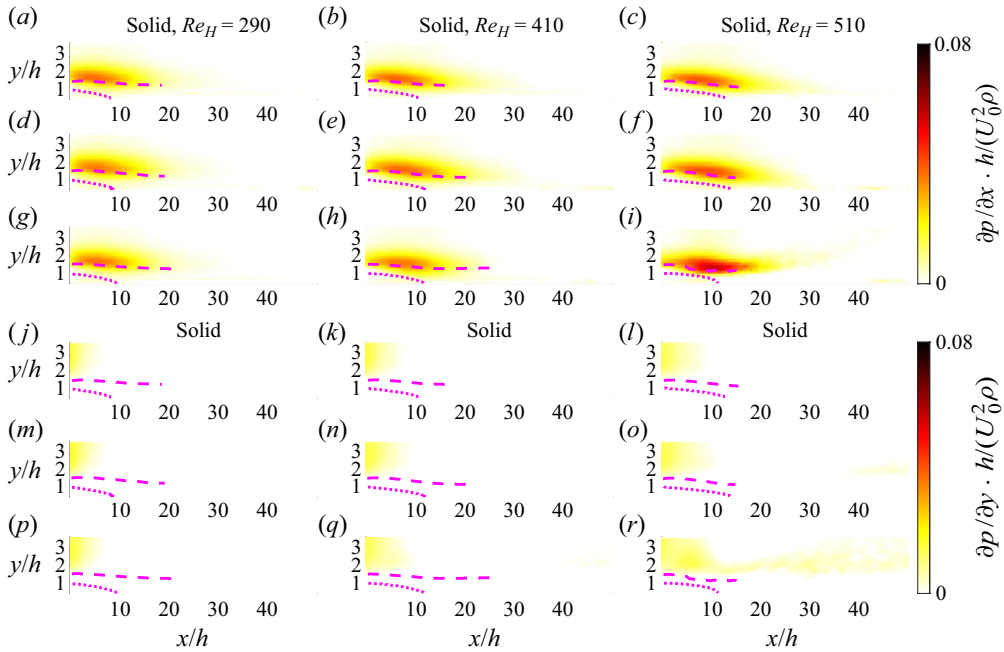


Figure 31. Same as in figure 29 but for time-averaged pressure gradient along streamwise (*a–i*) and wall-normal (*j–r*) directions. Pressure gradients are normalised with double the free-stream dynamic pressure ( $\rho U_0^2$ ) and step height ( $h$ ). Pressure gradients for three different configurations are presented: solid (*a,b,c,j,k,l*), 45 PPI (*d,e,f,m,n,o*) and 10 PPI (*g,h,i,p,q,r*).

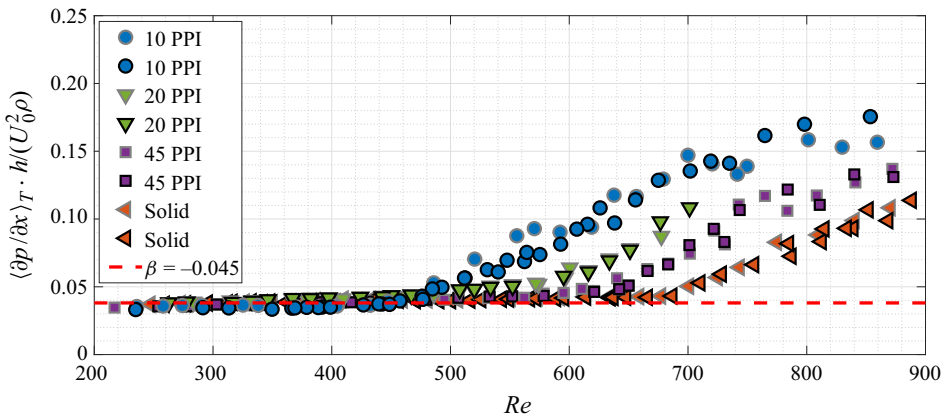


Figure 32. Global spatial maximum of time-averaged streamwise pressure gradient  $\langle \partial p / \partial x \rangle_T$  as a function of  $Re_H$  for all insert configurations. For sufficiently low Reynolds numbers, the time-averaged streamwise pressure gradient  $\langle \partial p / \partial x \rangle_T$  is independent of Reynolds number and porous configuration.

velocity profile will relax further downstream to the solution closer to the Blasius boundary layer. Such equilibration has been indeed reported for BFS flow by Bradshaw & Wong (1972) and Jovic & Driver (1994).

Finally, we present profiles of streamwise ( $\langle \partial p / \partial x \rangle_T$  in figure 33*a–c*) and wall-normal pressure gradients ( $\langle \partial p / \partial y \rangle_T$  in figure 33*d–f*) in the very vicinity of the separation edge ( $x/h = 0.7$ ) and for all porous inserts under investigation. Columns correspond to

## Influence of porous material on the flow behind a BFS

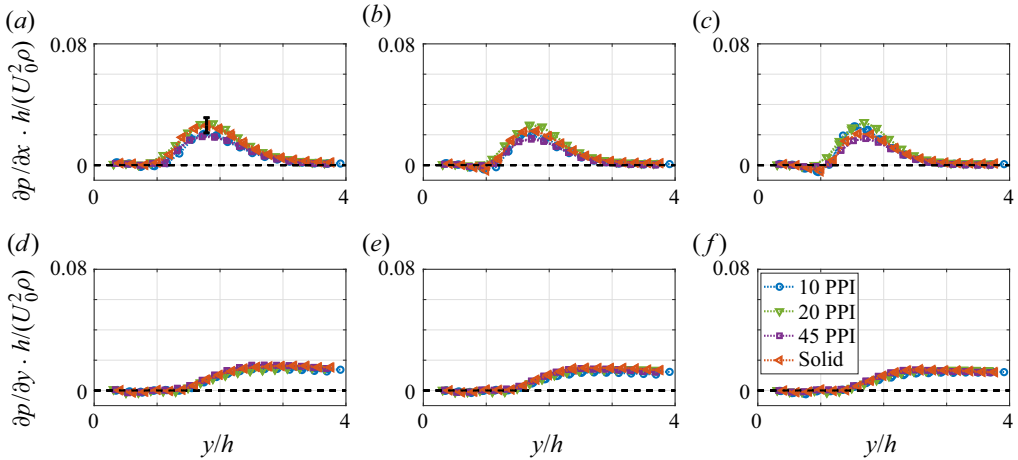


Figure 33. Pressure gradient profiles along the wall-normal direction  $y$  downstream of the separation edge at  $x = 0.7h$ , with  $Re_H = 290, 410, 510$  in (a,d), (b,e) and (c,f), from left to right. Panels (a–c) and (d–f) represent streamwise and wall-normal pressure gradients, respectively. Both realisations for each of four insert configurations are shown.

$Re_H \in (290, 410, 510)$ , from left to right. Similar spatial distribution of both pressure gradients for all insert configurations indicates that there is no significant communication between the back and top wall of the porous insert in the vicinity of the separation edge. Furthermore, the pressure gradient along the wall-normal direction is not reduced by the porous insert permeability due to the low expansion ratio and resulting low relative permeability of porous inserts in our study.

### 9. Discussion

We have presented detailed experimental investigation of separated shear flow formed behind the BFS. To ensure the largest possible aspect ratio ( $AR \approx 26$ ) and to reduce possible influence of side walls, we select a step with low height ( $h = 5.77$  mm). We investigate the effect of porous inserts located upstream of the separation edge and compare our results with solid insert configuration considered as a reference case.

The dynamics of BFS flow is characterised by two nearly commensurate frequencies that can be grouped onto two distinct branches. We determine characteristic spectral range for each branch and we reconstruct their spatial support using Hilbert transform. Specifically, BFS structures associated with the upper branch (i.e. with higher frequencies) attain their local maximal amplitude in the vicinity of the locus of inflectional points. Global maximum of these spatial envelopes is reached close to the end of recirculation zone, where the separated shear layer reattaches. Downstream of the reattachment these envelopes subsequently decay along the streamwise direction. In contrast, low-frequency structures associated with lower branch attain their maximal value further downstream of the reattachment, in the region where the shear flow transforms from mixing-layer-type to boundary-layer-type flow. Porous inserts affect the upper branch and corresponding high-frequency structures. Specifically, their maximal amplitude is increased up to five times for 10 PPI when compared with the reference case with solid insert configuration (see figure 10).

At low Reynolds numbers, the dynamics of BFS flow is dominated by the low-frequency branch (spectral mode 1). Once the Reynolds number is increased, frequency cross-over

occurs leading to the dynamics dominated by a higher-frequency branch (spectral mode 2). The value of the Reynolds number for the frequency cross-over occurrence decreases with increasing permeability of porous inserts. Similar existence of two modes has been already observed for planar free jet (Sato 1960; Deo, Mi & Nathan 2008), cavity flow (Bengana *et al.* 2019), free hot circular jet (Monkewitz *et al.* 1990), separation bubble (Rist & Maucher 2002), separated flow over a smooth bump (Marquillie & Ehrenstein 2003), BFS geometry (Heenan & Morrison 1998*a,b*; Dovgal & Sorokin 2004) and airfoil at non-zero angle of attack (Symon, Sipp & McKeon 2019). Even a linear system subjected to harmonic perturbation exhibits a double-peak response curve for a sufficiently low expansion ratio ( $ER = 1.4$ , see Boujo & Gallaire 2015), which indicates a potential for linear amplification of two different frequencies.

Canonical instability mechanisms are attributed to both branches based on a comparison of measured streamwise velocity profiles with local stability analysis. When the dominant frequency of the upper branch (i.e. spectral mode 2) is normalised with momentum thickness at the separation edge ( $\theta_0$ ), then the upper branch frequencies compare well with results reported for the free mixing layer (e.g. Michalke 1965; Freymuth 1966; Ho & Huerre 1984) and BFS (e.g. Eaton & Johnston 1982; Chun & Sung 1996; Dovgal & Sorokin 2004). Generation of vortical structures in these flows is a result of Kelvin–Helmholtz instability. This is fully supported by figure 17(*a*), on which all measured velocity profiles immediately downstream of the separation edge can be collapsed to a single curve that is similar to a hyperbolic tangent representing a free-mixing layer. The maximal measured value of  $St_\theta$  on the upper branch in our experiment compares well with the most unstable frequency retrieved from the local stability analysis of the free mixing layer (e.g. Michalke 1965; Freymuth 1966). Once Reynolds number  $Re_H$  is increased further,  $St_\theta$  decreases in analogy with the trend reported by Michalke & Hermann (1982) for the free jet. Therefore, upper-branch vortices result from Kelvin–Helmholtz instability.

Using streamwise autocorrelation of the streamwise velocity fluctuations, Breugem *et al.* (2006) observed  $\lambda_{KH}/W = 2.5$  as a characteristic streamwise wavelength of Kelvin–Helmholtz instability ( $W$  refers to the height of the channel above the porous substrate). Kuwata & Suga (2016) reported  $\lambda_{KH}^+ \approx 700$  (equivalently  $\lambda_{KH}/W \approx 3.2$ ) as a characteristic wavelength of the most energetic proper orthogonal decomposition (POD) mode of spanwise-coherent pressure fluctuations induced by wall permeability. Finally, Chu *et al.* (2021) observed a weak signature of large-scale coherence in premultiplied spectra of streamwise turbulent kinetic energy with  $\lambda_x \geq 2W$  and without directly attributing these modes to Kelvin–Helmholtz instability. All these wavelengths can be transformed into characteristic frequencies by taking half of the free-stream velocity as their approximate phase velocity, which is a typical value for the most-amplified Kelvin–Helmholtz-type instability in a free-mixing shear layer. The resulting normalised frequencies are  $St_\theta \approx 0.019$  for Breugem *et al.* (2006),  $St_\theta \approx 0.013$  for Kuwata & Suga (2016) and  $St_\theta \leq 0.019$  for Chu *et al.* (2021). These values reported for higher Reynolds numbers are similar to the prediction for Kelvin–Helmholtz instability of mixing shear layer (Michalke 1965; Freymuth 1966), as well as with our upper branch frequencies.

Our measurements fully agree with these results: first, porous inserts enhance the amplitude of upper-branch BFS structures associated with Kelvin–Helmholtz instability and promote frequency cross-over. We also measured a higher intensity of wall-normal velocity fluctuations immediately upstream of the separation edge that increases with the permeability of the porous insert, as presented in the bottom row of figure 28(*d–f*). Finally, our characteristic frequencies of upper branch (figure 16*a*) compare well with results for

the turbulent shear flow above porous substrate, as well as with theoretical predictions for Kelvin–Helmholtz instability of inflectional mixing shear layer.

Breugem *et al.* (2006) reported that the structure and dynamics of turbulence in the shear flow above the porous substrate is altered for sufficiently high permeability of porous media. They used two different Reynolds numbers to distinguish between the effect of permeability ( $Re_K$ ) and roughness ( $Re_R$ ). Permeability Reynolds number is defined as the ratio between the effective pore diameter and viscous length scale ( $Re_K = U_\tau \sqrt{k_1}/\nu$ ) and the roughness Reynolds number is defined on the typical height of the roughness elements, which in our case is half of the averaged linear size of foam cell ( $Re_R = 0.5 \cdot d_{PPI} U_\tau/\nu$ ). Roughness can be neglected for  $Re_R < 5$ . Regarding the permeability effect, for  $Re_K = 0.31$  they observed that the porous medium is effectively impermeable for the flow. For  $Re_K = 1.06$  permeability influences the shear flow above the porous substrate through the fluid–porous interface, where the time-averaged streamwise velocity profile becomes inflectional. However, the bulk permeability is still too low to allow for any significant Darcy’s drift flow within the homogeneous porous medium below the interface. Non-negligible Darcy’s drift flow across the bulk of the porous medium has been observed for  $Re_K = 9.35$ . Based on measured values of permeability  $k_1$  and momentum thickness  $\theta_0$ , as well as using the known relation of slip velocity for the Blasius boundary layer, we determined that in our experiment  $Re_K \in (0.7, 1.1)$  and  $Re_R < 4$  at the threshold of Hopf bifurcation observed in figure 10. This demonstrates that Hopf bifurcation is induced by the effect of permeability at the fluid–porous interface of the insert.

The low expansion ratio and resulting low relative permeability reduce the estimated Darcy’s drift velocity through the back wall to zero as presented in figure 29(a–i) and in the left column of figure 30. This indicates that both the BFS back-wall and the bulk of the porous insert are effectively impermeable. As a result, the hydrodynamical influence of the porous inserts is limited to a fluid–porous interface. Our experimental configuration can be considered as an analogy to simplified stability analysis of the shear flows above the porous substrate, in which the effect of the porous medium is modelled as the boundary condition at the interface. The total streamwise extent of porous insert normalised with permeability microscale varies between approximately  $L_p/\sqrt{k_1} \approx 230$  for 45 PPI and  $L_p/\sqrt{k_1} \approx 150$  for 10 PPI, which further justifies the analogy with stability analysis.

Heenan & Morrison (1998a,b) investigated the effect of permeable boundary conditions on BFS flow in slightly different geometrical configuration. They created the plenum chamber below the level of the outlet lower bounding wall ( $y < 0$ ) and downstream of the separation edge ( $x > 0$ ), which they then covered with a perforated plate at  $y = 0$  level and with a varying total area of holes. For impermeable solid wall configuration (i.e. no holes), they observed two different frequencies, with the higher frequency being attributed to large vortices generated within the separated shear layer and the lower frequency associated with flapping, i.e. global dynamics of recirculation bubble. No details regarding the momentum or displacement thickness were provided, therefore it is not possible to compare their frequencies with the two branches found in our study. They observed that the amplitude of lower-frequency oscillations decreased when the total area of holes was increased. For a sufficiently long plenum chamber spanning up to the reattachment region, they even observed a complete suppression of the lower-frequency oscillations. They explained that this stabilisation was due to shifting the reverse flow from the recirculation zone to the plenum chamber below, which inhibited the upstream propagation of the perturbations generated at the reattachment.

Bradshaw & Wong (1972) postulated that BFS flow can be divided into two subregions. Directly behind the step and below the separated shear layer, there is a reverse

flow/recirculation zone that results in time-averaged streamwise velocity profiles with inflectional point. Downstream the reattachment, shear flow changes the character to boundary-layer-type flow that eventually re-equilibrates to typical boundary layer profile. We observe that the spatial envelope of spectral mode 1 associated with a lower-frequency branch dominates in the region downstream of the reattachment. Therefore, we compare frequencies of the lower branch to local linear stability analysis of Tollmien–Schlichting instability for the Falkner–Skan family of velocity profiles (Obremski *et al.* 1969; Wazzan *et al.* 1986; Xu *et al.* 2019). First, we show that streamwise velocity profiles  $u(y)/U_0$  measured at the reattachment can be collapsed to a universal curve for all insert configurations, provided that wall-normal coordinate  $y$  is normalised with displacement thickness and  $Re_H$  is below the threshold of frequency cross-over. Then we demonstrate that streamwise velocity profiles measured at the reattachment ( $x_r$ ) and  $2h$  downstream ( $x'_r = x_r + 2h$ ) match the Falkner–Skan profiles for  $\beta = -0.198$  and  $\beta = -0.140$ , respectively. Finally, we show that the largest measured frequency of the lower branch compares well with the most amplified frequency of the Falkner–Skan velocity profile at the reattachment ( $\beta = -0.198$ ). This leads us to the conclusion that lower-branch BFS structures are associated with Tollmien–Schlichting instability.

Iñigo, Sipp & Schmid (2014) pointed out that it is not possible to discriminate between noise-driven amplification of convective instability and self-sustained oscillator behaviour based only on spectral analysis of the experimental results. To identify the proper physical mechanism lying behind BFS dynamics with different inserts, we first note that the level of environmental noise within the facility does not change significantly between different measuring campaigns (figure 25). Moreover, despite intrinsic scatter, both realisations for each insert configuration follow similar behaviour (figure 10). This demonstrates that the qualitative difference between solid and porous inserts is repeatable and results from the intrinsic influence of the porous material.

For all porous inserts (10 PPI, 20 PPI and 45 PPI), the oscillation amplitude of dominant BFS structures follows the Landau equation, in analogy with other oscillator-like flow such as cylinder wake (e.g. Provansal, Mathis & Boyer 1987; Mantič-Lugo *et al.* 2014), three-dimensional bluff bodies (e.g. Ormières & Provansal 1999; Gumowski *et al.* 2008; Bobinski, Goujon-Durand & Wesfreid 2014; Klotz *et al.* 2014), jet in a cross-flow (e.g. Ilak *et al.* 2012; Klotz *et al.* 2019; Chauvat *et al.* 2020) or hot free jet (e.g. Monkewitz *et al.* 1990). This demonstrates that the dominant dynamics of BFS flow with porous inserts can be described by a limit cycle originating from supercritical Hopf bifurcation. Furthermore, the critical Reynolds number retrieved from the Landau equation is lower (10 PPI, 20 PPI) or close to (45 PPI) the threshold of frequency cross-over. Oscillations for all porous inserts can thus be attributed to the upper branch associated with spectral mode 2.

In contrast, our data do not support a similar conclusion for solid insert configuration. Specifically, frequency cross-over occurs when the value of  $E$  is at a non-negligible level, implying that both upper and lower branches are involved in the dynamics of BFS with solid insert. Moreover, measured values of  $E$  do not grow linearly with  $Re_H$ . In the context of solid impermeable walls, Marquillie & Ehrenstein (2003) identified two independent global instabilities in the separation of the boundary layer at the rear of the two-dimensional bump using global stability analysis. These instabilities are characterised by two distinct incommensurable frequencies: that with a higher frequency has been localised within the recirculation zone as a result of Kelvin–Helmholtz instability. The dynamics of low-frequency instability are determined by the mutual interaction of a large number of marginally absolutely unstable Tollmien–Schlichting modes with spatial support around the reattachment point. Finally, they also reported that low-frequency

instability is the first to occur when the Reynolds number is increased. All these observations are in full agreement with our measurements for BFS geometry with solid walls.

Beneddine *et al.* (2016) reported that if convective instability is strong and coherent along sufficiently long streamwise extent, then energetic structures observed in the flow are described by the dominating response mode of the resolvent operator and that this resolvent operator has one dominant singular value. They also argued that the same condition of dominant singular value has to be satisfied if any spectral mode is marginal. Finally, they concluded that when dominant singular value condition is satisfied, then optimal resolvent response mode and spectral mode are proportional (i.e. with the same spatial structure). This provides a connection between amplifier and oscillator dynamics.

Using local analysis, Dovgal *et al.* (1994) demonstrated that for slowly diverging flows with solid boundary conditions, instability can be characterised by local linear analysis under the assumption of shear flow being homogeneous along the streamwise direction. Specifically, they reported that the streamwise amplification rate for a long separation bubble of  $\sim 50h$  is similar for  $Re_\theta = 300$  and infinite Reynolds number showing that for  $Re_\theta = 300$  flow dynamics already reached the inviscid regime. However, Betchov & Szewczyk (1963) and Villermaux (1998) demonstrated that even for the simplest case of mixing layer at  $Re_\theta = 20$ , viscous effects significantly reduce the streamwise amplification rate of the perturbation. Similarly, Ducimetière, Boujo & Gallaire (2022) recently reported that the global response of the BFS flow to external perturbation depends on the Reynolds number. Our experimental results cover the intermediate range of  $Re_\theta \in (80, 160)$ , and provide the link between a viscous regime depending on the Reynolds number and a regime dominated by inviscid instability. Our main control parameter is the Reynolds number that has been varied in the vicinity of bifurcation and covers approximately one decade both in absolute value range and normalised distance from the threshold. This is in contrast to classical analysis of BFS (e.g. Dovgal *et al.* 1994), where the Reynolds number was not systematically varied as a control parameter and bifurcation from laminar steady base flow to unsteady flow was not studied.

Recirculation bubbles with shorter streamwise extent ( $\simeq 25h$ ) were studied by Dovgal & Sorokin (2004). Their BFS flow configuration has comparable step height, momentum and displacement thickness of the boundary layer as in our experiment. However, they did not study the dependence of BFS dynamics on the Reynolds number. Specifically, they measured two flow realisations with Reynolds number  $Re_H \approx 1700$ , which is above the range of interest in our experiment. Similar to our case, they observed two distinct frequency peaks, with a higher frequency attributed to the shear layer in the vicinity of the separation edge and a lower frequency further downstream close to the reattachment. High-frequency peaks were attributed to Kelvin–Helmholtz instability in the separated shear layer. Interestingly, their characteristic frequency of Kelvin–Helmholtz shear layer was  $St_\theta = 0.012$ , which is in good agreement with our results in figure 16(a). No information regarding displacement thickness at the reattachment was provided, therefore we cannot compare these results with a lower branch of Tollmien–Schlichting waves. Furthermore, they also observed that the high-frequency oscillations of mode 2 are insensitive to the low-frequency oscillations of mode 1.

Gallaire, Marquillie & Ehrenstein (2007) numerically investigated the smooth bump geometry of Marquillie & Ehrenstein (2003) and Ehrenstein & Gallaire (2008) and reported about stationary streamwise vortices with spanwise wavelength of  $\lambda_z \approx 12.5h$  as the most unstable global mode. They also estimated that a positive growth rate of streamwise vortices can be observed for  $\lambda_z \gtrsim 5.5h$ . Passaggia *et al.* (2012) performed

experiments for similar geometry and found a sequence of three distinct regimes of the flow once Reynolds number is increased: (a) steady two-dimensional base flow; (b) steady three-dimensional base flow with streamwise vortices inducing spanwise modulation of the flow with  $\lambda_z \approx 12.5h$ ; (c) self-sustained shedding of quasi-two-dimensional vortices characterised by low-frequency oscillations resulting from Hopf bifurcation. Our measurements presented in figures 18 and 19 do not reveal any significant stationary streamwise vortices other than vortices induced by the corners at the side walls. However, on  $k_z$  spectra in figure 20(b) we do observe some weak signature of instantaneous streamwise vortices. These weak streamwise vortices can induce spanwise streak-like modulation of the flow through a lift-up mechanism (Schmid & Henningson 2001; Schmid 2007), which has been observed experimentally by Beaudoin *et al.* (2004) for BFS and by Passaglia *et al.* (2012) for smooth bump.

Lanzerstorfer & Kuhlmann (2012) studied the influence of expansion ratio  $ER$  on the critical threshold for stationary streamwise vortices and their characteristic spanwise wavelength in BFS geometry. The critical Reynolds number for these structures to appear increases from  $Re_m \approx 710$  for  $ER = 2$  to  $Re_m \approx 2460$  for  $ER = 1.3$ . The spanwise wavelength increases from  $\lambda_z \approx 7h$  for  $ER = 2$  to  $\lambda_z \approx 10h$  for both  $ER = 1.3$  and 1.4. This implies that for a constant value of Reynolds number intensity of streamwise vortices will decrease with decreasing  $ER$  up to a point, at which Reynolds number will be lower than the critical threshold. Our results fully support this scenario, since we do not observe any significant signs of stationary three-dimensionality apart from the vortices near the side walls in our cross-stream measurements.

Giannopoulos (2021) investigated solid impermeable BFS flow with  $ER = 1.15$  in several  $x$ - $z$  planes spanning over  $y/h \in (0.2, 1.6)$  with the main focus on the  $y = 0.6h$  plane. They observed streaks (i.e. spanwise modulation of the time-averaged streamwise velocity component) with a spanwise wavelength of  $2h$  for  $Re_H < 1500$  and proposed the range of  $Re_H \in (670, 1200)$  as the threshold for their formation. They attributed this spanwise modulation to streamwise vortices that resulted from centrifugal instability due to the local curvature of streamlines in the recirculation zone. Similar vortices were reported by Beaudoin *et al.* (2004) who observed mushroom-like counter-rotating longitudinal vortices using the laser-induced fluorescence (LIF) visualisation technique. Similarly, in our measurements for solid impermeable configuration, we did not observe any significant modulation of time-averaged streamwise velocity in the central region of the test section up to  $Re_H = 590$ . For 10 PPI porous configuration we observed spanwise modulation of the flow fields at  $y/h = 0.7$  that develops further downstream from the separation edge ( $x/h \gtrsim 15$ ). The observed wavelength  $\lambda_z \approx 4h$  is of a similar order of magnitude to the modulation reported by Giannopoulos (2021).

Linear stability analysis of BFS with solid walls and with parabolic velocity profile imposed in the inlet channel revealed no unstable eigenmode with characteristic frequency greater than zero (Barkley *et al.* 2002; Lanzerstorfer & Kuhlmann 2012). However, permeability at solid–fluid boundary can destabilise an otherwise (least-)stable global eigenmode (Tilton & Cortelezzi 2008; Rosti *et al.* 2015; Wedin *et al.* 2015). This, in turn, leads to finite-amplitude, equilibrated oscillations described by Landau equation. In addition, our experimental measurements of wall-normal velocity fluctuations (figure 28d–f) are in full agreement with results for fully turbulent flow, for which porous material at the bounding wall induced spanwise rollers due to Kelvin–Helmholtz instability (Jiménez *et al.* 2001; Breugem *et al.* 2006; Suga *et al.* 2018; Nishiyama *et al.* 2020) that significantly enhanced momentum and heat transfer (Motoki *et al.* 2022).

## 10. Conclusions

We have experimentally studied the influence of a porous insert located directly upstream of the separation edge in BFS flow. This is an example of a hydrodynamic system that is a combination of: (a) separated shear flow with a large potential for perturbation amplification; and (b) a porous medium known for efficient flow destabilisation. We have distinguished between two characteristic frequencies in the flow for the investigated range of Reynolds numbers and observed that the dominating flow response switches from lower to higher frequency once the control parameter (Reynolds number) is increased. Furthermore, the Reynolds number for this frequency cross-over occurrence monotonically decreases when the permeability of the porous insert increases. When dominating frequencies are normalised with step height ( $h$ ) and free-stream velocity ( $U_0$ ), then their values collapse onto one of two spectral ranges centred around two characteristic Strouhal numbers ( $St_H$ ) that remain constant when  $Re_H$  is changed. In addition, using the Hilbert transform on the corresponding characteristic spectral ranges, we have reconstructed spatial envelopes for each characteristic  $St_H$ . Higher dominant frequency reaches the maximum in the vicinity of the locus of inflectional points in time-averaged streamwise velocity profiles within the recirculation zone. Spatial support for lower dominant frequency is located downstream of the reattachment of the separated shear layer and slightly above step height. We have distinguished between two frequency branches using momentum thickness at the separation edge (higher-frequency branch) and displacement thickness in the vicinity of the reattachment line (lower-frequency branch) as alternative characteristic length scales. Comparing normalised frequencies at each branch with reported results allows us to attribute Kelvin–Helmholtz and Tollmien–Schlichting instabilities to upper and lower branches, respectively. Porous inserts significantly increase the amplitude of Kelvin–Helmholtz spectral mode enhancing more efficient mixing. Squared FFT amplitude of dominating frequency for Kelvin–Helmholtz spectral mode follows the prediction of the Landau model. This demonstrates that BFS structures associated with higher frequency originate from supercritical Hopf bifurcation and their oscillations are described by a limit cycle. Frequency cross-over occurs prior (10 PPI and 20 PPI) or in the vicinity (45 PPI) of critical Reynolds number derived from the Landau model, indicating the dominating role of Kelvin–Helmholtz structures for all porous inserts. Finally, our results indicate that porous inserts promote transition to oscillator-type dynamics.

**Acknowledgements.** We would like to thank M. Dzikowski, J. Szumbariski, P. Szymczak, A. Ladd, J. M. Chomaz and J. E. Wesfreid for fruitful discussions. We also thank J. Wiśniewski for technical assistance with permeability measurements and B. Zaęcki for help with electronics.

**Funding.** This research was funded by National Science Center (Poland) within the OPUS-21 project (2021/41/B/ST8/03142).

**Declaration of interests.** The authors report no conflict of interest.

### Author ORCIDs.

-  L. Klotz <https://orcid.org/0000-0003-1740-7635>;
-  K. Bukowski <https://orcid.org/0009-0000-5681-700X>;
-  K. Gumowski <https://orcid.org/0000-0002-1751-0926>.

**Author contributions.** L.K. performed hydrodynamical experiments, analysed the data, reached conclusions and wrote the paper. K.B. helped with flow visualisations and characterised the permeability and porosity of porous materials. K.G. built both experimental set-ups used to obtain experimental results reported in the paper.

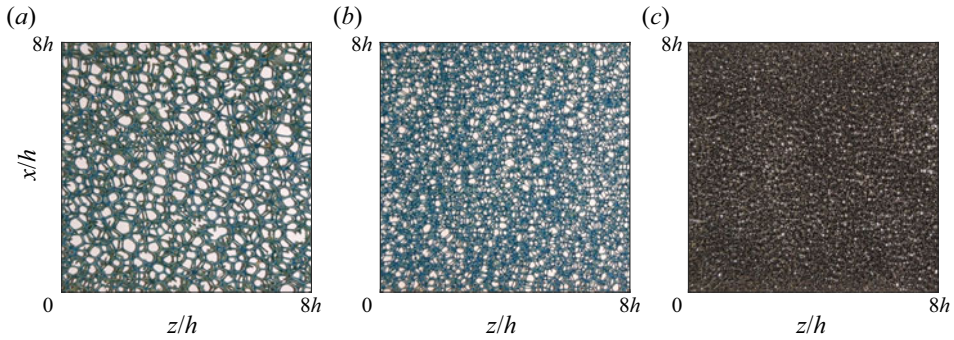


Figure 34. Top view of porous inserts made of open-cell rectified foam: (a) 10 PPI; (b) 20 PPI; (c) 45 PPI.

### Appendix A. Permeability, thickness of the fluid–porous interface and porosity of porous inserts

Here we determine permeability and porosity of the porous inserts made of open-cell rectified foams, the top views of which are presented in [figure 34](#). Permeability is inversely proportional to hydrodynamical resistance exerted on the working fluid once it passes through the porous medium. We use the Darcy–Forchheimer relation (see e.g. [Straatman et al. 2006](#); [Incera Garrido et al. 2008](#); [Suga et al. 2010](#); [Regulski et al. 2015](#)) to express the dependence of permeability on flow velocity and pressure drop across porous material:

$$\frac{\Delta p}{\Delta L} = \frac{\mu}{k_1} U_D + \frac{C_f \rho}{\sqrt{k_1}} U_D^2, \quad (\text{A1})$$

where  $\Delta p$  is the pressure drop across the medium,  $\Delta L$  is the length of the medium along the downstream direction,  $\rho$  and  $\mu$  are the density and dynamic viscosity of the working fluid,  $k_1$  and  $C_f$  are the permeability of the medium and Forchheimer coefficient and  $U_D$  is Darcy’s drift velocity.

Permeability of the rectified foam was characterised using an independent experimental set-up described in [Regulski et al. \(2015\)](#). The experimental facility described therein has been additionally modified by adding: (i) a 3-D-printed smooth contraction section to reduce the wall-normal dimension from 50 to 5.9 mm; (ii) Kobold NAD needle valve to control the volume flux; (iii) Kobold MIM flow meter with integrated thermocouple. We prepared three thin porous inserts ( $L_x \times L_y \times L_z = 50 \text{ mm} \times 5.9 \text{ mm} \times 44.7 \text{ mm}$ ) made of three different porous materials with 10, 20 and 45 pores per linear inch (PPI). This corresponds to a typical size of the pore of 2.54, 1.27 and 0.56 mm, respectively. Flow through a porous cube was induced by a pump and measured with a flow meter. Pressure drop along the downstream direction through a porous medium was measured using a differential pressure transducer. Dependence of measured pressure drop  $\Delta p$  along the streamwise extent of  $\Delta L$  on Darcy’s drift velocity  $U_D$  is presented in [figure 35](#). The data were additionally divided by dynamic viscosity  $\mu$  to compensate for any possible temperature variation. We determine linear and quadratic coefficients in the Darcy–Forchheimer relation by fitting a polynomial in the form of  $\Delta p/\Delta L/\mu = aU_D + b(U_D)^2$  to the measured data points. Red dashed curves in [figure 35](#) illustrate the best fit. The resulting values of permeability ( $k_1$ ) and Forchheimer coefficient ( $C_f$ ) of the porous medium are presented in the second and fifth columns in [table 1](#). Permeability  $k_1$  monotonically decreases with increasing PPI due to decreasing pore size and increasing hydraulic resistance.

*Influence of porous material on the flow behind a BFS*

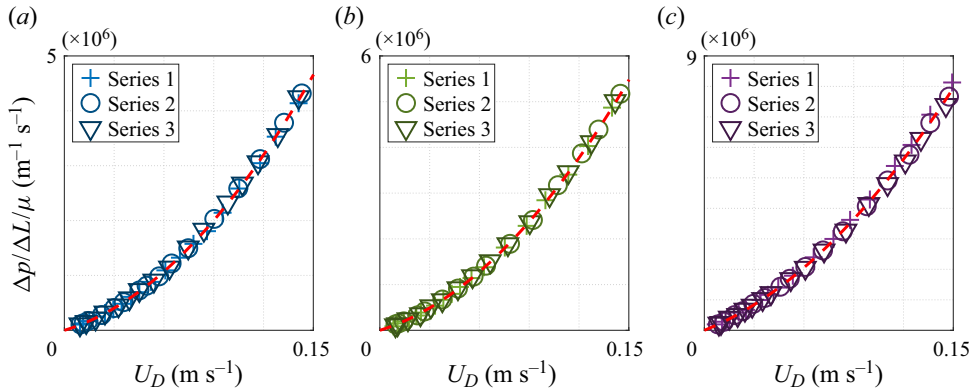


Figure 35. Pressure drop along the streamwise distance  $L$  divided by dynamic viscosity ( $\Delta p/\Delta L/\mu$ ) across the thin porous insert as a function of Darcy's drift velocity  $U_D$ . Three different porous materials were investigated: (a) 10 PPI, (b) 20 PPI and (c) 45 PPI. Red dashed curves illustrate the Darcy–Forchheimer relation used to determine permeability.

PPI	$k_1$ ( $m^2$ )	$\sqrt{k_1}$ (m)	$k_1/W^2$ (1)	$C_f$ (1)	$\epsilon$ (1)	$d_{PPI}^2/h^2$ (1)
10	$11.0 \times 10^{-8}$	$3.3 \times 10^{-4}$	$12.4 \times 10^{-6}$	0.05	$\simeq 98\%$	$\simeq 1.9 \times 10^{-1}$
20	$8.9 \times 10^{-8}$	$3.0 \times 10^{-4}$	$10.0 \times 10^{-6}$	0.05	$\simeq 98\%$	$\simeq 0.5 \times 10^{-1}$
45	$4.6 \times 10^{-8}$	$2.1 \times 10^{-4}$	$5.2 \times 10^{-6}$	0.04	$\simeq 98\%$	$\simeq 0.1 \times 10^{-1}$

Table 1. Values of permeability ( $k_1$ ), effective permeability pore size ( $\sqrt{k_1}$ ), relative permeability ( $k_1/W^2$ ), Forchheimer coefficient ( $C_f$ ) and porosity ( $\epsilon$ ) for 10 PPI, 20 PPI and 45 PPI porous rectified foams. The last column illustrates spatial scale separation between squared geometrical size of pore ( $d_{PPI}^2$ ) and the squared macroscale (step height  $h^2$ ), in agreement with Whitaker (1996).

Effective permeability pore diameter ( $\sqrt{k_1}$ ) is typically considered as the most relevant characteristic microscale in the bulk of porous medium (Beavers & Joseph 1967; James & Davis 2001; Breugem *et al.* 2005, 2006) and in the fluid-porous interface (Ochoa-Tapia & Whitaker 1995; James & Davis 2001). Specific values vary from 0.21 mm (45 PPI) to 0.33 mm (10 PPI) as presented in the third column of table 1. In addition,  $\sqrt{k_1}$  is significantly lower than the height of the channel above the porous insert ( $W$ ), which results in low relative permeability ( $k_1/W^2 \leq 12.4 \times 10^{-6}$ , see the fourth column in table 1) and reduces the slip velocity  $U_s$  at the interface (Breugem *et al.* 2005).

As specified in § 7 the magnitude of slip velocity  $U_s$  is of the order of  $10^{-3}$  ( $m s^{-1}$ ), the pore Reynolds number  $Re_{pore} = U_s \sqrt{k_1}/\nu$  is of the order of  $10^{-1}$  and  $k_1$  is more than two orders of magnitude lower than the squared step height. This allows us to use an estimation of the interface thickness of the Brinkman boundary layer within the porous medium for spatially evolving laminar boundary layer flow over a porous substrate proposed by Breugem *et al.* (2005). Based on their formulae, we estimate that the interface thickness of the fluid–porous interface varies between 1.0 mm (45 PPI) and 1.5 mm (10 PPI) and does not depend on the streamwise direction. The estimated thickness is approximately half of the size of geometrical pore for 10 PPI. Similar conclusions have been reported by Suga & Nishio (2009) and Kuwata & Suga (2016) who simulated hydrodynamics of the fluid–porous interface for an order of magnitude larger values of relative permeability than

in our case ( $\max(k_1)/W^2 = 8.9 \times 10^{-4}$  and  $\max(k_1)/W^2 = 1.7 \times 10^{-4}$ , respectively). They observed that the relaxation of the slip velocity at the interface to Darcy velocity in the bulk of porous medium occurs in less than one layer of geometrical cells. Furthermore, Kuwata & Suga (2016) also observed that boundary conditions imposed at the very bottom of the porous medium (the solid–porous interface) do not influence the hydrodynamics in the fluid–porous interface.

James & Davis (2001) investigated theoretically a Stokes flow passing through a sparse regular array of cylinders as a model for porous medium with high porosity. They reported that the bulk permeability of an array with 5 and 19 geometrical vertical layers is the same and that the interface region spans at most within one outermost layer. However, the ratio of the slip velocity at the interface to the free-stream centreline velocity of the shear flow above the porous insert decreases as the expansion ratio and relative permeability are decreased, in agreement with Breugem *et al.* (2005).

Suga & Nishio (2009) proposed two spatially homogeneous geometrical models to approximate the random distribution of geometrical pores: body-centred-cubic (BCC) and unit cube (UC). Our 45 PPI, 20 PPI and 10 PPI porous inserts allow for approximately 19/8/3 geometrical pores along the wall-normal direction for BCC organisation and 10/5/2 geometrical pores for UC organisation, respectively. We also assess spatial scale separation required for continuous porous medium approximation and for spatially averaged momentum equation to be applied. Whitaker (1996) reported that the continuous medium approach is justified when the squared macroscale ( $h^2$  in our case) is at least an order of magnitude larger than the squared characteristic length scale of a unit cell  $r_0^2$  (with  $r_0$  as the kernel for spatial averaging). Choosing geometrical pore size  $d_{PPI}$  as the length scale of a geometrical unit cell ( $r_0 = d_{PPI}$ ) allows us to satisfy this condition, as illustrated in the last column of table 1. This is further supported by the spatial distribution of velocity fields downstream the separation edge, which is the same for all insert configurations (see figures 29 and 30). This demonstrates that a 10 PPI porous insert with approximately three geometrical cells along the wall-normal direction behaves as a continuous porous medium in our specific geometrical configuration with low relative permeability.

Porosity  $\epsilon$  is another parameter describing porous material. It is defined by the volumetric fraction of the voids to the total volume of the porous medium. To estimate its value, we first determine the total volume of the porous cube ( $V_{total}$ ). Then, we calculate the volume of the solid material within a porous cube ( $V_{solid}$ ) using the mass and the density of the foam ( $\rho_{solid} = 1.13 \pm 0.13$  (g cm<sup>-3</sup>)). Finally, we compute the porosity as  $\epsilon = V_{void}/V_{total} = 1 - V_{solid}/V_{total}$ . The resulting values of  $\epsilon$  are presented in the sixth column in table 1. Porosity for each rectified foam is almost the same and close to unity. In this context, Rosti *et al.* (2015) demonstrated that an influence of porosity on dynamics at the fluid–porous interface is less significant when compared with the permeability.

## Appendix B. Spatial growth of the perturbation

To compare our results with local convective instability theory, we present the streamwise and wall-normal velocity fluctuations (figure 36a,b) for  $Re_H = 510$  and for all insert configurations. Global maximum of  $\text{std}(v)/U_0$  is typically larger and occurs closer to the separation edge when compared to the global maximum of  $\text{std}(u)/U_0$ . In addition, the initial spatial growth rate near the separation edge is greater for  $\text{std}(v)/U_0$  when compared with  $\text{std}(u)/U_0$ . This demonstrates that the wall-normal velocity component is more suitable to describe BFS structures formed within the recirculation zone, whereas streamwise velocity fluctuations can be used to describe the boundary layer downstream

*Influence of porous material on the flow behind a BFS*

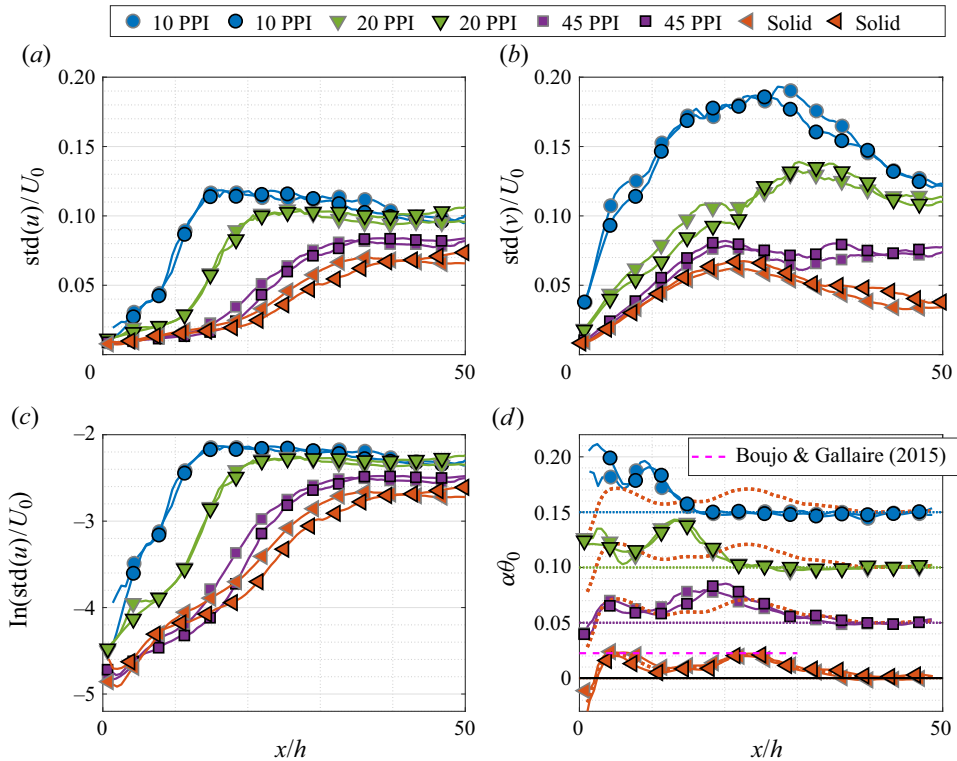


Figure 36. Streamwise (a) and wall-normal (b) velocity fluctuations as a function of the downstream distance from the separation edge for all insert configurations and  $Re_H = 510$ . In panel (c), logarithmic scale on vertical axis is used to present local exponential growth of  $\text{std}(u)/U_0$ . Resulting local spatial exponential amplification rate is presented in panel (d). For reference, global maximum of local spatial amplification along the streamwise direction obtained numerically by Boujo & Gallaire (2015) for  $ER = 2$  and for a solid insert is also superposed as horizontal dashed magenta line.

of the reattachment. Downstream dependence of  $\text{std}(u)/U_0$  is presented in both lin–lin (figure 36a) and log–lin (figure 36c) scales. For each streamwise location, we compute the local slope of  $\text{std}(u)/U_0$  on a log–lin plot, which provides us with the local streamwise spatial amplification rate  $\alpha$ . The resulting amplification rate is normalised with momentum thickness at the separation edge  $\theta_0$  and presented in figure 36(d). The results for each subsequent porous insert are shifted upwards by 0.05 to increase readability, with zero level for each insert configuration indicated by horizontal dashed lines in the corresponding colour. In addition, for each insert we superpose ensemble-averaged evolution of  $\alpha\theta_0$  for the solid reference case (orange dotted curves).

Interestingly, in contrast to the predictions of local convective instability theory, the streamwise amplification is not uniform along the streamwise direction. Specifically, we observe a local decrease in amplification rate  $\alpha\theta_0$  for each insert configuration. Similar non-monotonic dependence with local minimum has been already reported by Boujo & Gallaire (2015) for  $Re_H = 500$ ,  $ER = 2.0$  and solid impermeable boundary conditions. This illustrates the non-trivial dynamics of the flow due to the lack of homogeneity of the flow along the streamwise direction. In addition, our maximal local streamwise growth rate measured for solid insert compares well with the maximal value obtained numerically by Boujo & Gallaire (2015) marked by the magenta dashed horizontal line in figure 36(d).

Similar spatial amplification rate for two different expansion ratios ( $ER = 1.06$  in our case and  $ER = 2.0$  in Boujo & Gallaire 2015) indicates that  $ER$  does not significantly affect local convective growth of the combined frequency spectrum of streamwise velocity fluctuations in the free shear mixing layer once the incoming boundary layer separates. Finally, in figures 29 and 30 we presented that porous inserts do not alter in any significant way time-averaged velocity profiles within the recirculation zone. Despite similar velocity profiles, we observe an enhancement of streamwise amplification from  $\alpha\theta_0 \simeq 0.02$  (solid reference case, orange triangles in figure 36d) up to  $\alpha\theta_0 \simeq 0.05$  (for 10 PPI, blue circles in figure 36d).

#### REFERENCES

- ALIZARD, F., CHERUBINI, S. & ROBINET, J.-C. 2009 Sensitivity and optimal forcing response in separated boundary layer flows. *Phys. Fluids* **21** (6), 064108.
- ARMALY, B.F., DURST, F., PEREIRA, J.C.F. & SCHÖNUNG, B. 1983 Experimental and theoretical investigation of backward-facing step flow. *J. Fluid Mech.* **127**, 473–496.
- AVANCI, M.P., RODRÍGUEZ, D. & ALVES, L.S.D.B. 2019 A geometrical criterion for absolute instability in separated boundary layers. *Phys. Fluids* **31** (1), 014103.
- BARKLEY, D. 2006 Linear analysis of the cylinder wake mean flow. *Europhys. Lett.* **75** (5), 750.
- BARKLEY, D., GOMES, M.G.M. & HENDERSON, R.D. 2002 Three-dimensional instability in flow over a backward-facing step. *J. Fluid Mech.* **473**, 167–190.
- BEAUDOIN, J.-F., CADOT, O., AIDER, J.-L. & WESFREID, J.E. 2004 Three-dimensional stationary flow over a backward-facing step. *Eur. J. Mech. (B/Fluids)* **23** (1), 147–155.
- BEAVERS, G.S. & JOSEPH, D.D. 1967 Boundary conditions at a naturally permeable wall. *J. Fluid Mech.* **30** (1), 197–207.
- BENEDDINE, S., SIPP, D., ARNAULT, A., DANDOIS, J. & LESSHAFFT, L. 2016 Conditions for validity of mean flow stability analysis. *J. Fluid Mech.* **798**, 485–504.
- BENGANA, Y., LOISEAU, J.-C., ROBINET, J.-C. & TUCKERMAN, L.S. 2019 Bifurcation analysis and frequency prediction in shear-driven cavity flow. *J. Fluid Mech.* **875**, 725–757.
- BETCHOV, R. & SZEWCZYK, A. 1963 Stability of a shear layer between parallel streams. *Phys. Fluids* **6** (10), 1391–1396.
- BLACKBURN, H.M., BARKLEY, D. & SHERWIN, S.J. 2008 Convective instability and transient growth in flow over a backward-facing step. *J. Fluid Mech.* **603**, 271–304.
- BOBINSKI, T., GOUJON-DURAND, S. & WESFREID, J.E. 2014 Instabilities in the wake of a circular disk. *Phys. Rev. E* **89** (5), 053021.
- BOUJO, E. & GALLAIRE, F. 2015 Sensitivity and open-loop control of stochastic response in a noise amplifier flow: the backward-facing step. *J. Fluid Mech.* **762**, 361–392.
- BRADSHAW, P. & WONG, F.Y.F. 1972 The reattachment and relaxation of a turbulent shear layer. *J. Fluid Mech.* **52** (1), 113–135.
- BREUGEM, W.P., BOERSMA, B.J. & UITTENBOGAARD, R.E. 2005 The laminar boundary layer over a permeable wall. *Transp. Porous Media* **59** (3), 267–300.
- BREUGEM, W.P., BOERSMA, B.J. & UITTENBOGAARD, R.E. 2006 The influence of wall permeability on turbulent channel flow. *J. Fluid Mech.* **562**, 35–72.
- CANTWELL, C.D. & BARKLEY, D. 2010 Computational study of subcritical response in flow past a circular cylinder. *Phys. Rev. E* **82** (2), 026315.
- CHAUVAT, G., PEPLINSKI, A., HENNINGSON, D.S. & HANIFI, A. 2020 Global linear analysis of a jet in cross-flow at low velocity ratios. *J. Fluid Mech.* **889**, A12.
- CHEN, L., ASAI, K., NONOMURA, T., XI, G. & LIU, T. 2018 A review of backward-facing step (BFS) flow mechanisms, heat transfer and control. *Therm. Sci. Engng Prog.* **6**, 194–216.
- CHOI, H., JEON, W.-P. & KIM, J. 2008 Control of flow over a bluff body. *Annu. Rev. Fluid Mech.* **40** (1), 113–139.
- CHOMAZ, J.-M. 2005 Global instabilities in spatially developing flows: non-normality and nonlinearity. *Annu. Rev. Fluid Mech.* **37** (1), 357–392.
- CHU, X., WANG, W., YANG, G., TERZIS, A., HELMIG, R. & WEIGAND, B. 2021 Transport of turbulence across permeable interface in a turbulent channel flow: interface-resolved direct numerical simulation. *Transp. Porous Media* **136** (1), 165–189.
- CHUN, K.B. & SUNG, H.J. 1996 Control of turbulent separated flow over a backward-facing step by local forcing. *Exp. Fluids* **21** (6), 417–426.

## *Influence of porous material on the flow behind a BFS*

- COENEN, W., LESSHAFFT, L., GARNAUD, X. & SEVILLA, A. 2017 Global instability of low-density jets. *J. Fluid Mech.* **820**, 187–207.
- COSSU, C. & CHOMAZ, J.M. 1997 Global measures of local convective instabilities. *Phys. Rev. Lett.* **78** (23), 4387–4390.
- D'ADAMO, J., SOSA, R. & ARTANA, G. 2014 Active control of a backward facing step flow with plasma actuators. *Trans. ASME J. Fluids Engng* **136** (12), 121105.
- DEO, R.C., MI, J. & NATHAN, G.J. 2008 The influence of Reynolds number on a plane jet. *Phys. Fluids* **20** (7), 075108.
- DERGHAM, G., SIPP, D. & ROBINET, J.-C. 2013 Stochastic dynamics and model reduction of amplifier flows: the backward facing step flow. *J. Fluid Mech.* **719**, 406–430.
- DOVGAL, A.V., KOZLOV, V.V. & MICHALKE, A. 1994 Laminar boundary layer separation: instability and associated phenomena. *Prog. Aerosp. Sci.* **30** (1), 61–94.
- DOVGAL, A.V. & SOROKIN, A.M. 2004 Interaction of large-scale and small-scale oscillations during separation of a laminar boundary layer. *J. Appl. Mech.* **45** (4), 517–522.
- DRIVER, D.M., SEEGMILLER, H.L. & MARVIN, J.G. 1987 Time-dependent behavior of a reattaching shear layer. *AIAA J.* **25** (7), 914–919.
- DUCIMETIÈRE, Y.-M., BOUJO, E. & GALLAIRE, F. 2022 Weak nonlinearity for strong non-normality. *J. Fluid Mech.* **947**, A43.
- DURST, F. & TROPEA, C. 1983 Flows over two-dimensional backward – facing steps. In *Structure of Complex Turbulent Shear Flow* (ed. R. Dumas & L. Fulachier), International Union of Theoretical and Applied Mechanics, vol. 5, pp. 41–52. Springer.
- EATON, J.K. & JOHNSTON, J.P. 1981 A review of research on subsonic turbulent flow reattachment. *AIAA J.* **19** (9), 1093–1100.
- EATON, J.K. & JOHNSTON, J.P. 1982 Low frequency unsteadiness of a reattaching turbulent shear layer. In *Turbulent Shear Flows 3* (ed. L.J.S. Bradbury, F. Durst, B.E. Launder, F.W. Schmidt & J.H. Whitelaw), pp. 162–170. Springer.
- EDOUARD, D., LACROIX, M., HUU, C.P. & LUCK, F. 2008 Pressure drop modeling on SOLID foam: state-of-the art correlation. *J. Chem. Engng* **144** (2), 299–311.
- EHRENSTEIN, U. & GALLAIRE, F. 2005 On two-dimensional temporal modes in spatially evolving open flows: the flat-plate boundary layer. *J. Fluid Mech.* **536**, 209–218.
- EHRENSTEIN, U. & GALLAIRE, F. 2008 Two-dimensional global low-frequency oscillations in a separating boundary-layer flow. *J. Fluid Mech.* **614**, 315–327.
- FRANSSON, J.H.M. & ALFREDSSON, P.H. 2003 On the disturbance growth in an asymptotic suction boundary layer. *J. Fluid Mech.* **482**, 51–90.
- FREYMUTH, P. 1966 On transition in a separated laminar boundary layer. *J. Fluid Mech.* **25** (4), 683–704.
- GALLAIRE, F., MARQUILLIE, M. & EHRENSTEIN, U. 2007 Three-dimensional transverse instabilities in detached boundary layers. *J. Fluid Mech.* **571**, 221–233.
- GARNAUD, X., LESSHAFFT, L., SCHMID, P.J. & HUERRE, P. 2013 The preferred mode of incompressible jets: linear frequency response analysis. *J. Fluid Mech.* **716**, 189–202.
- GHOSH, S., LOISEAU, J.-C., BREUGEM, W.-P. & BRANDT, L. 2019 Modal and non-modal linear stability of Poiseuille flow through a channel with a porous substrate. *Eur. J. Mech. (B/Fluids)* **75**, 29–43.
- GIANOPOULOS, A. 2021 Optical flow velocimetry: optimization, benchmarking and application to system identification, modelling and control of shear flows. PhD thesis, Sorbonne Université.
- GOUJON-DURAND, S., JENFFER, P. & WESFREID, J.E. 1994 Downstream evolution of the Bénard–von Kármán instability. *Phys. Rev. E* **50** (1), 308–313.
- GUDMUNDSSON, K. & COLONIUS, T. 2011 Instability wave models for the near-field fluctuations of turbulent jets. *J. Fluid Mech.* **689**, 97–128.
- GUMOWSKI, K., MIEDZIK, J., GOUJON-DURAND, S., JENFFER, P. & WESFREID, J.E. 2008 Transition to a time-dependent state of fluid flow in the wake of a sphere. *Phys. Rev. E* **77** (5), 055308.
- GUPTA, S.K. & ADVANI, S.G. 1997 Flow near the permeable boundary of a porous medium: an experimental investigation using LDA. *Exp. Fluids* **22** (5), 408–422.
- HAHN, S., JE, J. & CHOI, H. 2002 Direct numerical simulation of turbulent channel flow with permeable walls. *J. Fluid Mech.* **450**, 259–285.
- HAMMOND, D.A. & REDEKOPP, L.G. 1998 Local and global instability properties of separation bubbles. *Eur. J. Mech. (B/Fluids)* **17** (2), 145–164.
- HEENAN, A.F. & MORRISON, J.F. 1998a Passive control of backstep flow. *Exp. Therm. Fluid Sci.* **16** (1), 122–132.
- HEENAN, A.F. & MORRISON, J.F. 1998b Passive control of pressure fluctuations generated by separated flow. *AIAA J.* **36** (6), 1014–1022.

- HENDERSON, R.D. & BARKLEY, D. 1996 Secondary instability in the wake of a circular cylinder. *Phys. Fluids* **8** (6), 1683–1685.
- HO, C. & HUERRE, P. 1984 Perturbed free shear layers. *Annu. Rev. Fluid Mech.* **16** (1), 365–422.
- HUDY, L.M., NAGUIB, A. & HUMPHREYS, W.M. 2007 Stochastic estimation of a separated-flow field using wall-pressure-array measurements. *Phys. Fluids* **19** (2), 024103.
- HUERRE, P. 2000 Open shear flow instabilities. In *Perspectives in Fluid Dynamics* (ed. K. Moffatt, G. Worster & G. Batchelor), chap. 4, pp. 159–229. Cambridge University Press.
- ILAK, M., SCHLATTER, P., BAGHERI, S. & HENNINGSON, D.S. 2012 Bifurcation and stability analysis of a jet in cross-flow: onset of global instability at a low velocity ratio. *J. Fluid Mech.* **696**, 94–121.
- INCERA GARRIDO, G., PATCAS, F.C., LANG, S. & KRAUSHAAR-CZARNETZKI, B. 2008 Mass transfer and pressure drop in ceramic foams: a description for different pore sizes and porosities. *Chem. Engng Sci.* **63** (21), 5202–5217.
- IÑIGO, J.G., SIPP, D. & SCHMID, P.J. 2014 A dynamic observer to capture and control perturbation energy in noise amplifiers. *J. Fluid Mech.* **758**, 728–753.
- JAMES, D.F. & DAVIS, A.M.J. 2001 Flow at the interface of a model fibrous porous medium. *J. Fluid Mech.* **426**, 47–72.
- JIMÉNEZ, J., UHLMANN, M., PINELLI, A. & KAWAHARA, G. 2001 Turbulent shear flow over active and passive porous surfaces. *J. Fluid Mech.* **442**, 89–117.
- JOVIC, S. 1996 An experimental study of a separated/reattached flow behind a backward-facing step.  $Re_H = 37\,000$ . *NASA Tech. Rep.* NAS 1.15:110384.
- JOVIC, S. & DRIVER, D.M. 1994 Backward-facing step measurements at low Reynolds number,  $Re_H = 5000$ . *Tech. Rep.* NASA-TM-108807.
- KAIKTSIS, L., KARNIADAKIS, G.E. & ORSZAG, S.A. 1996 Unsteadiness and convective instabilities in two-dimensional flow over a backward-facing step. *J. Fluid Mech.* **321**, 157–187.
- KLOTZ, L., GOUJON-DURAND, S., ROKICKI, J. & WESFREID, J.E. 2014 Experimental investigation of flow behind a cube for moderate Reynolds numbers. *J. Fluid Mech.* **750**, 73–98.
- KLOTZ, L., GUMOWSKI, K. & WESFREID, J.E. 2019 Experiments on a jet in a crossflow in the low-velocity-ratio regime. *J. Fluid Mech.* **863**, 386–406.
- KUWATA, Y. & SUGA, K. 2016 Lattice Boltzmann direct numerical simulation of interface turbulence over porous and rough walls. *Intl J. Heat Fluid Flow* **61**, 145–157.
- LANZERSTORFER, D. & KUHLMANN, H.C. 2012 Global stability of the two-dimensional flow over a backward-facing step. *J. Fluid Mech.* **693**, 1–27.
- MA, X., TANG, Z. & JIANG, N. 2020 Eulerian and Lagrangian analysis of coherent structures in separated shear flow by time-resolved particle image velocimetry. *Phys. Fluids* **32** (6), 065101.
- MANTIĆ-LUGO, V., ARRATIA, C. & GALLAIRE, F. 2014 Self-consistent mean flow description of the nonlinear saturation of the vortex shedding in the cylinder wake. *Phys. Rev. Lett.* **113** (8), 084501.
- MANTIĆ-LUGO, V. & GALLAIRE, F. 2016a Saturation of the response to stochastic forcing in two-dimensional backward-facing step flow: a self-consistent approximation. *Phys. Rev. Fluids* **1** (8), 083602.
- MANTIĆ-LUGO, V. & GALLAIRE, F. 2016b Self-consistent model for the saturation mechanism of the response to harmonic forcing in the backward-facing step flow. *J. Fluid Mech.* **793**, 777–797.
- MARAIS, C., GODOY-DIANA, R., BARKLEY, D. & WESFREID, J.E. 2011 Convective instability in inhomogeneous media: impulse response in the subcritical cylinder wake. *Phys. Fluids* **23** (1), 014104.
- MARQUET, O., LOMBARDI, M., CHOMAZ, J.-M., SIPP, D. & JACQUIN, L. 2009 Direct and adjoint global modes of a recirculation bubble: lift-up and convective non-normalities. *J. Fluid Mech.* **622**, 1–21.
- MARQUET, O. & SIPP, D. 2012 Convective instabilities in a backward-facing step flow: global forced perturbations. *EUCASS Proc. Ser.* **3**, 451–460.
- MARQUET, O., SIPP, D., CHOMAZ, J.-M. & JACQUIN, L. 2008 Amplifier and resonator dynamics of a low-Reynolds-number recirculation bubble in a global framework. *J. Fluid Mech.* **605**, 429–443.
- MARQUILLIE, M. & EHRENSTEIN, U. 2003 On the onset of nonlinear oscillations in a separating boundary-layer flow. *J. Fluid Mech.* **490**, 169–188.
- MEGERIAN, S., DAVITIAN, J., ALVES, L.S.D.B. & KARAGOZIAN, A.R. 2007 Transverse-jet shear-layer instabilities. Part 1. Experimental studies. *J. Fluid Mech.* **593**, 93–129.
- MICHALKE, A. 1965 On spatially growing disturbances in an inviscid shear layer. *J. Fluid Mech.* **23** (3), 521–544.
- MICHALKE, A. & HERMANN, G. 1982 On the inviscid instability of a circular jet with external flow. *J. Fluid Mech.* **114**, 343–359.
- MONKEWITZ, P.A., BECHERT, D.W., BARSIKOW, B. & LEHMANN, B. 1990 Self-excited oscillations and mixing in a heated round jet. *J. Fluid Mech.* **213**, 611–639.
- MONOKROUSOS, A., ÅKERVIK, E., BRANDT, L. & HENNINGSON, D.S. 2010 Global three-dimensional optimal disturbances in the Blasius boundary-layer flow using time-steppers. *J. Fluid Mech.* **650**, 181–214.

## *Influence of porous material on the flow behind a BFS*

- MOTOKI, S., TSUGAWA, K., SHIMIZU, M. & KAWAHARA, G. 2022 The ultimate state of turbulent permeable-channel flow. *J. Fluid Mech.* **931**, R3.
- NASTRO, G., ROBINET, J.-C., LOISEAU, J.-C., PASSAGGIA, P.-Y. & MAZELLIER, N. 2023 Global stability, sensitivity and passive control of low-Reynolds-number flows around NACA 4412 swept wings. *J. Fluid Mech.* **957**, A5.
- NISHIYAMA, Y., KUWATA, Y. & SUGA, K. 2020 Direct numerical simulation of turbulent heat transfer over fully resolved anisotropic porous structures. *Intl J. Heat Fluid Flow* **81**, 108515.
- OBERLEITHNER, K., RUKES, L. & SORIA, J. 2014 Mean flow stability analysis of oscillating jet experiments. *J. Fluid Mech.* **757**, 1–32.
- OBREMSKI, H.J., MORKOVIN, M.V., LANDAHL, M., WAZZAN, A.R. & OKAMURA, T.T. 1969 A portfolio of stability characteristics of incompressible boundary layers. *Tech. Rep.* Advisory group for aerospace research and development Neuilly-sur-Seine (France).
- OCHOA-TAPIA, J.A. & WHITAKER, S. 1995 Momentum transfer at the boundary between a porous medium and a homogeneous fluid. II. Comparison with experiment. *Intl J. Heat Mass Transfer* **38** (14), 2647–2655.
- ORMIÈRES, D. & PROVANSAL, M. 1999 Transition to turbulence in the wake of a sphere. *Phys. Rev. Lett.* **83** (1), 80–83.
- PASSAGGIA, P.-Y., LEWEKE, T. & EHRENSTEIN, U. 2012 Transverse instability and low-frequency flapping in incompressible separated boundary layer flows: an experimental study. *J. Fluid Mech.* **703**, 363–373.
- PIER, B. 2002 On the frequency selection of finite-amplitude vortex shedding in the cylinder wake. *J. Fluid Mech.* **458**, 407–417.
- PROVANSAL, M., MATHIS, C. & BOYER, L. 1987 Bénard–von Kármán instability: transient and forced regimes. *J. Fluid Mech.* **182**, 1–22.
- REGULSKI, W., SZUMBARSKI, J., ŁANIEWSKI WOŁŁK, Ł., GUMOWSKI, K., SKIBIŃSKI, J., WICHROWSKI, M. & WEJRZANOWSKI, T. 2015 Pressure drop in flow across ceramic foams – a numerical and experimental study. *Chem. Engng Sci.* **137**, 320–337.
- RIST, U. & MAUCHER, U. 2002 Investigations of time-growing instabilities in laminar separation bubbles. *Eur. J. Mech. (B/Fluids)* **21** (5), 495–509.
- RODRIGUEZ, D., GENNARO, E.M. & SOUZA, L.F. 2021 Self-excited primary and secondary instability of laminar separation bubbles. *J. Fluid Mech.* **906**, A13.
- ROOS, F.W. & KEGELMAN, J.T. 1986 Control of coherent structures in reattaching laminar and turbulent shear layers. *AIAA J.* **24** (12), 1956–1963.
- ROSTI, M.E., CORTELEZZI, L. & QUADRIO, M. 2015 Direct numerical simulation of turbulent channel flow over porous walls. *J. Fluid Mech.* **784**, 396–442.
- SATO, H. 1960 The stability and transition of a two-dimensional jet. *J. Fluid Mech.* **7** (1), 53–80.
- SCHMID, P.J. 2007 Nonmodal stability theory. *Annu. Rev. Fluid Mech.* **39** (1), 129–162.
- SCHMID, P.J. & HENNINGSON, D.S. 2001 *Stability and Transition in Shear Flows*. Applied Mathematical Sciences, vol. 142. Springer.
- SIPP, D. & LEBEDEV, A. 2007 Global stability of base and mean flows: a general approach and its applications to cylinder and open cavity flows. *J. Fluid Mech.* **593**, 333–358.
- SIPP, D., MARQUET, O., MELIGA, P. & BARBAGALLO, A. 2010 Dynamics and control of global instabilities in open-flows: a linearized approach. *Appl. Mech. Rev.* **63** (3), 030801.
- STRAATMAN, A.G., GALLEGU, N.C., YU, Q. & THOMPSON, B.E. 2006 Characterization of porous carbon foam as a material for compact recuperators. *Trans. ASME J. Engng Gas Turbines Power* **129** (2), 326–330.
- STUART, J.T. 1958 On the non-linear mechanics of hydrodynamic stability. *J. Fluid Mech.* **4** (1), 1–21.
- SUGA, K., MATSUMURA, Y., ASHITAKA, Y., TOMINAGA, S. & KANEDA, M. 2010 Effects of wall permeability on turbulence. *Intl J. Heat Fluid Flow* **31** (6), 974–984.
- SUGA, K. & NISHIO, Y. 2009 Three dimensional microscopic flow simulation across the interface of a porous wall and clear fluid by the lattice Boltzmann method. *Open Transport Phenom. J.* **1** (1), 35–44.
- SUGA, K., OKAZAKI, Y., HO, U. & KUWATA, Y. 2018 Anisotropic wall permeability effects on turbulent channel flows. *J. Fluid Mech.* **855**, 983–1016.
- SYMON, S., ROSENBERG, K., DAWSON, S.T.M. & MCKEON, B.J. 2018 Non-normality and classification of amplification mechanisms in stability and resolvent analysis. *Phys. Rev. Fluids* **3** (5), 053902.
- SYMON, S., SIPP, D. & MCKEON, B.J. 2019 A tale of two airfoils: resolvent-based modelling of an oscillator versus an amplifier from an experimental mean. *J. Fluid Mech.* **881**, 51–83.
- THEOFILIS, V. 2011 Global linear instability. *Annu. Rev. Fluid Mech.* **43** (1), 319–352.
- TILTON, N. & CORTELEZZI, L. 2008 Linear stability analysis of pressure-driven flows in channels with porous walls. *J. Fluid Mech.* **604**, 411–445.
- TILTON, N. & CORTELEZZI, L. 2015 Stability of boundary layers over porous walls with suction. *AIAA J.* **53** (10), 2856–2868.

- TROUTT, T.R., SCHEELKE, B. & NORMAN, T.R. 1984 Organized structures in a reattaching separated flow field. *J. Fluid Mech.* **143**, 413–427.
- TURTON, S.E., TUCKERMAN, L.S. & BARKLEY, D. 2015 Prediction of frequencies in thermosolutal convection from mean flows. *Phys. Rev. E* **91** (4), 043009.
- VILLERMAUX, E. 1998 On the role of viscosity in shear instabilities. *Phys. Fluids* **10** (2), 368–373.
- WAZZAN, A.R., TAGHAVI, H. & PAFFORD, D. 1986 Spatial viscous instability of the incompressible Falkner–Skan similarity profile at separation. *Phys. Fluids* **29** (7), 2039–2041.
- WEDIN, H., CHERUBINI, S. & BOTTARO, A. 2015 Effect of plate permeability on nonlinear stability of the asymptotic suction boundary layer. *Phys. Rev. E* **92** (1), 013022.
- WEE, D., YI, T., ANNASWAMY, A. & GHONIEM, A.F. 2004 Self-sustained oscillations and vortex shedding in backward-facing step flows: simulation and linear instability analysis. *Phys. Fluids* **16** (9), 3361–3373.
- WESFREID, J.E., GOUJON-DURAND, S. & ZIELINSKA, B.J.A. 1996 Global mode behavior of the streamwise velocity in wakes. *J. Phys. II* **6**, 1343–1357.
- WHITAKER, S. 1996 The Forchheimer equation: a theoretical development. *Transp. Porous Media* **25** (1), 27–61.
- WILLIAMSON, C.H.K. 1996 Mode A secondary instability in wake transition. *Phys. Fluids* **8** (6), 1680–1682.
- XU, J., BAI, J., QIAO, L. & ZHANG, Y. 2019 Development of a computational fluid dynamics compatible mathematical model for boundary layer transitional flows in low-disturbance environment. *Aerosp. Sci. Technol.* **86**, 487–496.
- ZIELINSKA, B.J.A., GOUJON-DURAND, S., DUŠEK, J. & WESFREID, J.E. 1997 Strongly nonlinear effect in unstable wakes. *Phys. Rev. Lett.* **79** (20), 3893–3896.